UNIVERSIDAD DE CONCEPCIÓN
FACULTAD DE CIENCIAS FÍSICAS Y MATEMÁTICAS

HARNESSING ATOMIC ENSEMBLES FOR THE GENERATION, ROUTING AND CHARACTERIZATION OF QUANTUM STATES

Por: Amaru Gael Moya Ragal

Tesis presentada a la Facultad de Nombre de Facultad de la Universidad de Concepción para optar al grado académico de Magíster en Ciencias con Mención en Física

Mayo 2026
Concepción, Chile

Profesor Guía: Pablo Solano
Comisión: Aldo Delgado
Stephen Walborn
Carla Hermann

"¿Cómo se mira algo que nunca más se va a ver? ¿Cómo se puede olvidar aquello que nunca se ha tenido?"

— P. Lemebel

Acknowledgements

Una página no es suficiente para agradecer a todas las personas que hicieron posible este trabajo. Espero que todos mis conocidos sepan que los agradezco profundamente por todo el cariño y apoyo que me han brindado en estos años. Sin embargo, no puedo dejar esta página vacía y esperar que todos me entiendan; por lo tanto, una mención especial a:

Denise, que ha hecho todo esto posible.

Mis compañeros, profesores, y amigos de Concepción, gracias por tenerme infinita paciencia, apoyarme, siempre estar dispuestos a ayudar y hacer de una ciudad desconocida para mí un nuevo hogar. Especialmente a Karla y Enrique, por su muy apreciada compañía durante mi magíster. A todo el equipo de LAMP, que lograron ser mi hogar y familia por estos dos largos (y quizá muy cortos) años! Y a Adonai, por ayudarme desde el día uno y obligarme a almorzar con alguien de vez en cuando.

Mis amigos de Santiago: Vale, Joaquito, Paloma, Fer, Migue, Santi, Manu, Vicho, Belu, las "mamacitas del S.J.", et al., por estar siempre ahí a pesar de la distancia.

A Pablo Solano, por recibirme en Concepción, por todas sus enseñanzas, por ser no solo un profesor increíble, pero una persona mega apañadora, y un gran guía. Al Instituto Milenio de Investigación en Óptica (MIRO), y a todo su equipo, por su apoyo financiero, logístico y por un gran ambiente durante estos años. A Carla Hermann, por ver en mi algo que yo aún no veía, tenerme fe y apoyarme en mis locuras.

A Mantú a Magdalena y Sebastián, por ser mis pilares familiares, por ser incondicionales en su amor, y por su preocupación constante por mi bienestar. No sería la persona que soy hoy sin ustedes.

To Preston, for giving me a new reason to live my life to the fullest, for all our adventures had and yet to be, for your love, your patience and your infinite tenderness. I'm on my way :-).

To Lindsay and the Cold Atoms Lab, thank you for receiving this random physics student from Chile! See you soon!

Resumen

La realización de un Internet Cuántico fue propuesta como una red que permitiría la coexistencia de infraestructura de telecomunicaciones existente con tecnologías cuánticas, permitiendo comunicación mas rapida y segura a través del entrelazamiento. Para implementar un internet cuántico, se requiere el desarrollo de fuentes de luz cuántica robustas y controlables, *routers* cuánticos eficientes y una tomografía de estados cuánticos precisa. Estos son solo algunos de los desafíos actuales que deben resolverse para avanzar de manera efectiva hacia un internet cuántico funcional. El presente trabajo explora la manipulación efectiva de medios atómicos como una plataforma versátil para diseñar, controlar y medir estados cuánticos de luz.

Primero, describimos un estudio experimental de la generación de fotones individuales a través de la emisión atómica colectiva. Usando un conjunto de átomos de rubidio frío, estudiamos la generación de fotones individuales mediante procesos DLCZ (Duan-Lukin-Cirac-Zoller), enfocándonos en las propiedades temporales y estadísticas de los fotones emitidos. Estos resultados se comparan con un protocolo superradiante, demostrando el importante papel de los efectos colectivos en la interacción luz-materia como recurso para la fotónica cuántica.

Segundo, desarrollamos un marco teórico de espejos cuánticos (*quantum mirrors*) y proponemos un procotolo para su utilización en la tomografía de estados cuánticos. Al explotar las interacciones controlables de la luz con una metasuperficie controlada por un sistema de dos niveles, demostramos que la respuesta del espejo proporciona acceso directo a la estructura del espacio de fase de estados no clásicos desconocidos.

Finalmente, mostramos un estudio preliminar sobre la generación de un reflector de Bragg en vapores de rubidio, inducido por un laser de control vía onda estacionaria contra-propagante, que resulta en una modulación periódica del índice de refracción, a través del efecto AC Stark. Este sistema se modela mediante una Teoría de Modos Acoplados utilizando un enfoque basado en la susceptibilidad que incorpora absorción, saturación y posiblemente ensanchamiento Doppler. Nuestros resultados muestran que a intensidades de *probe* más altas, la saturación conduce a un comportamiento no lineal intrínseco de los átomos, el cual podría permitir

aplicaciones como *all-optical switching*.

Keywords – Óptica Atómica, Tomografía, Tecnologías Cuánticas

Abstract

The realization of a Quantum Internet was proposed as a network that would allow for the coexistence of existing telecommunication infrastructure with quantum devices, enabling faster and more secure communication through entanglement. In order to implement a quantum internet, one requires the development of robust and controllable quantum light sources, efficient quantum routers and precise quantum state tomography. These are only some of the current challenges that must be resolved in order to make progress towards a functional quantum internet. The present work explores the effective manipulation of atomic media as a versatile platform for engineering, controlling and measuring quantum states of light.

First, we describe an experimental study of the generation of single photons through collective atomic emission. Using an ensemble of cold rubidium atoms, we study single-photon generation via DLCZ (Duan-Lukin-Cirac-Zoller) processes, focusing on the temporal and statistical properties of the emitted photons. These results are compared to a superradiant protocol, showing the important role of collective light-matter coupling as a resource for quantum photonics.

Secondly, we develop a theoretical framework of quantum mirrors and their utilization for quantum state tomography. By exploiting the controllable interactions of light with a metasurface interacting with a *control* two-level system, we demonstrate that the mirror's response provides direct access to the phase-space structure of unknown non-classical states.

Finally, we show a preliminar study on the generation of an atomic Bragg reflector in rubidium vapors, induced by a counter-propagating standing-wave control field, which results in periodic modulation of the refractive index, via the AC Stark effect. This system is modeled through a Coupled Mode Theory using a susceptibility-based approach that incorporates absorption, saturation, and possible Doppler broadening. Our results show that at higher probe intensities, saturation leads to an intrinsic nonlinear response, enabling the possibility to implement such medium for all-optical switching.

Keywords – Atomic Optics, Tomography, Quantum Technologies

Preface

In the realization of this thesis, I participated in various projects where I sought to understand how atomic mediums can be used for storage, transmission and characterization of information, be it quantum or classical light. In this document, I present my learnings and contributions to these projects, which are divided into the following five main content chapters.

Chapter 1 introduces the general context of the thesis, presenting the motivation and objectives pursued in each chapter.

Chapter 2 focuses on the general contextualization of the areas of atomic physics for both experimental and theoretical aspects, as well as the techniques used in the laboratory to manipulate atomic systems.

The experiment for Chapter 3 was designed and executed by the Cold atoms Lab past students and Professor Lindsay Leblanc. My work in this chapter was supervised by Professor Leblanc; and developed alongside Travis Hosack, a current MSc. Student at that time.

The theory for Chapter 4 was developed initially by PhD. Student Mariano Uria, under the supervision of P. Solano and Professor Aldo Delgado. My contribution included the verification of the model and extension of it to analyze its feasibility with experimental parameters.

The experimental set-up for chapter 5 as well as the initial proposition was designed by P. Solano and PhD. Student N. Vera, and executed by N. Vera and me. The hardware (including lasers!) was designed and executed by the team from the LAMP Laboratory.

A publication based on Chapter 4 is currently in preparation.

Contents

List of Figures

1

Overview and Motivation

The New Sound

Geordie Greep

1.1 Introduction

Since the quantum revolution began its unfolding in the early 20th century, our understanding of the physical world has undergone a profound transformation. Physicists all over the world developed tools that allowed us to discover and begin to understand the behaviour of matter and energy at the smallest scales, leading to groundbreaking discoveries that have reshaped our technological landscape. Even today, the quantum revolution continues to question our understanding of the world. One of the most widely discussed concepts still is entanglement—the phenomenon by which two or more quantum systems exhibit correlations that persist regardless of the distance between them.

This phenomenon has given rise to a *Second* Quantum Revolution, where we now seek to *utilize* the emerging phenomena of quantum mechanics, such as entanglement and superposition. From this, entire fields of research have emerged, including but not limited to: quantum information, quantum cryptography, and quantum computing, between many others. These disciplines are not only redefining how we process information, but also challenging our fundamental notions of what *information* itself means.

Certain areas have seen the potential benefits of the quantum characteristics in solving problems that have a limiting factor associated to classical systems. In particular, we will be interested in *quantum technologies*; as a grand scheme, what scientists all over the world are trying to achieve is to: first, be able to isolate and control a 'simple' quantum system, (such as an atom, ion, photon, or superconducting circuit). Second, to be able to manipulate these systems to

perform specific tasks, such as storing and processing information. Finally, to be able to scale up these systems to create larger and more complex quantum networks.

While atoms and ions are excellent for storing information (acting as stationary nodes), they cannot easily send that information over long distances. This is where light comes into play. Photons are ideal for transmitting information over long distances due to their speed and low interaction with the environment, making them less susceptible to decoherence.

In particular to the focus of this thesis, there are three main challenges that need to be overcome in order to realize the full potential of quantum technologies with light. First, how can one reliably generate the quantum light (single photons) that serve as the building blocks of stable qubits? What's an efficient mechanism for routing the photonic states for optical processing? And how can we make fast and reliable measurements of these quantum states? In the search for the answers one must always find more fundamental questions, so in this work I present my contribution in this huge, developing area.

1.2 State of the Art

1.2.1 The Quantum Internet

The possibility of including quantum advantages into a global communication network has been (and still is) an important goal in the quantum information community. The idea of a quantum internet (Kimble (2008)) was proposed as a network that would allow the coexistence of classical systems with quantum devices, enabling more secure, faster and efficient communication. The ultimate goal is to interface classical and quantum systems within the same network, allowing for the transmission of both classical and quantum information. For example, a problem could be offloaded to a remote quantum computer for simulation or processing, with the results transmitted back to a classical user via the quantum network (See Figure 1.2.1)

For a quantum internet to be realized, several key components need to be developed and integrated. These include but are not limited to:

- **Quantum light sources**, for generating quantum states of light with high fidelity and efficiency.
- Quantum channels, for allowing the transmission of quantum information over long distances with minimal loss and decoherence.
- Quantum repeaters, for extending the range of quantum communication by overcoming losses and errors in the channels.
- **Quantum routers**, for redirecting quantum information to the appropriate destinations within the network.
- Quantum memories, for storing quantum information for later retrieval and processing.
- Quantum processors, for manipulating and processing quantum information for various applications.
- **Quantum tomography**, for accurately measuring and reconstructing quantum states of light.

In the following sections, we will review some of the current developments and open challenges that researchers are facing in the development of some of these technologies; in particular, for a quantum light source we study the generation of single photons. This thesis addresses *three* distinct contributions within these niche areas. First, addressing the need for light sources, we investigate the generation of single photons in cold rubidium clouds. Second, regarding signal routing, we explore a rapidly reconfigurable Bragg lattice in warm atomic vapors. Finally, to address the challenge of verification, we propose a novel measurement protocol utilizing a tool we term Quantum Mirrors.

1.2.2 Single Photon Source

Single photons show promising signs in becoming one of the fundamental units for quantum information. They can be used to encode quantum bits (qubits) and can be manipulated using quantum gates. Light has a few characteristics that makes it specially attractive for quantum information processing, such as the fact that photons are *really* fast, work in ambient temperatures, and don't interact easily with their environment. Because of this, researchers have put lots of efforts into finding out what is the best way to generate single photons, control their interactions with different systems and preserve the coherence and fidelity of the

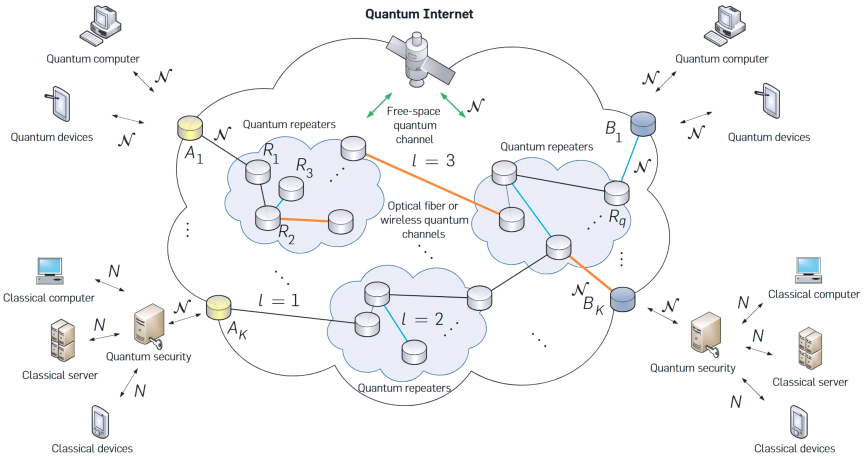

Figure 1.2.1: From Gyongyosi and Imre (2022). Illustration depicting the connections and components of a quantum internet. Quantum channels connect quantum nodes, enabling the transmission of quantum information. Nodes are able to generate, process, and store quantum states, while the channels permit distribution of states and entanglement through the network. This image has been upscaled using AI tools.

information stored in these quanta of light.

Research is still ongoing for an effective, deterministic single photon source. Although there have been many advances in the field, such as the use of quantum dots (Liu et al. (2025)), color centers in diamond (Pezzagna et al. (2011)) and atomic vapors (Glorieux et al. (2023)), there is still no perfect solution. The main challenges include achieving high efficiency, low noise, bandwidth limitations and scalability for practical applications in quantum computing and communication. Researchers are exploring various approaches to overcome these challenges, including the development of new materials and techniques for photon generation and manipulation.

In the case of atomic vapors, alkali atoms such as rubidium and cesium have been widely used due to their deeply studied transitions, as well as succesful manipulation through cooling and trapping mechanisms (see 2.6 for further discussion), which allows for precise control over their interactions with light. Due to the high level control and strong nonlinearities that atomic vapors present, they have been used in a variety of applications, including but not limited to quantum memories (Saglamyurek et al. (2021)) and quantum repeaters (Sangouard et al. (2011)). This makes then an ideal platform for generating single photons for quantum information processing.

In particular, in Chapter 3, we will explore the generation of single photons using cold atomic clouds. The highly controllable environment makes them an ideal platform for generating single photons with high fidelity and efficiency. We investigate different protocols based on state-of-the-art literature for generating single photons, exploit the collective effects that cold atoms possess, and benchmark their performance, with the goal of identifying strategies that optimize the efficiency and quality of the single-photon source.

1.2.3 Quantum State Tomography

Due to the fragile nature of quantum states, accurately measuring and reconstructing these states is a significant challenge in quantum information processing. In this sense, optical systems have a strong presence in quantum information processing, due to their low decoherence rates and ease of manipulation. Quantum state estimation, or quantum state tomography, is the process of reconstructing the quantum state of a system from a series of measurements. Standard quantum tomography relies on homodyne or heterodyne detection (Leonhardt (1997)), methods that are often computationally and experimentally resource intensive (Anshu and Arunachalam (2024)), even more so when applied to continuous variable systems (Lvovsky and Raymer (2009b)). Alternative methods have been proposed, such as direct Wigner function measurement using photon-number-resolving detectors (Sridhar et al. (2015)), but these approaches often require complex setups and are limited by detector inefficiencies.

In Chapter 4, we study the feasibility of a protocol for quantum tomography of continuous variables for states of light, namely the possibility of reconstructing the Wigner function of quantum states using a tool we term Quantum Mirrors. We will show how this method overcomes some of the limitations of traditional homodyne and heterodyne detection methods, providing a more efficient and scalable approach to quantum state reconstruction. By leveraging the unique properties of Quantum Mirrors, we aim to develop a protocol that is both experimentally feasible and capable of accurately characterizing quantum states.

1.2.4 Atomic Vapor based Optical Switch

Basing ourselves in the field of fiber optics, fiber Bragg gratings have been widely used for switching, filtering and sensing applications (Erdogan (1997)). Bragg

gratings are periodic structures that reflect particular wavelengths of light and transmit others. This is achieved by creating a periodic variation in the refractive index of the medium. When studying the nonlinear interactions of light and matter in fiber optics, one of the characteristics that shines is the fact that optical fibers such as the ones made with erbium and silica have very small nonlinear coefficients, and as such, nonlinear interactions require a lot of power to be observed. This is not the case with alkali atoms such as rubidium, which in experimental settings with small beams needs not more than a few mW in power to interact nonlinearly with the medium (Aladjidi et al. (2022)).

For us to be able to create a Bragg grating in an atomic vapor, we need to be able to manipulate the refractive index of the medium. This can be achieved through the use of two counter-propagating laser beams to create an interference pattern. The periodicity of the interference pattern creates a periodic variation in the refractive index of the medium, which can be used to reflect specific wavelengths of light. This could be an interesting step in optical quantum computing, as it could be used to create optical switches and memory devices, such as seen in (Dawes et al. (2005)), where they demonstrated the ability of low-intensity light switching in a warm rubidium vapor, and others (Stern et al. (2016), Chen et al. (2013))

Challenges in optical nonlinear switches include high power requirements, slow response times, and integration difficulties with existing technologies. Overcoming these challenges is crucial for the development of practical optical computing systems. Up to our knowledge, there has been no research on the possibility of creating a Bragg grating in a warm atomic vapor and using the reflections as an optical switch for information processing, nor a study on the intrinsic bistable response of the system due to saturation effects present in atomic mediums. This is the gap that Chapter 5 of the thesis aims to fill.

1.3 Objectives of the Thesis

Single Photon Source

- To study and implement a single photon source in a cold rubidium cloud, based on the DLCZ protocol for effective photon generation and high degree of control.

- To characterize the correlations of generated single photons, their emission rates, assess and compare their suitability for quantum information applications.
- To compare the performance of the single photon source in cold atomic mediums with the DLCZ protocol versus the photons generated using superradiant protocol, identifying the advantages and limitations of each approach.

Quantum State Tomography

- To develop and implement a quantum state tomography protocol that overcomes traditional complications associated with homodyne and heterodyne detection methods.
- To validate the tomography method by comparing reconstructed states with theoretical predictions, ensuring high fidelity and reliability of the measurements.
- To explore the experimental feasibility of the proposed tomography protocol, assessing its scalability and potential applications in quantum information processing.

Atomic Vapor based Optical Switch

- To investigate the feasibility of creating a Bragg reflector in atomic vapors using a counter-propagating standing wave, and to analyze the resulting reflection and transmission properties.
- To incorporate temperature effects through Doppler broadening and verify the viability of a warm vapor Bragg lattice.
- To explore the intrinsic bistable response of the atomic medium due to saturation effects, and to evaluate its potential for use as an optical switch in quantum information processing.
- To design and optimize the experimental parameters, such as laser intensity, detuning, and atomic density, to achieve efficient switching behavior and high reflectivity in the Bragg grating setup.

1.4 Outline of the thesis

The thesis has been organized to follow a logical progression from foundational concepts in atomic physics, to the generation of single photons, the development of an optical switch for photonic channels, and finally to the implementation of quantum state tomography.

More specifically, Chapter 2 seeks to set an even terrain in both theoretical and experimental physics, describing the basics of atomic physics ranging from the ability to understand atomic transitions in different fine/hyperfine/Zeeman structures to reviewing lock mechanisms for lasers in the laboratory.

Chapter 3 then delves into the generation of single photons using cold atomic clouds of rubidium, implementing the DLCZ protocol for effective photon generation and control. The chapter characterizes the correlations of the generated photons and compares their performance with those generated using superradiant protocols.

Chapter 4 focuses on the theoretical development and implementation of a quantum state tomography protocol through a medium known as Quantum Mirrors. The chapter validates the tomography method by comparing reconstructed states with theoretical predictions, ensuring high fidelity and reliability of the measurements.

Chapter 5 studies the possibility of a Bragg grating response in a warm atomic medium, and characterized the instrinsic bistabilities in the system due to a saturation and loss effects present in atomic mediums. An experimental proposal is presented to implement an optical switch based on these principles.

Finally, Chapter 6 summarizes the key findings of the thesis, discusses their implications for the field of quantum information processing, and outlines potential directions for future research.

2

Basic Concepts for Atomic Physics

Palabritas y Palabrotas

Diego Lorenzini

The main goal of this chapter is to introduce and contextualize important concepts in the world of atomic physics used in the following chapters of this work. Concepts that will be reviewed in this chapter belong to the historical guidelines of understanding how light and matter interact, and the particular effects that appear when external fields interact with an atom, such as electric and magnetic fields. We will also consider other effects such as temperature, all the former are measurable perturbations that exist in atomic media when interacting with a probe. We also dwell on a more particular case, for experimental situations where it is needed to know how to find atomic transitions and *lock in* a laser to the important features. Finally, we will conclude with a quick introduction to cooling atoms.

2.1 Atomic Structure

Rubidium is one of the atomic physicists favorite elements in the periodic table. It was foundational in discoveries and technologies developed, ranging from spectroscopy to more recent technologies such as Bose-Einstein condensates and atomic clocks. This prominence is largely due to the fact that diode lasers in the wavelength range of rubidium transitions were one of the first developed and more widely available, making experiments with rubidium more accessible.

This historic element is part of the alkalis group. One of the most important features in alkali atoms is the fact that they are hydrogenous elements, this means that they possess a single valence electron, which allows for treating them in a more simplified manner: as a big nucleus with some perturbation and a single electron in the outer shell. This allows not only for a helpful treatment as a *two*

level system, which we will explain briefly, but also for a more complex study of three or four level atoms of various configurations.

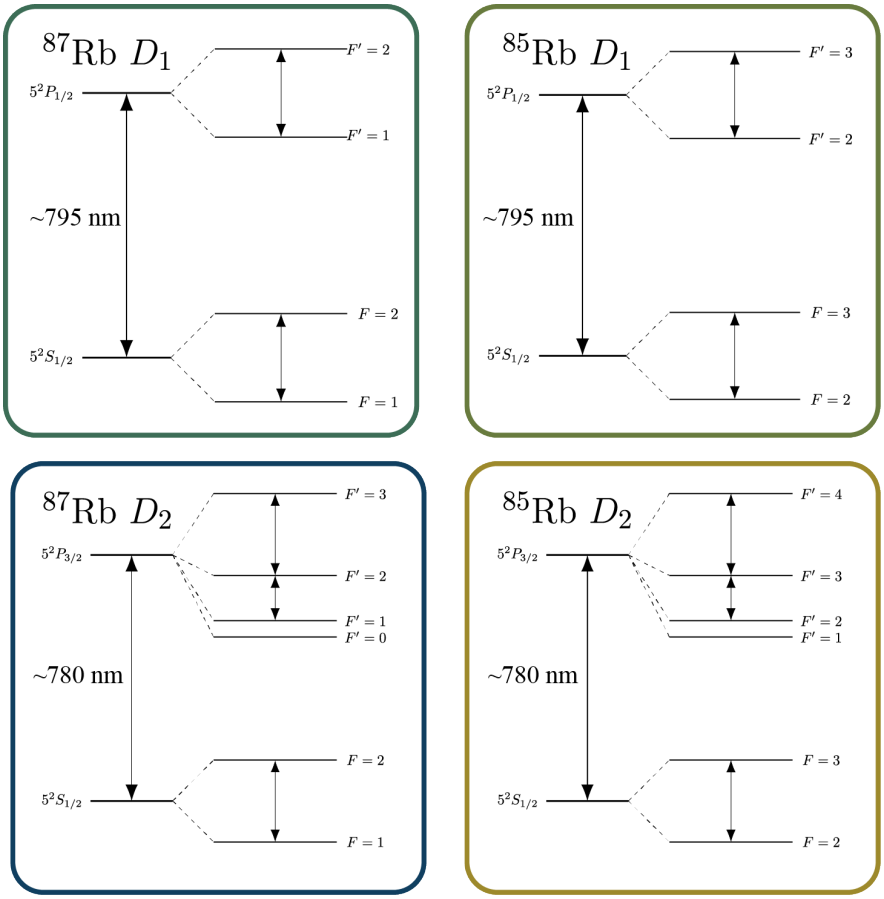

Figure 2.1.1: Illustration of the general atomic structure of naturally occurring rubidium, with the D1 and D2 lines. For more details and information on the atomic structure of both ^{85}Rb and ^{87}Rb, refer to Steck (2001).

When we talk about the atomic structure, it is first most important to mention that rubidium has two naturally occurring isotopes, that is ^{87}Rb and ^{85}Rb. Working with Rubidium, the most used transitions are the so-called D1 and D2 lines (pictured in Fig. 2.1.1), which are around 795 nm and 780 nm respectively; this relatively small range is where most experiments in the area of atomic physics are realized; this is because, as we have discussed before, of historical and resource reasons. The D lines correspond to the so-called *fine structure transitions*. In the following section we will briefly explain what this means and what makes these transitions so important and helpful for atom light interactions.

2.2 Fine and Hyperfine Structure

The study of atomic structure through history has revealed unexpected phenomena; at first glance, it might seem that once the emission spectra of an element can be measured, the remaining task is simply to construct a theoretical model that reproduces the observed spectral lines and their structure. However, very quickly, researchers found some discrepancies; some lines appeared slightly shifted, or multiple lines were observed where theory predicted a single one. As is now understood, these anomalies arise because external fields interact with atoms, lifting intrinsic degeneracies that were previously hidden. In this section, we introduce the physical origins of these perturbations and establish the framework commonly used to describe them.

2.2.1 Fine Structure

Fine structure corresponds to a splitting that occurs due to the coupling between the electron's spin and its orbital angular momentum. The spin S and the orbital angular momentum L couple to form the total angular momentum $J = L + S$. For given values of L and S the allowed values of J range from $J = |L - S|$ to $J = L+S$. Spin-orbit interaction typically results in meV shifts of the energy levels. Taking into account the spin-orbit coupling and other relativistic corrections one arrives at the fine structure of the atomic levels, which are determined by their quantum numbers n, J, L and S.

For a hydrogen like atom, one can write the hamiltonian that describes the spin-orbit interaction as

$$H_{SO} = \frac{Ze^2}{4\pi\varepsilon_0} \frac{(g_s - 1)\mathbf{L} \cdot \mathbf{S}}{2m_e^2 c^2 r^3}, \tag{2.2.1}$$

Z corresponds to the atomic number, g_s is the electron spin g-factor (the ratio of the magnetic moment of a particle to that expected of a classical particle of the same charge and angular momentum), m_e is the electron mass, c is the speed of light, and r is the distance between the nucleus and the electron Sommerfeld (1940), Michelson and Morley (1887). This model however still assumes that the nucleus is a point-like charge that is infinitely heavy and has no intrinsic electric or magnetic structure.

2.2.2 Hyperfine Structure

Dropping the aforementioned assumption, we can refine the energy levels further. This leads us to the concept of **hyperfine structure**, which arises from the interaction between the nuclear spin I and the total electronic angular momentum J, resulting in a total angular momentum $F = I + J$. An electron with spin angular momentum $\mathbf{S}$ has a magnetic moment $\vec{\mu}_s$ given by:

$$\boldsymbol{\mu}_s = -g_s \mu_B \mathbf{S}, \tag{2.2.2}$$

where μ_B is the Bohr's magneton. Hyperfine interactions lead to energy level splittings on the order of μeV, which are (generally) significantly smaller than those caused by fine structure (This can also be refered to as *IJ-coupling*).

The hyperfine Hamiltonian is typically expanded into magnetic dipole and electric quadrupole contributions:

$$H_{\text{hfs}} = A_{\text{hfs}} \mathbf{I} \cdot \mathbf{J} + B_{\text{hfs}} \frac{3(\mathbf{I} \cdot \mathbf{J})^2 + \frac{3}{2}(\mathbf{I} \cdot \mathbf{J}) - \mathbf{I}(\mathbf{I}+1)\mathbf{J}(\mathbf{J}+1)}{2\mathbf{I}(2\mathbf{I}-1)\mathbf{J}(2\mathbf{J}-1)}. \tag{2.2.3}$$

Here, A_{hfs} is the magnetic hyperfine constant, arising from the interaction between the nuclear magnetic dipole moment and the magnetic field generated by the electron; it also has units of energy. Rubidium has no permanent electric dipole moment. The constant B_{hfs} is then known as the electric quadrupole hyperfine constant, which arises from the interaction between the nuclear electric quadrupole moment and the gradient of the electric field created by the electron.

2.2.3 Zeman Splitting

When an external magnetic field interacts with an atom, the degeneracy of the magnetic sublevels is lifted (see Figure 2.2.1). This was discovered by Pieter Zeeman in 1896, when he observed that the spectral lines of sodium were split into multiple components in the presence of a strong magnetic field. This effect can be explained by considering the interaction of the magnetic moment of the electron with the external magnetic field. It is generally introduced as a perturbation to the atomic Hamiltonian, given by

$$\hat{H} = -\hat{\boldsymbol{\mu}} \cdot \mathbf{B}, \tag{2.2.4}$$

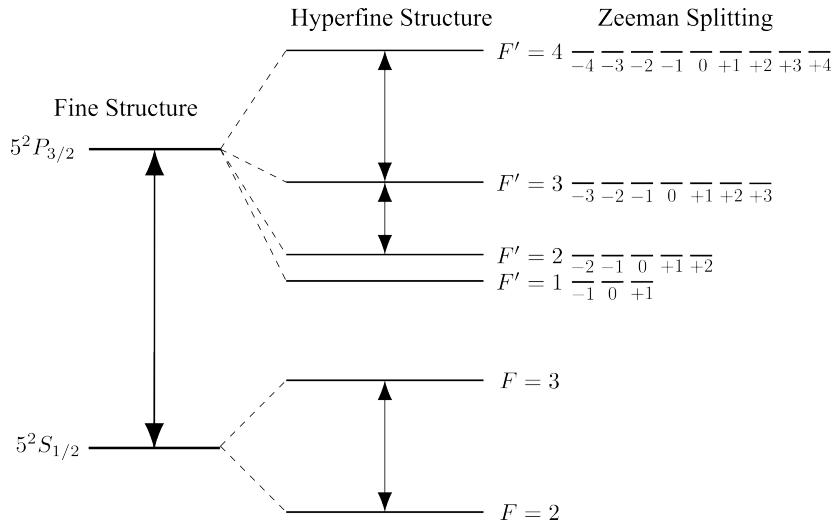

Figure 2.2.1: Illustration of the general atomic structure for the D_2 line in rubidium. The fine and hyperfine splittings, and the Zeeman effect due to an external magnetic field. Although not shown, all hyperfine levels will also experience a Zeeman splitting in the presence of an external magnetic field.

where B is the external magnetic field, and $\hat{\boldsymbol{\mu}} = \boldsymbol{\mu}_L + \hat{\boldsymbol{\mu}}_s + \hat{\boldsymbol{\mu}}_I$ is the magnetic moment operator of the electron, which contains contributions from the orbital momentum and the spin of the electron, as well as a small contribution from the nuclear spin.

There are, of course, even more shifts that have not been discussed here, such as the Lamb shift, which is a quantum electrodynamics effect that arises from the interaction of the electron with vacuum fluctuations of the electromagnetic field. However, these are not as relevant for the scope of this thesis and will not be discussed further.

2.3 Linear Response of an Atom to an External Field

The interaction between radiation and matter easily result in different perturbations, which can be described through macroscopic effects, for example, the polarization of a medium. For this Section, we now look into outputs that can occur from interaction with an external source of fields, such as absorption, scattering, and emission of light. In general, a case study can be done in both semi-classical and quantum descriptions (Foot (2005), Boyd (2020)). In this case,

we will start with a more classically oriented focus and note when a quantum description might be more appropriate.

Consider a two level atom with states $|g\rangle$ and $|e\rangle$ separated by an energy $\hbar\omega_0$. The atom is driven by a classical electric field of frequency ω and amplitude E_0. Assuming that the size of the atom is much smaller than the optical wavelength, there is no need to consider the spatial dependence of the electric field (we call this *dipole approximation* Jaynes and Cummings (1963)).

Here, we can make use of the analogy of the electron's motion to a damped harmonic oscillator driven by an external electric force, identifying the force on the electron due to the field $\boldsymbol{F} = -e\boldsymbol{E}$. The damping ("friction") term models radiation reaction due to the charge acceleration (the classical analog of spontaneous emission) and collisions with other atoms.

We can define the polarizability α as the proportionality constant between the induced dipole moment and the electric field; $\boldsymbol{d} = -\alpha(\omega)\boldsymbol{E}$. Using the solution for x_0, we can write the solution for a resonant interaction with no phase lag, and then rewrite the polarizability as

$$\alpha(\omega) = \frac{e^2/m}{\omega_0^2 - \omega^2 - i\gamma\omega}, \tag{2.3.1}$$

where e and m correspond to the electron's charge and mass, respectively, ω_0 is the resonant frequency of the atomic transition, and γ represents the damping rate (linewidth).

This characterizes the frequency-space response of the atom due to the incident electric field. Now, since we are working with atomic ensembles, we can use the definition for polarization $\boldsymbol{P} = N\boldsymbol{d} = \epsilon_0\chi\boldsymbol{E}$ and write the susceptibility as

$$\chi(\omega) = \frac{N\alpha(\omega)}{\epsilon_0} = \frac{Ne^2/m}{\epsilon_0(\omega_0^2 - \omega^2 - i\gamma\omega)}, \tag{2.3.2}$$

where N is the atomic density (number of atoms per unit volume) and ϵ_0 is the vacuum permittivity. χ is then known as the atomic susceptibility, which fully characterizes the optical response of the medium under the excitation of an external electric field. It is a complex quantity (and a tensor for many elements and materials depending on the symmetry). The real part describes the *dispersion* of the medium. It is related to the index of refraction n, governing the phase

velocity of light through the atomic vapor. The imaginary part describes the *absorption* (or gain) of the radiation. See Figure 2.3.1 for a plot of the real and imaginary components of the atomic susceptibility.

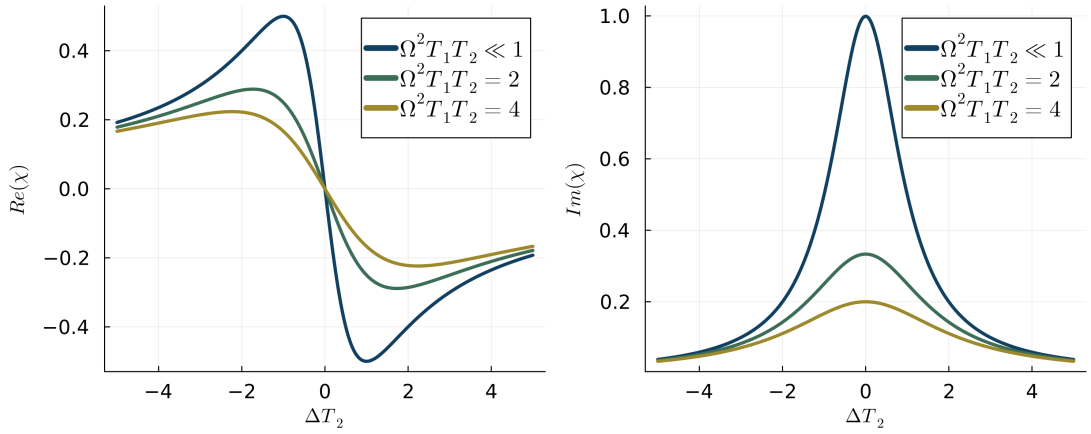

Figure 2.3.1: Reconstructed plot of the real and imaginary components of the atomic susceptibility as derived in Boyd (2020). These susceptibilities have been normalized to the constant $a_0 c/\omega_e g$.

2.4 Nonlinear Response of an Atom to an External Field

In order to describe the optical nonlinearities that the medium exhibits, and if we neglect frequency conversion processes, we can describe the generalization of the polarization as a power series of what we derived in the last section:

$$\mathbf{P}(t) = \varepsilon_0[\chi^{(1)}\mathbf{E}(t) + \chi^{(2)}\mathbf{E}^2(t) + \chi^{(3)}\mathbf{E}^3(t) + \dots] \tag{2.4.1}$$

$\chi^{(i)}$ denotes the i-th order nonlinear optical susceptibilities. This description shows the hidden nonlinearities of the interaction, which allows us to deepen our understanding of the system.

However, we must emphasize that the description of the nonlinear polarization as a power series is only valid within a certain range of parameters. The Taylor expansion works as an approximation only when the applied intensity is below the saturation regime of the medium. We can see this limitation when looking at Figure 2.4.1; the expansion coefficients will alternate sign in the contributions,

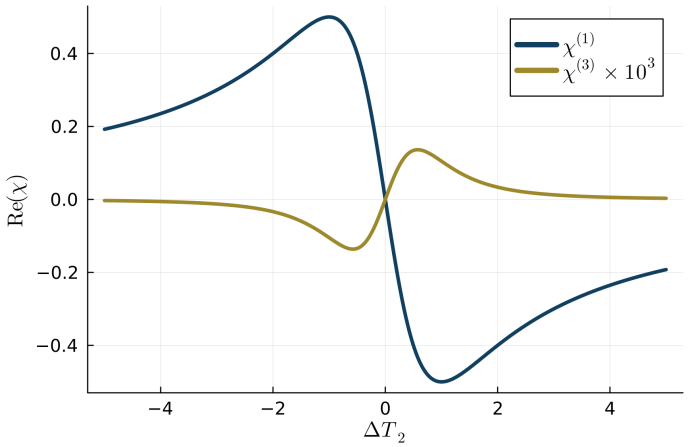

Figure 2.4.1: Reconstructed plot of the first and third components of the atomic susceptibility as derived in Boyd (2020). These susceptibilities have been normalized to the constant $a_0 c/\omega_e g$.

so as the incoming field becomes stronger, the nonlinear orders will contribute towards a saturation of the response in the medium.

2.4.1 Kerr Effect

When an intense beam of light propagates through a medium, the electric field itself induces a significant nonlinear response. We consider a monochromatic field:

$$\mathbf{E}(\mathbf{r}, t) = \mathbf{E}_\omega \cos(\omega t) \tag{2.4.2}$$

From this field, a medium will respond according to the nonlinear polarization expansion (Eq. 2.4.1) The third-order term will generate a contribution at the same frequency as the incident field, which can be written as:

$$\mathbf{P} \approx \varepsilon_0 \left(\chi^{(1)} + \frac{3}{4} \chi^{(3)} |\mathbf{E}_\omega|^2 \right) \mathbf{E}_\omega \cos(\omega t). \tag{2.4.3}$$

This results in an intensity-dependent refractive index, which is what we know as the optical **Kerr effect**. Unlike the quadratic term, the way the response depends on the magnitude of E is independent of the sign of E, so the behaviour is symmetrical between positive and negative fields. The consequence is that $\chi^{(3)}$ is non-zero in centrosymmetric materials (such as glass, liquids, and gases) where $\chi^{(2)}$ is zero by symmetry.

The change in the refractive index, $\Delta n = n - n_0$, is proportional to the incident intensity I:

$$\Delta n \approx \left(\frac{3\chi^{(3)}}{4c\varepsilon_0 n_0^2} \right) I. \tag{2.4.4}$$

This effect underlies the potentially damaging effect of self-focusing, as well as the temporal effects of self-phase modulation (SPM) and self-steepening. Self-phase modulation plays a crucial role in a variety of pulse compression processes, as well as in optical soliton formation. We typically represent this type of nonlinearity as

$$n = n_0 + n_2 I, \tag{2.4.5}$$

with $n_2 = \left(\frac{3\chi^{(3)}}{4c\varepsilon_0 n^2} \right)$, and $I = \frac{1}{2} n_0 \varepsilon_0 c E^2$ the intensity if the incident wave. Once again, the real part of the refractive index describes a response that occurs as a consequence of parametric processes, while the imaginary part of the refractive index describes the absorption of radiation, which results from the transfer of population from the atomic ground state to an excited state.

2.4.2 Stark Effect

The Stark shift arises from virtual transitions induced by interacting photons with the atomic system. Much like Zeeman splitting, electric fields that interact with the atom, can also shift the atomic energy levels, so the transitions will be shifted from what we expect theoretically. This effect can be either linear or quadratic, and it can be explained by perturbation theory (Delone and Krainov (1999)). Light shifts have been a fundamental effect in atomic physics, as they are often used to confine and control particles in optical dipole traps and lattices. However, light shifts can also perturb measurements or produce errors, for example, in atomic clocks. This is meant to be a brief introduction and the derivation is outside the scope of this thesis, although these effects might appear.

2.4.2.1 DC Stark Effect

Corresponds to the perturbation that occurs due to a static, relatively weak electric field $\boldsymbol{E}$. For a two level atom this can be written as a time independent first order perturbation of the Coulomb hamiltonian

$$H_{Stark} = -\hat{\mu} \cdot \boldsymbol{E} = -e\boldsymbol{r} \cdot \boldsymbol{E}, \tag{2.4.6}$$

where the energy shift ΔE will be given by

$$\Delta E = -\frac{\alpha(\omega)|\boldsymbol{E}|^2}{2} \tag{2.4.7}$$

2.4.2.2 AC Light Shifts

In the case of a weak, non-constant electric field, one can follow the time-dependent perturbation theory; considering that the effects appear on the second order of this derivation. For the simpler case of a two level atom, the energy shift ΔE will be given by

$$\Delta E = \mp\frac{\mu_{eg}^2 I}{2\varepsilon_0 c\Delta} \tag{2.4.8}$$

2.4.3 Doppler Effect

Working with hot atomic vapors means the particles are in constant motion. Doppler broadening corresponds to the inhomogeneous broadening of the linewidth of atomic transitions caused by the random movements of atoms. It is the dominant line broadening mechanism in gas lasers. If the atoms have a thermal velocity distribution with temperature T, the linewidth resulting from the Doppler effect is

$$\Delta\nu_D = \frac{2\nu_0}{c}\sqrt{2\ln 2 \cdot \frac{k_B T}{m}}$$

where ν_0 is the mean optical frequency, and m corresponds to the atomic mass. For atoms in a room temperature gas cell this effect is typically much larger than the natural linewidth of the atomic transition.

The broadening has to be taken into account when modulating the index of refraction, which can be done through a convolution of the susceptibilities and 1D the Maxwell-Boltzmann distribution. As a first approximation for this effect, one can consider a temperature of $T = 400$ K and calculate the Doppler width for the rubidium D2 line at 780 nm. This results in a Doppler width of around 300 MHz (see Figure 2.4.2), which is much larger than the natural linewidth of $\gamma \approx 2\pi 6$ MHz.

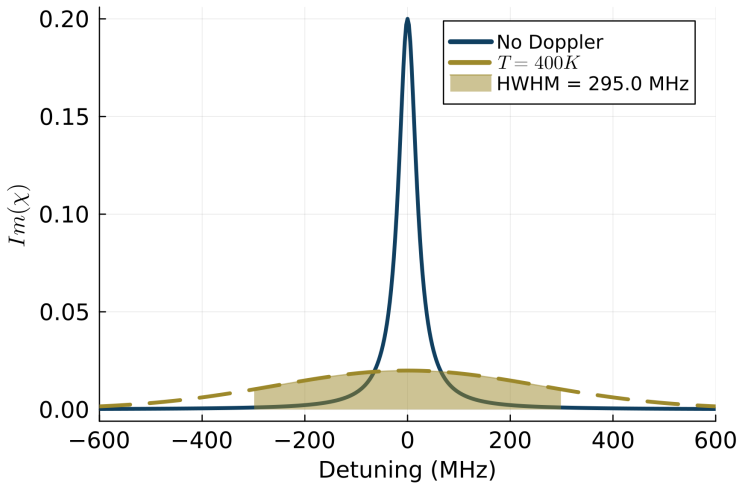

Figure 2.4.2: Illustration of the Doppler broadening effect on the absorption profile (Imaginary part of the susceptibility) of an atomic transition (^{87}Rb).

2.4.4 Saturation Intensity

It is a natural question to ask *what mechanism* explains the fact that once a two level atom is excited, within the natural decay time, it will not be able to absorb any more energy/photons. This is what is known as a saturation effect. In a more macroscopic perspective, light of a higher intensity than I_{sat} does not have the same effect on an atomic ensemble. By writing the difference in population difference of this two level atom,

$$N_1 - N_2 = \frac{N}{1 + I/I_{sat}}, \tag{2.4.9}$$

where $I_{sat} = \hbar\omega A_{21}/2\sigma(\omega)$. The minimum value for I_{sat} is when light is on resonance wiht the transition. This is when saturation is largest; defined by

$$I^0_{sat} = \frac{\pi h \Gamma}{3\lambda^3}, \tag{2.4.10}$$

where Γ^{-1} is the lifetime for the transition, and λ is its wavelegth. In particular, rubidium in the D_2 line $\lambda = 780$ nm has a lifetime of around 26.2 ns. A quick calculation then results in $I^0_{sat} \approx 0.8\text{mW/cm}^2$. If we review the document from Steck (2001), all non-resonant I_{sat} are slightly higher than this value, which we excpect.

2.5 Locking a Laser to a warm cell

In order to perform experiments with atomic systems, two main things must be taken into account: first, the laser linewidth must be narrower than the atomic transition linewidth γ, and second, we must be able to control the center frequency ω of the laser near the transitions.

For the former requirement, most commercial grade lasers already have the needed linewitdths. Since at the Laboratory of Atomic and Molecular Physics (LAMP) we develop our own lasers, we have two main mechanisms to narrow the linewidth; optical feedback from a diffraction grating in LITTROW configuration (Hawthorn et al. (2001)), and optical feedback from an external cavity (Dahmani et al. (1987)). Both of these mechanisms can be used to achieve very narrow linewidths.

For the latter requirement, it is now standard practice to **lock** the laser frequency to an atomic transition. This is done by deflecting a small portion of the laser light to an atomic reference system. The light will interact with an atomic vapour cell, and the transmitted light will be detected using a photodiode. This signal can then be used to send electrical signals and control the laser frequency. In the section that follows, we will explain in further detail how to **lock your laser to an atomic transition**.

2.5.1 Locking Mechanisms

Laser diodes have been effective tools for atomic physics experiments. However, as we have hinted, the center frequency of a laser diode is not stable enough as is, being very sensitive to current, temperature, humidity and the environment in general; this will have an effect on the diode frequency such that it will change from the expected one (known as *drift*). To overcome this problem, the laser frequency is *locked* to an atomic resonance; this means that the laser frequency is continuously adjusted and stabilized via feedback. The feedback is usually done by modulating the laser current (with the possible addition of optical feedback), and using the error signal from the atomic reference to correct the frequency.

There are two main quantities which can be used to study the stability of a laser: the Power Spectral Density (studied in frequency domain) and the Allan Deviation (studied in time domain). The first one is associated with the linewidth

of the laser and is studied by a beat-note analysis or autocorrelator, while the latter describes long term effects on performance, akin to standard variation, and studied as a time series from a beat-note or wavemeter. For our particular case, we tend to care more about the first one, since one can always re-lock the laser for experiments.

Two locking mechanisms used in the development of this thesis. They are known as Saturated Absorption Spectroscopy (SAS) and Dichroic Atomic Vapor Laser Lock (DAVLL). Both of these mechanisms use a warm atomic vapor as a reference, and both can be used to lock the laser to a specific transition (see Figure 2.5.1). The main difference between them is that SAS uses a counter-propagating pump and probe beam to achieve sub-Doppler resolution (Wieman and Hänsch (1976)), while DAVLL, based on the SAS protocol, adds a controlled magnetic field to achieve a higher quality signal in the Zeeman manifold (Corwin et al. (1998)).

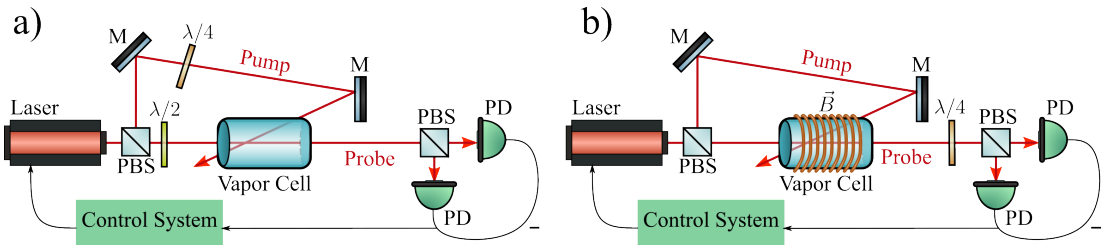

Figure 2.5.1: a) Saturated Absorption Spectroscopy (SAS) setup. A laser beam is split into a strong pump and a weak probe beam, which counter-propagate through a vapor cell. The transmitted probe beam is detected using a photodiode. b) Dichroic Atomic Vapor Laser Lock (DAVLL) setup. A linearly polarized laser beam passes through a vapor cell placed in a magnetic field, which splits the atomic energy levels via the Zeeman effect. The transmitted light is analyzed using a quarter-wave plate and a polarizing beam splitter, creating two circularly polarized components that are detected by two photodiodes. Figure adapted from Mäusezahl et al. (2024)

2.5.1.1 SAS and DAVLL

SAS, also known as Doppler Free Spectroscopy, is a technique that allows for the observation and determination of atomic and fine transition frequencies without the effects of Doppler broadening (discussed in 2.4.3). This is useful when probing atomic vapors, where the thermal motion of atoms can lead to significant broadening of spectral lines.

To illustrate the technique, consider a warm atomic cell (between 30–100 °C)

with a weak **probe** propagating in it. If the atoms have a velocity profile, then atoms will see different frequencies depending on where and how they are moving; something we usually call *Doppler Shift* (Fig. 2.5.2 (a) & (c)). If we scan the laser in frequency, we will lose finer transitions due to the thermal noise. In this sense, we are limited to a certain resolution set by the Doppler broadening. For rubidium at room temperature this broadening is around 300 MHz, much larger than the natural linewidth of the D_2 transition (6 MHz).

To overcome this limitation, a counter-propagating, stronger **pump** beam is introduced along with the weak probe. The pump beam saturates a set of atomic transitions, while the probe measures the resulting absorption. This configuration produces the familiar Doppler-broadened background but, importantly, a narrow dip (*Lamb dip*) appears at the resonance frequency $\omega = \omega_0$ (Fig. 2.5.2 (b)).

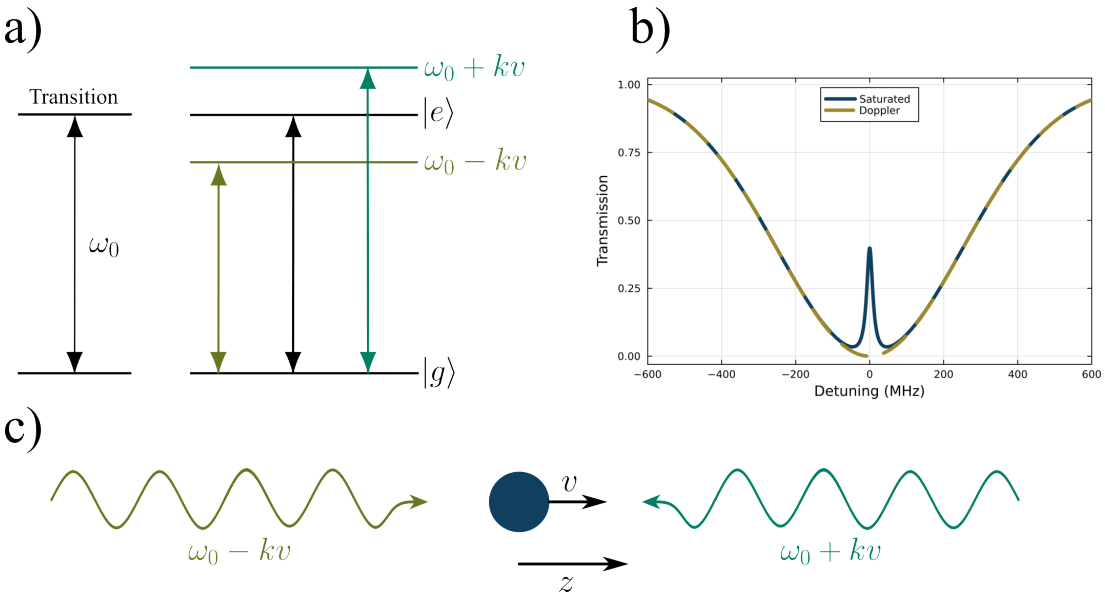

Figure 2.5.2: a) Energy level diagram for a two-level atom under Doppler shifts. The atom percieves an energy (frequency) shift of $\pm kv$ due to its motion with respect to the laboratory/laser frame. b) Transmission plots for a two-level atom showing both the Doppler profile and the saturated absorption peak centered at resonance, for a saturated absorption setup. c) Illustration of an atom with velocity v interacting with counter-propagating laser beams, resulting in opposite Doppler shifts.

The physical mechanism behind this dip is that the pump and probe interact with different velocity classes of atoms. While the probe absorption originates from atoms moving in one direction, the pump simultaneously depletes the population of atoms moving in the opposite direction. When both beams address the same

group of atoms (i.e., atoms with zero velocity relative to the laser), the transition saturates, leading to a reduction in probe absorption at the exact resonance. This feature provides the Doppler-free signature needed for precise frequency determination and laser frequency stabilization.

In addition to the central Lamb dips, crossover resonances can also appear. These arise when the Doppler-broadened profile of two nearby transitions (a common excited state for two ground states) overlaps. In this case, a particular velocity class of atoms can simultaneously satisfy resonance conditions for the probe on one transition and for the pump on another. As a result, the observed crossover resonance signal is typically stronger (often about twice the size of a normal transition dip) making it a specially useful reference feature in saturated absorption spectroscopy. Figure 2.5.3 shows experimental measurements obtained using a SAS setup, demonstrating the ability to resolve the hyperfine transitions across a range of temperatures.

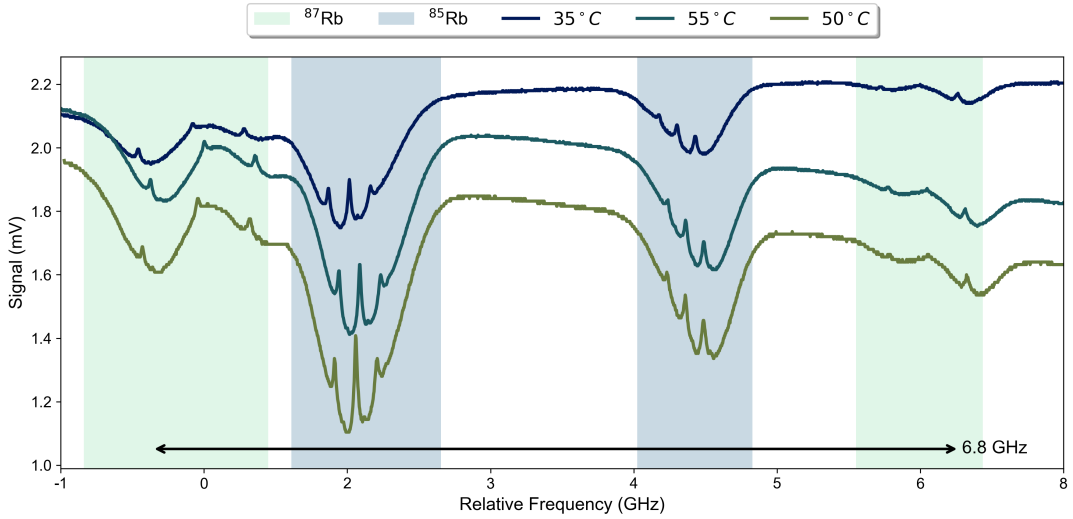

Figure 2.5.3: SAS signals obtained in an oscilloscope of part of the D1 line while the vapor cell is at different temperatures (changing then the number density of the atoms interacting with both the probe and pump). The detuning units are approximated to what the distance between these transitions should be. Special thanks to Sian McGarva, for completing the final data set that made this Figure. Frequency shifts seen near the edges of the figure in the hyperfine transitions are attributed to nonlinearities in the AOM response.

2.5.1.2 PID Locking

In order to control the modulation of the feedback (either the current or optical feedback), we borrow concepts from control theory. The most common approach for feedback systems is known as PID control, which stands for **Proportional, Integral and Derivative** control. Control signals are usually shown in the following form (Bechhoefer (2005)):

$$u(t) = k_P e(t) + k_I \int_0^t e(t)dt + k_D \frac{de(t)}{dt} \tag{2.5.1}$$

where k_P, k_I, and k_D are the parameters that would be tuned for a particular application. k_P is known as proportional feedback *gain*, and it will produce an output proportional to e(t), adjustable by its own value. k_I is the integral control gain, associated with the accumulated error over time, and is responsible for eliminating steady-state offsets, at the cost of potentially slower response. k_D corresponds to the derivative gain, determined by the slope of the error. This term provides a predictive correction that can improve stability and damp oscillations.

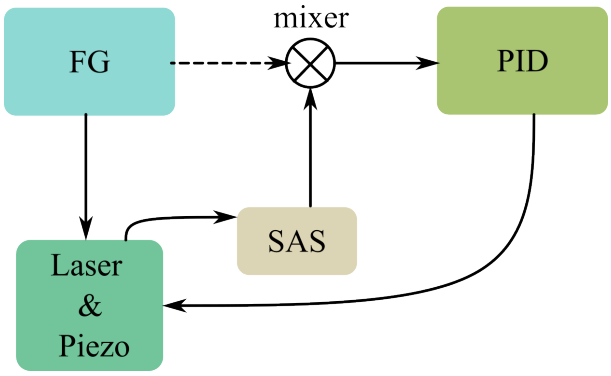

Figure 2.5.4: Feedback control loop for laser frequency stabilization. The dashed arrow represent the modulation and reference signals required for the SAS method. These components are absent schemes like DAVLL. FG is Function Generator. PID corresponds to Proportional-Integral-Derivative controller. SAS is the Saturated Absorption Spectroscopy setup.

The PID takes a calculated error signal $e(t)$ of a given set point with respect to its actual value, and will in turn produce a response $u(t)$, that goes back to the system of the laser current and the piezo (for optical feedback). PID control can be implemented using either analog electronics or digital microcontrollers.

In SAS setups, the mechanism for locking to a particular transition requires an

external reference (Fig. 2.5.4) generally given by a function generator (FG). A lock-in amplifier then takes the signal from the photodiode and multiplies it by a sinusoidal wave at the reference frequency. This provides a demodulated dispersive error signal, effectively generating the derivative of the absorption peak. After appropriate filtering, the required error signal is sent to the laser controller to make the correct adjustment (Mäusezahl et al. (2024)).

In contrast, in a DAVLL setup, we have the advantage that there is no particular need for a reference. Through applying a magnetic field and using a quarter-wave plate, one creates two overlapping absorption profiles that are slightly shifted. Subtracting the signals from two photodiodes produces a dispersion signal that crosses zero. This signal can be fed directly to a PID (Lee et al. (2011)).

2.6 A Quick Guide on Cooling Atoms

In this section I will briefly explain how we manage to cool a group of atoms (10^8) down to hundreds of a few hundred micro Kelvin. This is an essential for experiments in atomic physics, as cold atoms have paved a way for incredible discoveries such as Bose Einstein Condensates (Anderson et al. (1995)), precision atomic clocks (Ludlow et al. (2015)), quantum memories (Saglamyurek et al. (2018)), and so much more (Blumenthal et al. (2024)). The most popular procedure (but not the only one by far) to generate this cloud of atoms is called Magneto Optical Trapping, better known as MOT. While a MOT can typically cool atoms to the *Doppler limit* (a few hundred micro Kelvin for rubidium), one can make use of more than one mechanism, such as Sisyphus cooling, Raman sideband cooling and optical molasses; which in certain situations can help cool even further, down to nanokelvin scale. This means that on earth, we can effectively reach temperatures colder than those found in deep space.

The focus of this section will be to explain, in hopefully rather simple concepts from what we have discussed seen so far, how a MOT works[1]. For this goal, we will describe different processes that belong to the interaction and conclude with putting everything together to explain the MOT mechanism and hopefully illustrate why this has been revolutionary to understand light matter interactions.

2.6.1 Light Forces

When radiation interacts with matter, the process of absorption will generate a change in the momentum of the object associated to the force on the object. In order to calculate the forces that will appear in this interaction, we must be very deliberate with the Hamiltonian we choose to describe the system. In this particular case, we will consider the fact that the atom is not stationary, but rather moves as it interacts with the **resonant** light field ($\omega = \omega_0$). Speaking in a semi-classical framework, this movement will be described by the *center of mass* $\vec{\mathbf{R}}$, and momentum $\vec{\mathbf{P}}$ operators of the atom; and will appear as a kinetic energy term $\hat{\mathbf{P}}^2/2M$ in the total Hamiltonian.

The interaction between the internal atomic degrees of freedom and the incident

[1]For more details and further discussion, please refer to the amazing lectures given by Raul Celistrino Teixeira at the IV ICTP-SAIFR School on Light and Cold Atoms (2025).

light is described by the electric dipole interaction Hamiltonian; we commonly write this interaction as:

$$H_{\text{dip}}^{\text{inter}} = -dE_0 \cos(\mathbf{k}\cdot\mathbf{R} - \omega_0 t)(\hat{\sigma}_+ + \hat{\sigma}_-), \tag{2.6.1}$$

where d is the dipole moment of the transition, E_0 is the amplitude of the electric field, $\mathbf{k}$ is the wave vector of the light field, and $\hat{\sigma}_+$ and $\hat{\sigma}_-$ are the raising and lowering operators of the two-level atom. Through the Rotating Wave Approximation (RWA), and considering the atomic kinetic energy term, we can rewrite the total Hamiltonian of the system as

$$H_{RWA} = \hbar\omega_0 \left|e\right\rangle \left\langle e\right| + \frac{\hbar\Omega_0(\hat{\mathbf{R}})}{2}\left(e^{i(\phi(\hat{\mathbf{R}})-\omega t)}\hat{\sigma}_+ + e^{-i(\phi(\hat{\mathbf{R}})-\omega t)}\hat{\sigma}_-\right) + \frac{\hat{\mathbf{P}}^2}{2M}, \tag{2.6.2}$$

where $\Omega_0(\hat{\mathbf{R}}) = dE_0(\hat{\mathbf{R}})/\hbar$ is the position-dependent Rabi frequency, $\phi(\hat{\mathbf{R}}) = \mathbf{k}\cdot\hat{\mathbf{R}}$ is the position-dependent phase of the incident light field, and M is the mass of the atom.

From classical mechanics, and using the Ehrenfest theorem, we can relate the force on an object to the time derivative of the expectation value of its momentum operator:

$$F = \frac{d\langle\hat{\mathbf{P}}\rangle}{dt} = M\frac{d\langle\hat{\mathbf{V}}\rangle}{dt} = \frac{1}{i\hbar}\langle[\hat{\mathbf{P}}, \hat{H}]\rangle, \tag{2.6.3}$$

and calculate the forces on the atom due to the interaction with light:

$$\vec{F} = \frac{2\hbar}{\Omega_0(\mathbf{R})}\Delta\sigma_{ee}^{st}\vec{\nabla}_R\Omega_0(\mathbf{R}) + \hbar\Gamma\sigma_{ee}^{st}\vec{\nabla}\phi(\mathbf{R}), \tag{2.6.4}$$

σ_{ee}^{st} is the steady state solution of the bloch euations for the excited state population. Γ is the spontaneous emission rate of the excited state ($2\pi \times 6.05$ MHz for Rb^{D2}). This force contains two components, where the first one is usually called *Dipolar Force*; and the latter is known as *Radiation Pressure*.

The dipolar force corresponds to a conservative potential, is proportional to the gradient of the intensity of the light field, shown by the Rabi frequency Ω_0, and decays with the detuning as $1/\Delta$. This is the force responsible for the trapping of atoms in optical dipole traps. The radiation pressure, on the other hand, is proportional to the scattering rate of photons by the atom, and decays with detuning as $1/\Delta^2$. This force is responsible for the cooling of atoms in optical

molasses and magneto-optical traps.

2.6.2 Optical Molasses

Is the name given to the technique which uses counter-propagating beams in three orthogonal directions along the cartesian axes. These lasers all share the same frequency, which is slightly red-detuned from an atomic transition. Due to the Doppler effect, moving atoms will feel a slowing force (as if they were travelling in molasses) and stationary atoms with respect to the center where all lasers intersect will not feel any external force. Since the lasers are relatively close to resonance, the force comes from the radiation pressure term of the light forces discussed before. The force on an atom moving with velocity $\vec{v}$ due to two counter-propagating laser beams in 1D can be written as:

$$\vec{F}_{\pm} = \gamma_{\pm}\hbar\vec{k}_{\pm} = \pm\frac{1}{2}\frac{s_0\hbar\vec{k}\Gamma}{1+s_0+4((\Delta_0 \mp kv)/\Gamma)^2}, \tag{2.6.5}$$

where $s_0 = 2\Omega_0^2/\Gamma^2$ is the on-resonance saturation parameter, Δ_0 is the detuning of the laser from the atomic resonance, and $\vec{k}_{\pm}$ are the wavevectors of the two beams. The total force on the atom is then given by $\vec{F} = \vec{F}_+ + \vec{F}_-$.
The velocity capture range Δv of such a process is determined by the natural width Γ of the atomic excited state. As is, atoms will begin to accumulate slowly in the center of the trap. There is however a limit to how cold one can get atoms using only this method, known as the Doppler limit. This limit arises from the balance between the cooling force (radiation pressure) and the heating effect due to statistical fluctuations. The minimum achievable temperature, known as the Doppler temperature T_D for a number of dimensions D, is given by (Dalibard and Cohen-Tannoudji (1989)):

$$T_D^{min} = \frac{\hbar\Gamma}{2k_B}. \tag{2.6.6}$$

For a rubidium atom, since $\Gamma = 2\pi(6.05 \times 10^6)$ rad/s this temperature is around 140μK. To overcome this limit, an addition of polarization and magnetic field engineering makes this method much more effective, something we will know as Magneto-Optical Trapping.

2.6.3 Magneto-Optical Trap

As mentioned, the addition of a set of coils in anti-Helmholtz configuration manage to diminish the effects of any external magnetic field, and maybe most importantly, generate a magnetic field gradient outside the center of the trap. This gradient induces spatially varying Zeeman shifts in the atoms that are farther from the center. Adding then circular polarization of the counter-propagating beams ensures atoms preferentially scatter photons that push them back to the trap center. Although initially a warm atomic vapour is released inside the vacuum chamber that will hold the cold atomic cloud, it is this particular interaction of magnetic field and polarized radiation that will make the atoms distribute in velocity in the middle of the trap. The final size of the cloud is determined by the equilibrium between the magnetic restoring force and the thermal expansion of the atoms.

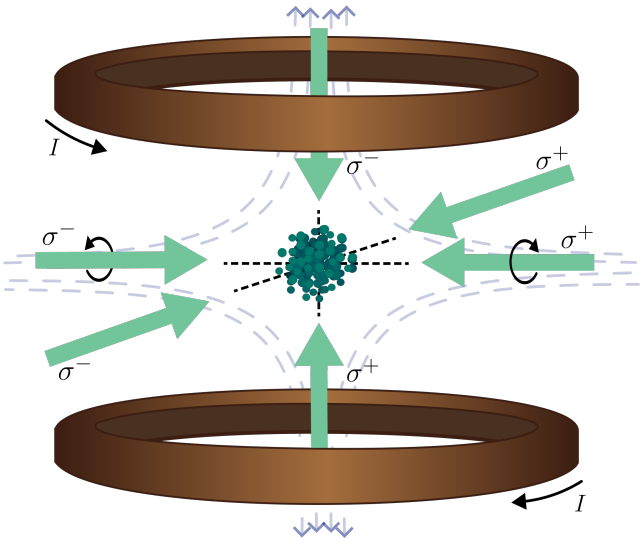

Figure 2.6.1: Illustrated mechanisms of a MOT. Two coild in anti-Helmholtz configuration generate a quadrupole magnetic field (dashed lines) with zero field at the centre. The intersection of this field with three pairs of counter-propagating, circularly polarized laser beams ($\sigma^{\pm}$) creates a position-dependent restoring force that confines the atoms.

3

Single Photon Generation in Cold Atomic Ensembles

Illinois

Sufjan Stevens

3.1 Introduction

In the following chapter, we present the work carried out during my internship at the University of Alberta, including the theoretical background and experimental feasibility of realizing a single photon source based on the DLCZ protocol. We begin by introducing the motivation for generating single photons in a cold atomic cloud, followed by a review of the concepts and theoretical tools needed to understand the contributions of this work. The performance of the DLCZ is then compared with a protocol meant to induce collective effects (specifically superradiance), highlighting the advantages and limitations of each. Finally, we show that the superradiant protocol provides faster operation and greater control over single-photon generation.

3.1.1 Motivation

Experimental sources for quantum computing as an area of research show great promise to drive forward communication and information science. As researchers, we seek for the technological advancements in these areas, because this means that fundamentally we can change the way we process information, build computers, and solve complex problems. As a more local example, the developments in quantum optics technologies have allowed Chilean researchers to develop the first real random number generator based on quantum optics, which is now being used in the Chilean National Lottery (Iturra (2023)). This is only one of many

examples of how quantum technologies can be used to improve our daily lives and how they can be used to create new tools that can make our life easier.

In particular to quantum communication through optics, a well-known area of active research is currently being done on studying Quantum Key Distribution (QKD), one of the most famous quantum cryptography protocols, envisioned to provide safe communication channels using entanglement of photons. These channels would be safe from an intermediary between a sender and a receiver, since, due to the collapse of the wavefunction during measurements, the intermediary would not be able to measure the photons without disturbing them (no-cloning theorem). However, this of course is not as safe as promised by theory; until recently, QKD was based on an attenuated coherent light as a medium for transfer of information, but these light sources have imposed a limit on the secure key rate (SKR) per channel use. This limit corresponds to the scarcity of single-photon components within coherent light, inherently bounded by a maximum of $1/e$. This limit is surpassed in single photon realizations of the QKD protocol, as seen in (Zhang and Ding (2025)).

It becomes clear then, that single photon sources are a key technology that can drive forward not just quantum science, but quantum computing and technologies alike (Couteau et al. (2023)). This, among many other potential benefits, is why we seek to build a single photon source based on the DLCZ protocol, which has been shown to be an efficient and controlled way of generating single photons in atomic media. Before discussing the protocol itself, we will review some of the theoretical tools needed to understand the process.

3.2 Statistics of Light and Quantum States of Light

A foundational step in the area of quantum optics began from studying the statistics of light, allowing us to distinguish classical from genuinely quantum behavior (Fox (2006)). In particular, photon-counting measurements reveal the statistical distribution of detected photons, allowing light fields to be classified according to their photon-number statistics.

Light can then be classified into: Poissonian, sub-Poissonian, and super-Poissonian distributions, based on the statistics of photon counting through detectors. Poissonian and super-Poissonian (classical) states can be described by classical

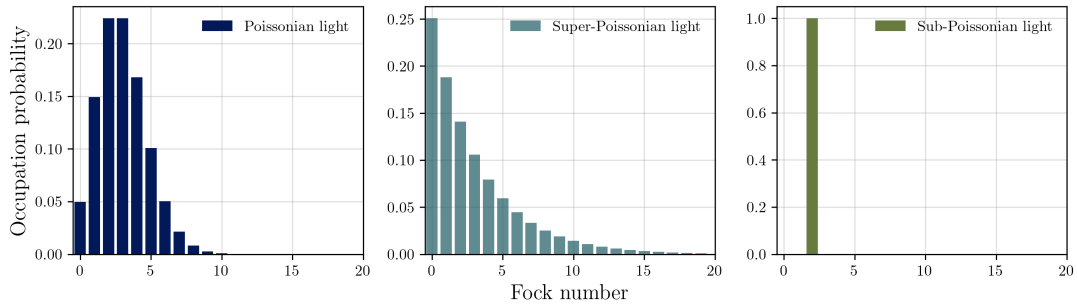

Figure 3.2.1: Three possibilities for the photon statistics, for different states of light. From left to right, these are the statistics for a coherent state and a thermal state with $\bar{n} = 3$, and a Fock state with $\bar{n} = 2$. Figure made with QuTiP.

electromagnetic theory, while sub-Poissonian (non-classical) states exhibit quantum features that cannot be explained classically (see Fig. 3.2.1). The Poissonian distribution is given by the expression:

$$P(n) = \frac{e^{-\bar{n}}\bar{n}^n}{n!} \tag{3.2.1}$$

Where n can be $0, 1, 2, 3, ...$, meanwhile $\bar{n}$ is the average photon number. This distribution has the property that the variance is equal to the mean, $\Delta n = \sqrt{\bar{n}}$.

These definitions allow us to separate the three possible statistics for light:

* Sub-Poissonian: $\Delta n < \sqrt{\bar{n}}$.
* Poissonian: $\Delta n = \sqrt{\bar{n}}$.
* Super-Poissonian: $\Delta n > \sqrt{\bar{n}}$.

However, this statistical classification is not enough to fully characterize quantum states of light, since distinct quantum states may share identical photon-number statistics while also differ in their phase properties, correlations, or nonclassical features. Therefore, in the following sections we will introduce a selection of relevant, well-known quantum states of light, specifically coherent states, Fock (number) states, thermal states, and squeezed states—and discuss their key properties in the context of photon statistics and optical coherence. Among these, special emphasis will be placed on the single-photon state, as the main goal of this chapter is to study the generation and characterization of this state.

3.2.1 Library of Optical Quantum States

3.2.1.1 Coherent States

The coherent state $|\alpha\rangle$ is an eigenstate of the annihilation operator $\hat{a}$, representing the quantum state of light most closely resembling a classical electromagnetic wave, most commonly associated with that produced by an ideal laser. It is defined as:

$$\hat{a}_i |\alpha_i\rangle = \alpha_i |\alpha_i\rangle \tag{3.2.2}$$

where α_i is a complex amplitude associated with mode i. Expanding $|\alpha\rangle$ in the Fock basis yields

$$|\alpha\rangle = e^{-|\alpha|^2/2} \sum_{n=0}^{\infty} \frac{\alpha^n}{\sqrt{n!}} |n\rangle \tag{3.2.3}$$

where mean photon number is given by $\langle \hat{n} \rangle = |\alpha|^2$. The photon number distribution follows a Poissonian form. Consequently, coherent states satisfy $\Delta n = \sqrt{\langle \hat{n} \rangle}$ and represent the **boundary between classical and nonclassical photon statistics**. For this reason, although they are often regarded as classical states of light, they are pure quantum states (shown by the fact that they can show entanglement when interacting with other quantum systems Berezhiani and Zantedeschi (2021)).

3.2.1.2 Fock States (Number States)

Fock states are quantum states with a well-defined number of photons, denoted as $|n\rangle$, where n is the exact number of photons in the state. These states are eigenstates of the photon number operator $\hat{n} = \hat{a}^\dagger \hat{a}$:

$$\hat{n}_i |n_i\rangle = n_i |n_i\rangle \tag{3.2.4}$$

where $\langle \hat{n} \rangle = n_i$. The probability $P_{Fock}(n)$ to find n_i photons in one mode is either 1 for $n = n_i$ or 0 for $n \neq n_i$. This means that since the photon number of a Fock state is determined, the state is intrinsically quantum. As such, the probability distribution of the photon number follows a sub-Poissonian distribution (with a photon variance of zero in ideal conditions).

3.2.1.3 Thermal States

The thermal state originates from blackbody radiation (such as light coming from the sun) and is characterized by a statistical mixture of photon-number states. These states are indeed intrinsically mixed and lack a well-defined phase. To describe a thermal state one can use the density operator formalism, expressing it as an incoherent statistical mixture of photon-number states:

$$\hat{\rho}_{thermal} = \sum_{n=0}^{\infty} P_n(n)|n\rangle\langle n| \tag{3.2.5}$$

These states exhibit super-Poissonian photon-number fluctuations, characterized by a variance $\Delta n > \sqrt{\bar{n}}$. This enhanced noise reflects photon bunching and strong intensity fluctuations, distinguishing thermal light from both coherent and number states.

3.2.2 Correlation Functions

Photon-number statistics provide an indication of the nature of a particular light field; however, they are not enough to let us distinguish between different quantum states. For example, weak coherent states (with low mean photon number) may exhibit photon number distributions that resemble those of Fock states. Despite this apparent similarity, these states differ fundamentally; this becomes evident when looking at correlation functions. These functions allow us to quantify the statistical correlations between field amplitudes $I(\mathbf{r}) = \langle |E(\mathbf{r}, t)|^2 \rangle$ measured at different points in space and time. They can be formulated within both classical and quantum frameworks; however, we adopt the simplest expressions that capture the essential physical behavior relevant to the characterization of single-photon sources.

3.2.2.1 First Order Correlation Function

The first order correlation function describes the coherence of an optical field between a spatial coordinate $\mathbf{r}_1$ and $\mathbf{r}_2$, and time coordinate t_1 and t_2. The magnitude of this function relates to the visibility of interference fringes observed in interferometers.

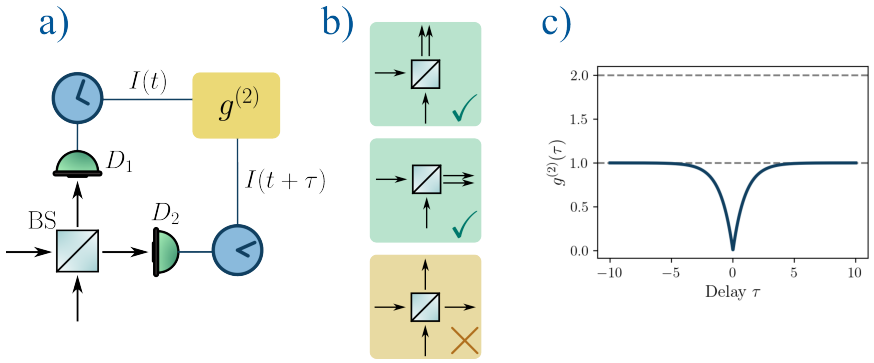

Figure 3.2.2: a) Hanbury Brown and Twiss (HBT) interferometer used to measure the second-order correlation function $g^{(2)}(\tau)$ via photon coincidence detection. b) Hong-Ou-Mandel (HOM) effect demonstrating two-photon interference at a 50/50 beamsplitter, resulting in coincidence suppression for indistinguishable photons. c) Expected measurements for the HBT interferometer once a single photon source is measured; due to the fact that the single photons must be indistinguishable, the HOM effect gives us a second order correlation function equal to 0. Figure inspired partly by Couteau et al. (2023)

$$g^{(1)} = \frac{\langle E^*(r_1,t_1)E(r_2,t_2)\rangle}{\sqrt{\langle|E(r_1,t_1)|^2\rangle\langle|E(r_2,t_2)|^2\rangle}} \tag{3.2.6}$$

For a perfect coherence, the interference fringes will have high contrast, and so $|g^{(1)}| = 1$. For smaller values, one would observe a partial fringe visibility, and for $|g^{(1)}| = 0$ there will be no contrast in the interferometer's fringes, so there will be no coherence.

3.2.2.2 Second Order Correlation Function

The second-order correlation function fundamental role in the identification of non-classical photon sources (Aspect (2019), Hadfield (2009)), also refered to as the intensity autocorrelation function of a source. Experimentally, it is most commonly measured using the Hanbury-Brown-Twiss (HBT) interferometer, shown in Fig.3.2.2(a), which consists of a 50/50 beamsplitter followed by two single-photon detectors.

In the HBT configuration, the incoming optical field is divided into two spatial modes by a 50/50 beamsplitter. The two detectors will trigger or not depending on the arrival of a photon, and the coincidence rate between detection events at the two output ports is recorded as a function of the temporal delay τ between

detections. The normalized second-order intensity correlation function is defined as

$$g^{(2)}(\tau) = \frac{\langle I(t)I(t+\tau)\rangle}{\langle I(t)\rangle^2} \tag{3.2.7}$$

This then allows us to obtain a new characterization for light based on its 'bunchiness':

* Bunched light: $g^{(2)}(0) > 1$.
* Coherent light: $g^{(2)}(0) = 1$.
* Anti-bunched light: $g^{(2)}(0) < 1$.

Now, there is a need to corroborate that the single photons emitted in different processes are indeed identical, and for this one makes use of an effect known as the Hong-Ou-Mandel (HOM) effect, which is a two-photon interference phenomenon that occurs when two *indistinguishable* photons enter a 50/50 beamsplitter from different input ports. If the photons are perfectly indistinguishable in all degrees of freedom (temporal, spectral, spatial, and polarization), they will interfere destructively in the coincidence channel, leading to both photons exiting through the same output port (Fig.3.2.2(b)).

When measuring an ideal single photon source with the HBT interferometer, the HOM effect ensures that no coincidence counts are detected at zero time delay, since a single photon cannot be split into two paths. This results in a suppression of coincidence counts at time 0, seen in Fig.3.2.2(c).

3.3 Single Photon Generation

In order to understand the mechanisms that allow for the generation of single photons in this case, we must understand that there are many ways in which one can create single photons. A few examples are basic two level systems such as quantum dots, nonlinear processes such as spontaneous parametric down conversion (SPDC) or spontaneous four wave mixing; or through defect centers in solids, between many others (Lounis and Orrit (2005)). As a consensus (Zugenmaier (2018)), these sources are divided in two categories, probabilistic and deterministic. For the applications in quantum technologies, one would most commonly prefer to rely on deterministic sources, that would deliver single photons on demand; these types

of sources are neither common nor easy to apply, and as such, intense research has been conducted the past 20 years to find such a deterministic (and efficient) source. On the other hand, probabilistic sources are based on a photon-pair emission (e.g. SPDC), where one of the photons is used to herald the other. As one can expect, these are much easier to come by and are the most commonly used.

3.3.1 Raman Process

A fundamental part of the now-famous DLCZ protocol is the Raman process, also known as Raman scattering. This corresponds to the inelastic scattering of light when interacting with either atoms or molecules, resulting in a transfer of energy between the photon and the matter. This inelastic transfer results in a shift of the photon's energy; the emitted components shifted to lower frequencies are called Stokes components, while those shifted to higher frequencies are known as anti-Stokes components.

Beyond its use in quantum memories, the Raman process is a versatile tool in quantum optics. It can be used to generate non-classical states of light, such as squeezed states (Knight (1986)). These processes are also highly advantageous for spectroscopy and state manipulation, as they allow for the study of "forbidden" transitions. By utilizing a two-photon process through an intermediate virtual or excited state, one can drive transitions between two states of the same parity that are otherwise inaccessible via single-photon electric dipole transitions.

Although Raman scattering is most efficient for higher intensities (Boyd (2020)), the spontaneous Raman scattering process is effective even at the single-photon level. This is the regime utilized in the DLCZ protocol and is of particular interest to our work. In a typical thermal equilibrium, the Stokes emission is higher than the anti-Stokes emission because the latter requires the atom to already be in an excited state, which has a much lower population compared to the ground state.

In particular to our case, we will be focusing on a spontaneous raman process in a Λ configuration (see Fig. 3.3.1), where the atom starts in a ground state $|g\rangle$, is excited to a virtual intermediate state close to the excited state $|e\rangle$ through the interaction with a write beam, and then spontaneously decays to a different ground state $|s\rangle$, creating then a spin wave excitation that is stored, while emitting a Stokes photon. This process is non-resonant; the write beam is detuned from the

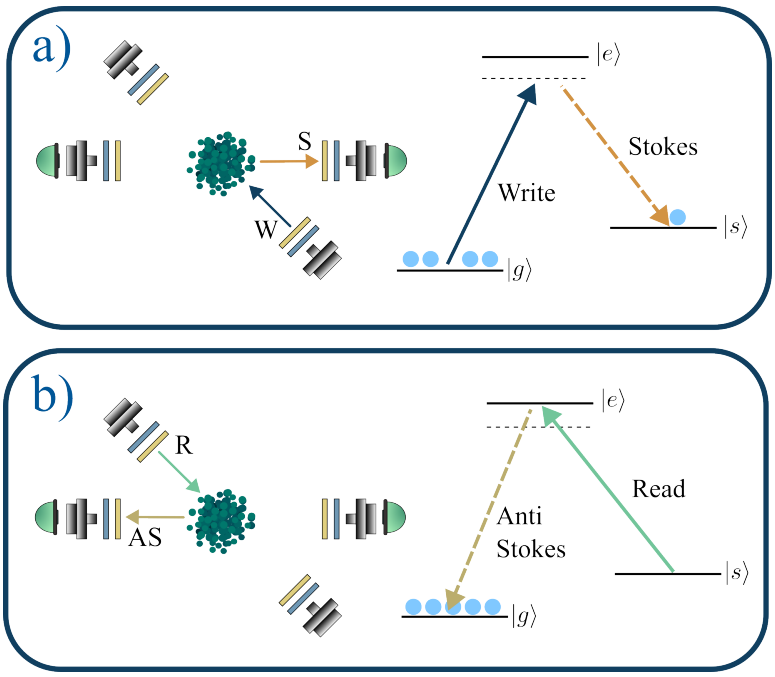

Figure 3.3.1: Illustration of the DLCZ protocol for single photon generation.

$|g\rangle - |e\rangle$ transition by a certain amount Δ. This detuning reduces the possibility of spontaneous emission from the excited state, increasing the coherence time of the process. The mometum conservation equation for the Raman process is given by:

$$\boldsymbol{k}_{out} = \boldsymbol{k}_{in} - \boldsymbol{k}_{write} + \boldsymbol{k}_{read}. \tag{3.3.1}$$

3.3.2 Duan-Lukin-Cirac-Zoller Protocol

Better known as DLCZ protocol, was initially proposed by Duan et al. (2001). This protocol proposes a spontaneous Raman scattering process to generate a heralded photon presenting as a single excitation stored in an atomic ensemble. Although initially proposed as a scheme for quantum repeater technologies for remote entanglement and long distance quantum communications, this scheme has proven to be highly efficient in deterministic single photon generation (Farrera et al. (2016), Sangouard et al. (2007)).

The protocol is implemented using an ensemble of N identical atoms in a Λ-configuration is prepared in the ground state $|g\rangle$. A short off-resonant optical pulse (*write*) induces the Raman transition close to the $|g\rangle - |e\rangle$ transition. This results in the isotropic emission of a Stokes photon and the creation of a spin-wave

excitation that is stored in the ensemble in an intermediate state $|s\rangle$.

Since it is not possible to know which atom from the ensemble stores the excitation, the system can be written as a superposition:

$$|\Psi\rangle = \frac{1}{\sqrt{N}} \sum_{j=1}^{N} e^{i\vec{k}\cdot\vec{r}_j} |g_1, g_2, \ldots, s_j, \ldots, g_N\rangle \,, \tag{3.3.2}$$

where the summation is taken over all the atoms. This is what is known as a collective spin excitation, or spin-wave excitation.

The stored excitation can later be extracted using a second, strong beam (*read*), which drives the $|s\rangle - |e\rangle$ transition resonantly, and induces the emission of an anti-Stokes photon, which is emitted in a correlated direction and polarization given by the Stokes photon and the conservation of momentum.

The efficiency of this protocol relies on constructive interference. Once the read beam satisfies the phase matching condition, the phase adquired by the superposition (Eq. 3.3.2) will interfere constructively and enhance the read transition, and the anti-Stokes photon will be emitted into a well-defined spatial mode with high probability.

It is then straight forward to think of this process as a controllable and deterministic single photon source. If one is able to control the Raman process, the Stokes photons will herald information of stored single photons that can be recalled on-demand via a read pulse and then immediately used on subsequent stages of any other application.

While this has been studied on its own as an effective protocol to generate single photons, this work focuses on methods to optimize its retrieval efficiency via collective effects. For this we reference the work by Laurat et al. (2006) and investigate how collective emission (via superradiance in this case) can improve the performance of the source compared to the traditional DLCZ scheme.

3.3.3 Superradiance

Superraddiance is a collective effect that originates from the indistinguishability of the atoms in an ensemble, leading to an enhanced emission rate in a specific direction. This effect was first described in Dicke (1954), and has since been

studied theoretically extensively in various systems. However, its application to quantum technologies has gained significant attention in recent years, since it can enhance the efficiency of photon emission and retrieval processes. Pulse optimization for quantum memories has been done by Gorshkov et al. (2007) and most recently by Shinbrough and Lorenz (2023), where they showed that the optimal pulse shape can significantly enhance the retrieval efficiency of single photons from atomic ensembles.

In the context of the DLCZ protocol, superradiance will play a crucial role in the efficient retrieval of the stored excitation as a single photon; reducing the time it takes for the anti-Stokes photon to be emitted, and increasing the probability of its emission in the desired mode. This is particularly important for quantum communication applications, where high efficiency and low loss are essential.

The optimal shape of a probe for a lorenztian spectral feature such as seen in rubidium is the exponential rising envelope. With a duration given by Ho et al. (2018), Vivoli et al. (2013),

$$T_P^{opt} \approx \frac{1}{\Gamma}\left(\frac{1}{1+d/4}\right). \tag{3.3.3}$$

The characteristic timescale of superradiant emission is inversely proportional to the optical depth of the medium. As a result, for optical depths larger than unity (which is the case for cold atomic clouds such as the one realized), the collective decay can occur on timescales much shorter than the natural lifetime of the atomic excited state. Moreover, it has been shown by Rastogi et al. (2022) that superradiant-based protocols impose more relaxed optical depth requirements compared to other quantum memory schemes, making them particularly attractive for practical implementations.

3.4 Experiment

The experiment was developed over several years by the team and students of the Cold Atoms lab's at the University of Alberta. Therefore, many omitted details will be available in the past student's theses such as Anindya's (M.Sc. Rastogi (2018), Ph.D. Rastogi (2024)), and Andrei's Tretiakov thesis (M.Sc. Tretiakov (2016)). The core of the experiment is, of course, the rubidium 87 chamber in the

middle of the table, under an ultrahigh vacuum. Rubidium atoms are supplied into the chamber by a metallic dispenser, which is resistively heated, releasing pure rubidium vapor through the decomposition of specialized salts within the dispenser. Once the atoms are in the chamber, they undergo a cooling process,

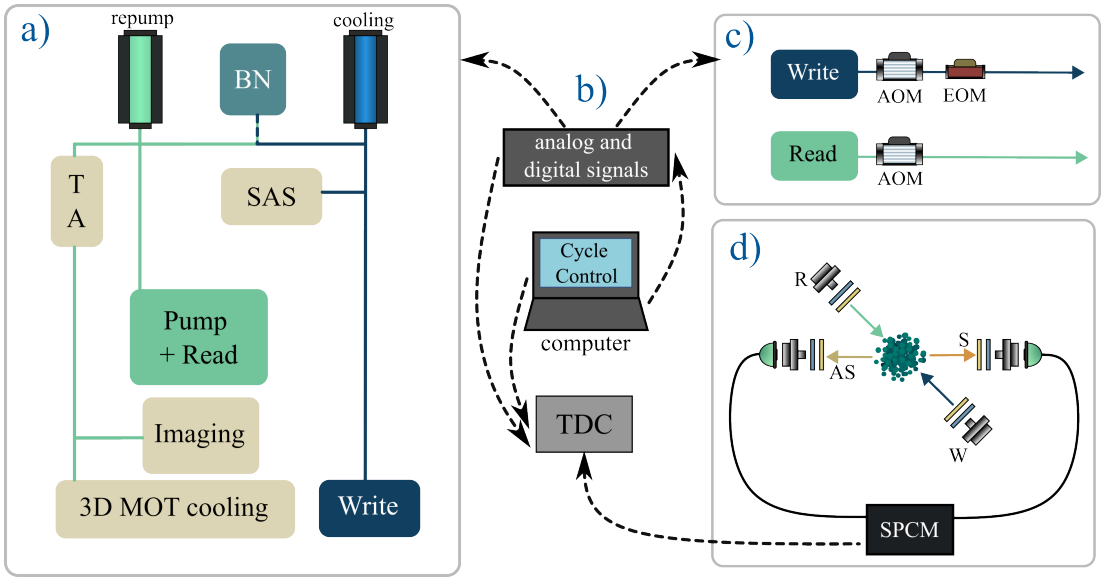

Figure 3.4.1: Illustration of the experimental set-up.

which is done via MOT, followed by an optical molasses stage (see Figure 3.4.2 for the experimental cycle). The MOT provides initial spatial confinement and high collection efficiency, while the subsequent optical molasses step further cools the atoms to temperatures around 30μK. For the MOT, a pair of coils in an anti-Helmholtz configuration are used to generate a weak quadrupolar magnetic field. The coils are separated along the z-axis In the proximity of the field zero, located halfway between the two coils along the z-direction, the field gradient is uniform and the field itself varies linearly with displacement from the field zero. Added to this, there are three pairs of smaller coils (*biases*) used to control where the atomic cloud will be formed and positioned in every cycle. An average number of atoms is a number between 2×10^7 to 1×10^8. This can be controlled by changing the time our MOT takes to build up, or by changing the time of flight.

In a separate optical table, we find the laser system with all locking electronics. Two diode lasers are used in the setup; a *Moglabs* Diode Laser (*repump laser*) with its controller and a *Toptica* 780 Laser (*cooling laser*) with its own *Digilock* 110. The repump laser is sent in part to a SAS setup for frequency stabilization, while other parts are used to lock the cooling laser via a beatnote detection, and sent

in part to the cooling beam path, and finally sent in through two acousto-optic modulators (AOM) to create the write beam. The repump laser is locked to the cooling laser via a beatnote detection, and its frequency is controlled via PID control. It's power in part sent to both the optical pumping and read beam, and is then amplified via a THORLABS tapered amplifier (TPA780P20) which takes around 5mW input and outputs around 300mW in the frequency needed. This power is mainly used for the cooling beams of the MOT, while a small part goes to the imaging of the atomic cloud.

We work in a lambda configuration around the D2 line of rubidium 87, as seen in Figure 3.3.1. We engage the following levels; for the ground state $|g\rangle = |^2 5S_{1/2}, F = 1\rangle$, the long-lived state $|s\rangle = |^2 5S_{1/2}, F = 2\rangle$ and the excited state $|e\rangle = |^2 5P_{1/2}, F' = 2\rangle$. As seen in Section 2, $|g\rangle$ and $|s\rangle$ are spaced by 6.83 GHz. The pulses from the read and write probes are shaped and "cut" by both AOM's

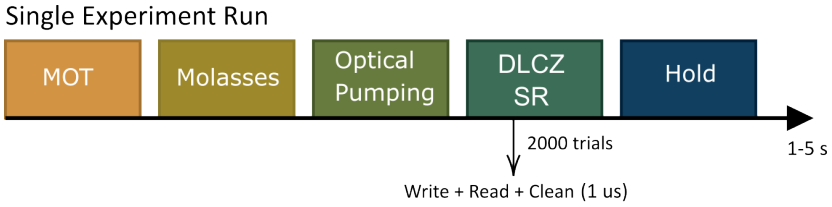

Figure 3.4.2: Illustration of the experimental cycle for data acquisition.

and shutters in the setup. After this, an electro-optic modulator (EOM) shapes the *write* pulse. All these are controlled by an arbitrary waveform generator (AWG) and synched by a cycle control program. The write and read pulses are separated by a 50° angle. This allows the filtering of scattered control noise. The beams have a $1/e^2$ Gaussian diameters of around 3 mm. With a number of around 10^9 atoms, the peak optical depth is around $d = 9$.

For the measurement of the Stokes and anti-Stokes photons, we use single photon detectors (Excelitas SPCM 780 24 FC). Once the photons reach the detectors, a time-to-digital converter (TimeTagger 20) measures the time between each start Stokes photon and stop anti-Stokes photon. Accounting for fiber coupling and detector inefficiencies, the total photon loss for the Stokes and anti-Stokes channels is approximately 2.2%. Correlation statistics are accumulated into 40,000-bin histograms with a bin width of 25 ns, and data is filtered into write and read windows for analysis (see Section 3.4.1).

3.4.1 Measurements

We did not have available all neded single photon detector modules to characterize the second-order autocorrelation function, as such, what we have characterized in the figures shown in 3.5.1 and the appendix for this section (Appendix A.1), are the correlation and other characteristics arising from measuring the Stokes and anti-Stokes photons emmited from the protocol in both their DLCZ and superradiant versions.

Therefore, the second order correlation calculated and shown in this work is defined by:

$$g^{(2)}_{S,AS}(\tau) = \frac{\langle \eta_S(t)\eta_{AS}(t')\rangle}{\langle \eta_S(t)\rangle\langle \eta_{AS}(t')\rangle}. \tag{3.4.1}$$

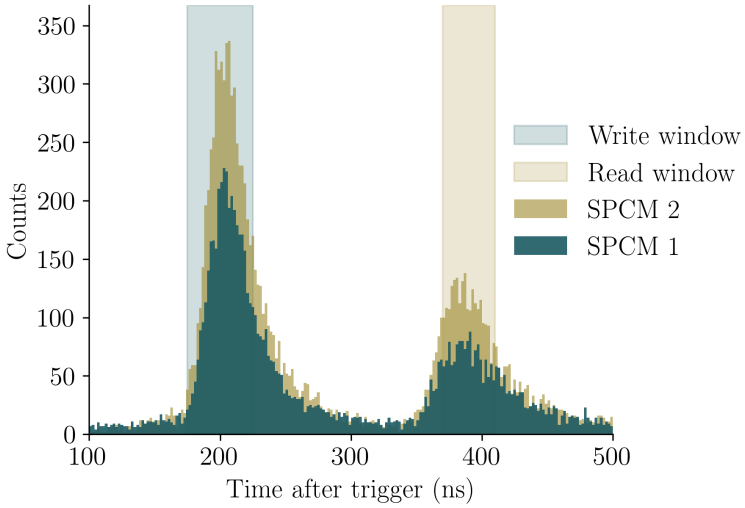

Figure 3.4.3: Experimental trial for data acquisition.

The photon detection data (Fig. 3.4.3) is analyzed by first separating events according to their detection channel, associated to two different single photon detectors that measure the scattered photons. Detection times are referenced to the experimental trigger given by the analog and digital signals sent from the control system (Fig. 3.4.1) and converted to nanoseconds. Stokes photons are then selected within a predefined write window, while anti-Stokes photons are filtered within a read window, defined by the expected width of the write pulse, and shifted by the write (read) pulse delay and a small temporal tolerance. Coincidences are identified by matching events that occur within the same experimental trigger within each trial, accounting for all possible Stokes (anti-Stokes) combinations.

From the total number of detected Stokes photons, anti-Stokes photons, and coincidences, the second-order cross-correlation function $g^{(2)}_{S,AS}(\tau)$ is calculated. Accidental coincidences are estimated by correlating Stokes detections with anti-Stokes detections from temporally shifted trials, allowing for the extraction of corrected coincidence probabilities and the conditional readout efficiency.

We have calculated the spinwave generation probability, which is defined as the probability of having a spinwave excitation in the atomic ensemble per write pulse. This is calculated as:

$$p_{sw} = \frac{N_{Stokes}}{\eta_S N_{trials}} \tag{3.4.2}$$

where N_{Stokes} is the number of detected Stokes photons, η_S is the total detection efficiency for the Stokes channel, and N_{trials} is the total number of write trials.

The coincidence generation probability, which is defined as the probability of having a coincidence detection event (Stokes and anti-Stokes photon detected) per write pulse. This is calculated as:

$$p_c = \frac{N_{Coin} + N_{acc}}{\eta_S \eta_{AS} N_{trials}} \tag{3.4.3}$$

where N_{Coin} is the number of detected coincidence events, N_{acc} is the number of accidental coincidences, η_{AS} is the total detection efficiency for the anti-Stokes channel, and N_{trials} is the total number of write trials.

Finally, we calculated the conditional retrieval efficiency, which is defined as the probability of retrieving an anti-Stokes photon given that a Stokes photon has been detected. This is calculated as:

$$\eta_R = \frac{N_{Coin}}{N_{Stokes}} \tag{3.4.4}$$

where N_{Coin} is the number of detected coincidence events, and N_{Stokes} is the number of detected Stokes photons.

3.5 Results

In the present section we will show a comparison of the measurments described in Section 3.4.1 for both the DLCZ and SR protocols. The results shown here were obtained using a read power of 1.5 mW, with a varying write power. We can see

in Figure 3.5.1 that the superradiant protocol outperforms the DLCZ protocol in all measured aspects; spinwave creation probability, coincidence probability, and conditional readout efficiency. We believe this is due to the collective enhancement of the read process, which allows not only for a more efficient retrieval of the stored excitation, but also a faster emission of the anti-Stokes photon, reducing the likelihood of decoherence during the retrieval process, which can be seen in the conditional retrieval efficiency and the second order correlation function. The results for other read powers can be found in Appendix A.1.

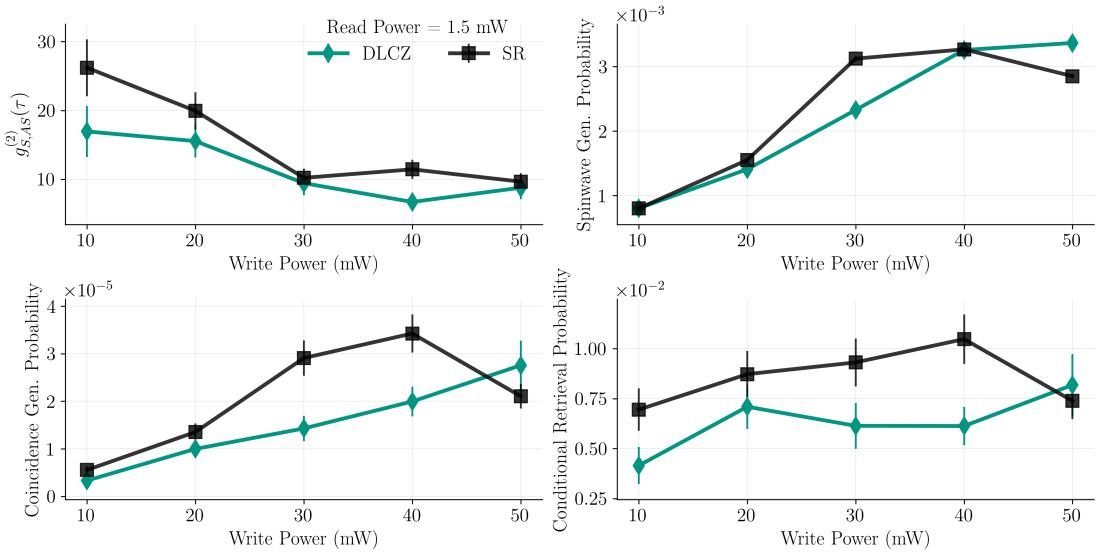

Figure 3.5.1: DLCZ vs Superradiance protocol with a read power of 1.5 mW.

An important point to consider is that due to the fact we are collectively storing excitations in the atomic ensemble, not all photons measured in the read window will belong to the anti-Stokes photons emitted from the stored excitation. There will be noise photons, coming from spontaneous emission or excitations that were not successfully recalled that are spontaneously emitted in different trials. In order to confirm that statistically the photons are correlated in the correct window, we look at different trials within a range, and calculate the second order correlation function $g^{(2)}_{S,AS}(\tau)$ as explained in Section 3.4.1. This gives us a histogram of the time delay between Stokes and anti-Stokes photons, once a Stokes photon has been detected.

In Figure 3.5.2 we notice two important features. First, the superradiant protocol has a higher peak, indicating a higher correlation between Stokes and anti-Stokes photons, which is consistent with the results shown in Figure 3.5.1. This is

consistent with the idea that superradiance enhances the emission rate of the anti-Stokes photon, leading to a faster retrieval process. Second, in both cases, there is a peak in the 200 ns bin, which is consistent with the delay between the write and read pulses in the experimental cycle (Figure 3.4.2).

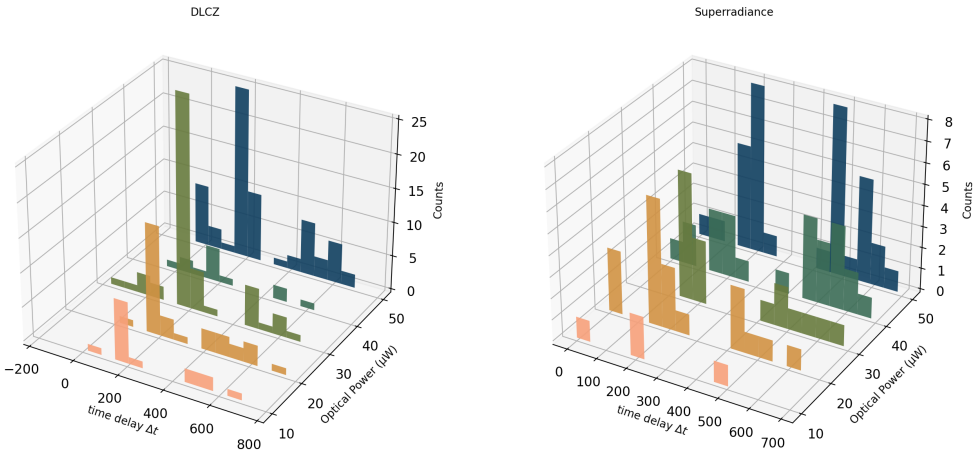

Figure 3.5.2: DLCZ vs Superradiance protocol. For each detected Stokes photon, all anti-Stokes detections occurring within the **same experimental trigger** are considered, and the time difference between their detection times is calculated. This procedure yields a distribution of Stokes to anti-Stokes time delays, which is plotted here to analyze photon bunching and temporal correlations between the two processes.

3.6 Conclusions and Comments

We have shown in this work that the correlations between Stokes and anti-Stokes photons arising from the DLCZ protocol and from the superradiance protocol have similar behaviors for the parameters studied. However, the superradiance protocol shows promising performance in terms of all characteristics studied for the same read power. We believe this is mainly due to the collective enhancement effect present in the superradiance protocol, which allows for a more efficient retrieval of the anti-Stokes photon.

In particular, we have observed that for read powers of 1.0 mW, 1.5 mW, and 2.0 mW, the superradiance protocol mainly outperforms the DLCZ protocol in both retrieval efficiency and correlation values. This suggests that the superradiance

protocol is more robust to variations in read power, making it a more reliable choice for applications requiring high-fidelity single-photon generation.

This work also confirms the generally stated fact that lower powers tend to give higher correlation values, at the cost of lower retrieval efficiencies. A crucial factor for optimizing single-photon sources for specific applications, such as quantum communication and quantum computing.

As one can see from Fig A.1.1, there exists a big experimental difficulty associated to measuring the SR protocol at low write powers, due to the low count rates obtained. There could be hours of data and not enough photon detections to calculate $g^{(2)}$. This is something that needs to be improved in future iterations of the experiment.

Additionally, this work could benefit from further characterization of the temporal profile of the emitted anti-Stokes photons in both protocols, and exploring the effects of varying other parameters such as optical depth of the atomic cloud. This would provide a more comprehensive understanding of the advantages and limitations of each protocol, and help to identify optimal operating conditions for practical implementations.

Finally, calculating the actual second order autocorrelation function $g^{(2)}(0)$ for anti-Stokes photons after measuring a Stokes photon would confirm the quantum nature of the emitted light in both protocols, and provide a more direct comparison of their single-photon characteristics.

4

Quantum State Tomography through Atomic Mirrors

Let's Dance Raw

Shintaro Sakamoto

4.1 Introduction to Quantum Mirrors

The ability to exert precise control over propagation and scattering of light has been a particular interest in quantum optics and technologies (Hammerer et al. (2010)), and as such, it has motivated extensive research into the development of devices capable of controlling optical reflection while minimizing losses (Hétet et al. (2011a); Marte et al. (1991)). While light scattering by individual atoms is often stochastic, it has been shown that *collective effects* in atomic ensembles can enable coherent scattering of light, allowing for the engineering of highly efficient atomic-thin mirrors (Shahmoon et al. (2017),Micheli et al. (2004); Rui et al. (2020)). Furthermore, the reflectivity of these interfaces can be actively controlled through techniques such as Electromagnetically Induced Transparency (EIT) and Rydberg blockade interactions (Srakaew et al. (2023); Srakaew (2024); Bekenstein et al. (2020)).

In this work, we extend the concept of a controllable mirror to define a *Quantum Mirror* (QM). Unlike the former, this device is capable of existing in a coherent superposition of reflective and transmissive states. This superposition, alongside the phase differences induced in the participating modes, generates non-trivial light-matter interactions of the device with the incident radiation fields, projecting their quantum state onto the mirror's medium itself.

A difficulty arises when considering the fact that collective atomic systems will not be easily prepared in such coherent superposition states. In this case, the

superposition is feasible via the entanglement of the ensemble with a controlling ancilla atom (Srakaew et al. (2023)), although other approaches could also be considered, such as macroscopic spin squeezing (Bornet et al. (2023)).

Due to the controllable interaction between the QM and incident light fields (that is, the projection of the radiation state onto the atomic medium), this device has profound implications for quantum metrology and information processing. The ability to measure an optical quantum state indirectly opens a door of possibilities for non-destructive quantum state tomography (QST). Additionally, the versatility of the QM has demonstrated potential in various quantum information protocols, including quantum teleportation (Uria et al. (2026)).

In this chapter, we turn our focus to questioning how is it exactly that one might be able to characterize generated or even transported quantum optical fields. We have shown already the importance of correlation functions in Chapter (3), but also discussed the relevance of more complete characterizations in the case of light with quantum characteristics, such as the Wigner function (WF) (see Section 4.2.0.3). In what follows, we will dwelve into *what is* tomography, why it is so computationally and experimentally resource intensive and present a novel protocol based on QMs that seeks to ease these difficulties.

4.2 Quasiprobability Distributions

Since the early days of quantum mechanics, physicists all over the world have put enormous effort into being able to connect their novel findings with what had been previously known in classical physics. One of the more relevant questions that was investigated during the mid-20th century was the relationship between the phase space formulation of classical mechanics and the analog formalism for quantum mechanics.

Due to the Heisenberg uncertainty principle, it is impossible to define a joint probability distribution for position and momentum in quantum mechanics, as one cannot simultaneously measure both variables with arbitrary precision. The non-trivial answer to this problem lies in the fact that while a true probability distribution cannot be defined in quantum mechanics, it is possible to define *quasiprobability distributions* that can capture the essential features of quantum states in a phase space representation.

From this, several representations arose, most notably the **Glauber-Sudarshan (P distribution)**, the **Husimi (Q distribution)** and **Wigner distribution**, each with their own advantages and characteristics, which depended heavily on the context in which they were used (Cahill and Glauber (1969), Moya-Cessa and Knight (1993)).

These distributions provide a complete and intuitive description of quantum states in phase space. Formally, for a quantum state $\hat{\rho}$ they can be derived from density matrix elements in the coherent state basis $\langle\alpha|\,\rho\,|\beta\rangle$. Although generally complex-valued, they encode the full information of the quantum state and are mapped to real-valued phase-space representations through invertible linear transformations.

4.2.0.1 P distribution Kernel

Also known as Glauber-Sudarshan P representation. If the quantum system has a classical analog (such as a coherent state or thermal state), then the P distribution will be non-negative. However, for exclusively quantum states with no classical analogs such as a Fock state, Schrödinger cat state, or any system that exhibits non-classical correlations (Sudarshan (1963)), the P distribution will show negativity. It can be represented in integral form as:

$$P(\alpha) = \frac{e^{|\alpha|^2}}{\pi^2} \int \langle -\beta|\,\hat{\rho}\,|\beta\rangle \, \exp(|\beta|^2 - \beta\alpha^* + \beta^*\alpha) d^2\beta \tag{4.2.1}$$

4.2.0.2 Husimi distribution Kernel

The Husimi representation is one of the easiest to calculate given that the observables are written in an anti-normal order. It is generally described in the coherent basis as

$$Q(\alpha) = \frac{1}{\pi} \langle\alpha|\,\hat{\rho}\,|\alpha\rangle\,, \tag{4.2.2}$$

meanwhile, its integral form is interpretable as the weierstass transform of the Wigner function, in an integral expression

$$Q(\alpha) = \frac{2}{\pi} \int W(\beta) \exp(-2|\alpha - \beta|^2) d^2\beta. \tag{4.2.3}$$

One of the few drawbacks of this function corresponds to the fact that the Q distribution is always non-negative, and thus, might not capture the full non-

classicality of quantum states.

4.2.0.3 The Wigner Function

The Wigner function (WF) originated as a solution for the problem of finding a quantum equivalent to the classical distribution function in phase space. It has been a tool of relevance in quantum information because it displays the state of a quantum system in a phase space, allowing for a more intuitive understanding of the quantum state. It has a unique characteristic which makes it an excellent diagnostic of quantum properties: the function can be negative in some areas of phase space, which indicates the nonclassical interferences associated to entanglement. The integral form of the WF is

$$W(\alpha) = \frac{1}{\pi^2} \int \mathrm{Tr}\{\hat{D}(\beta)\hat{\rho}\}\, e^{\alpha\beta^* - \alpha^*\beta} d^2\beta. \tag{4.2.4}$$

Where $\hat{D}(\beta)$ is the displacement operator and ρ is the density matrix of the field under investigation.

The position-basis kernel for a pure state of the Wigner function is $\langle q + x/2| \, \rho \, |q - x/2\rangle$. The process of going from kernel representation to quasiprobability distribution generally involves a Fourier transform, and we can define the Wigner function in a position of the phase space α by writing (Banaszek and Wódkiewicz (1996)),

$$W(\alpha) = \frac{2}{\pi} \mathrm{Tr}\left[\hat{\rho}\hat{D}^\dagger(\alpha) e^{i\pi\hat{a}^\dagger\hat{a}} \hat{D}(\alpha)\right]. \tag{4.2.5}$$

Being able to directly measure the WF yields complete knowledge of the quantum state and enables a clearer physical interpretation of the quasiprobability distribution. Additionally, the phase-space representation offered by the Wigner function (and other representations as well) allows for a direct visualization of the quantum state, facilitating insight into its geometrical structure in the phase space. It's negativity also serves as an indicator of nonclassical behavior (Kenfack and yczkowski (2004)).

While these distributions provide a powerful theoretical framework, researchers quickly realized that much alike the quantum state, the quasiprobability distributions cannot be measured directly in a single experimental shot (Leonhardt

and Paul (1995)). Instead, their experimental determination relies on the *statistical reconstruction* of the quantum state from a series of measurements, a process known as quantum tomography.

4.3 Quantum State Tomography

Quantum state tomography (QST) is the process of reconstructing the quantum state of a system through a set of measurements applied on an ensemble of identical quantum states. One expects that this ensemble is tomographically complete, meaning that the measured operators must form a basis on the Hilbert space of the system, allowing us to retrieve all the information about the state (Lvovsky and Raymer (2009a)). QST is a very useful tool in quantum information, as it allows us to not only characterize quantum states, but by virtue verifies state preparation, examines state properties such as correlations, and helps us calibrate experimental systems. However, the data obtained from these measurements do not yield the state directly (predictably), but rather indirectly through data analysis; a process we usually call reconstruction (See Fig. 4.3.1). Huge efforts are currently being devoted to research algorithms that will make this process easier (Zuo et al. (2022)).

Experimental measurements of the Wigner function (WF) in cavity QED systems were first proposed by Lutterbach and Davidovich (1997) and then succesfully realized (Nogues et al. (2000); Bertet et al. (2002)), standing as a testament to the sophisticated control achieved in these pioneering experiments. However, it becomes easy to see how many complexity layers are added in for CQED systems to be realized. Not only are these realizations resource intensive and high complexity tasks in the experiment, but algorithmic reconstruction methods, such as the inverse Radon transform, or maximum likelihood algorithms, scale fast with the size of the Hilbert space, making them impractical if not impossible for larger systems (Suess et al. (2017); Mele et al. (2025)).

A less common tomography technique arises from exploiting beam splitter interactions which allowed for the direct measurement of quasi-probability functions via photon counting (Banaszek et al. (1999); Wallentowitz and Vogel (1996)); something that had been experimentally out of reach until very recently (Laiho et al. (2009) Nehra et al. (2019)). In that direction, we propose a novel

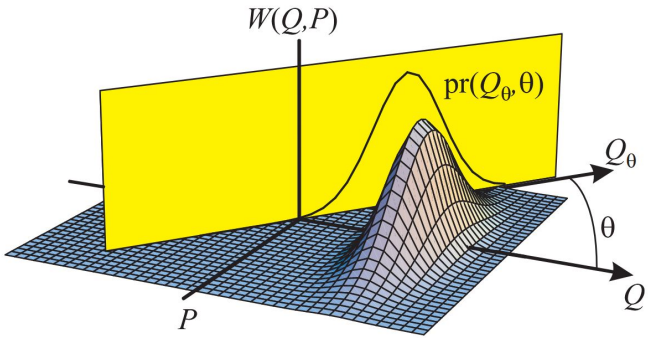

Figure 4.3.1: Measurement of the Wigner function via optical tomography. The yellow plane at an angle θ represents the phase of the local oscillator; the projection of the Wigner function on this plane shows the measured field quadrature probability density $pr(Q_\theta, \theta)$. In order to reconstruct the full Wigner function, it would require a sufficiently dense set of local oscillator phases. Figure from Lvovsky and Raymer (2009a)

method based on the QMs to perform quantum state tomography in a manner adjacent to the former proposal. In the following sections, we will derive how the interactions with the QM will allow for the natural developing of the parity operator, which can be engineered to form the quasiprobability functions we seek in different contexts.

4.4 Quantum Beam Splitter Formalism

The present section presents a step-by-step logical progression, starting from the derivation of a symmetric beam-splitter-like device, through the measurement protocol for the WF, and concluding with a discussion on the experimental feasibility of this protocol.

4.4.1 General Description

A beam splitter is a device that allows for passive transmission and reflection of light. Light entering through any port might change its path or not with a certain probability characterized by the complex coefficients of reflection r and transmission t. Without defining any particular characteristic of this device, a

loss-less beam splitter can be described through a unitary operator

$$\hat{U}_{BS} = \begin{pmatrix} t_0 & r_0 \\ r_1 & t_1 \end{pmatrix}, \tag{4.4.1}$$

where we can write the input and output modes following the relation

$$\begin{pmatrix} b_0 \\ b_1 \end{pmatrix} = \begin{pmatrix} t_0 & r_0 \\ r_1 & t_1 \end{pmatrix} \begin{pmatrix} a_0 \\ a_1 \end{pmatrix}, \tag{4.4.2}$$

or equivalently

$$b_0 = t_0 a_0 + r_0 a_1, \tag{4.4.3}$$
$$b_1 = r_1 a_0 + t_1 a_1. \tag{4.4.4}$$

The input a_k and output b_k bosonic modes obey the conmutation relations

$$\left[a_i, a_j^\dagger\right] = \delta_{ij}, \tag{4.4.5}$$
$$\left[b_i, b_j^\dagger\right] = \delta_{ij}, \tag{4.4.6}$$

respectively. Applying the commutation relations to the output modes, we obtain

$$|t_0|^2 + |r_0|^2 = 1 \tag{4.4.7}$$
$$|t_1|^2 + |r_1|^2 = 1 \tag{4.4.8}$$
$$t_0 r_1^* + r_0 t_1^* = 0. \tag{4.4.9}$$

From Eq. (4.4.9) we can obtain the phase dependence of the coefficients. Through a polar decomposition, one can write $t_i = |t_i| e^{i\phi_{t_i}}$ and $r_i = |r_i| e^{i\phi_{r_i}}$, allowing us to obtain

$$|t_0| e^{i\phi_{t_0}} |r_1| e^{-i\phi_{r_1}} + |r_0| e^{i\phi_{r_0}} |t_1| e^{-i\phi_{t_1}} = 0. \tag{4.4.10}$$

This equation must be satisfied in both the real and imaginary parts, which leads to the conditions

$$|t_0||r_1| = |r_0||t_1| \tag{4.4.11}$$

and

$$e^{i(\phi_{t_0} - \phi_{r_1})} = e^{i(\phi_{r_0} - \phi_{t_1})}. \tag{4.4.12}$$

Equation (4.4.12) can be satisfied if $\phi_{t_0} - \phi_{r_1} = \phi_{r_0} - \phi_{t_1} \pm \pi$. From the modulus condition we obtain the relation between the transmittance and reflectance coefficients. Starting from

$$|t_0||r_1| = |r_0||t_1| \tag{4.4.13}$$
$$|t_0|^2|r_1|^2 = |r_0|^2|t_1|^2 \tag{4.4.14}$$
$$|t_0|^2(1 - |t_1|^2) = (1 - |t_0|^2)|t_1|^2 \tag{4.4.15}$$
$$|t_0|^2 - |t_0|^2|t_1|^2 = |t_1|^2 - |t_0|^2|t_1|^2 \tag{4.4.16}$$
$$|t_0|^2 = |t_1|^2 \tag{4.4.17}$$
$$|t_0| = |t_1| = t \tag{4.4.18}$$
$$|r_0| = |r_1| = r, \tag{4.4.19}$$

thus, we can parameterize the equations by setting $\theta = arctan(r/t)$ with $\theta \in [0, \pi/2]$ as the angle that **defines the transmittance and reflectance of the beam splitter**. Then if $|r|^2 + |t|^2 = 1$

$$t = \cos(\theta), \quad r = \sin(\theta). \tag{4.4.20}$$

Finally, we can rewrite the original matrix as the components we have found,

$$U_{BS} = \begin{pmatrix} \cos(\theta)e^{i\phi_{t_0}} & \sin(\theta)e^{i\phi_{r_0}} \\ -\sin(\theta)e^{-i\phi_{r_1}} & \cos(\theta)e^{-i\phi_{t_1}} \end{pmatrix}, \tag{4.4.21}$$

Factoring out the phases and renaming them: $\phi_0 = (\phi_{t_0} + \phi_{t_1})/2$, $\phi_t = (\phi_{t_0} - \phi_{t_1})/2$ and $\phi_r = (\phi_{r_0} - \phi_{r_1} \mp \pi)/2$ the final expression for the beam splitter matrix is

$$U_{BS} = e^{i\phi_0} \begin{pmatrix} \cos(\theta)e^{i\phi_t} & \sin(\theta)e^{i\phi_r} \\ -\sin(\theta)e^{-i\phi_r} & \cos(\theta)e^{-i\phi_t} \end{pmatrix}. \tag{4.4.22}$$

Note that the determinant of U_{BS} is

$$|U_{BS}| = e^{2i\phi_0}. \tag{4.4.23}$$

Therefore, whether U_{BS} is in $SU(2)$ or $U(2)$ depends on the value of $2\phi_0$ or, equivalently, $\phi_{t_0} + \phi_{t_1}$.

4.4.2 Symmetric Case

In the particular case of a symmetric beam splitter, both the transmittance and the reflectance coefficients are equal to each other.

$$M = \begin{pmatrix} t & r \\ r & t \end{pmatrix}, \tag{4.4.24}$$

Again, if $t = |t|e^{i\phi_t}$ and $r = |r|e^{i\phi_r}$, using Eq. (4.4.9) one may arrive to the equation

$$|t - r|^2 = (t^* - r^*)(t - r) = |t|^2 + |r|^2 - (tr^* + rt^*) = |t|^2 + |r|^2 = 1. \tag{4.4.25}$$

This leads to the relation commonly written as $t - 1 = r$, however, this is an idealized version of the equation that **ignores the global phase**. The more general expression is as follows

$$t = r + e^{i\phi}. \tag{4.4.26}$$

The phase relation can be obtained from Eq. (4.4.9); solving for the phase components

$$\phi_r - \phi_t = \pm\pi/2. \tag{4.4.27}$$

Thus, we can **parameterize** the equations with $t = e^{i\phi} + |r|e^{i\phi_r}$. Starting from Eq. 4.4.7, one arrives to

$$|r|(\cos(\phi - \phi_r) + |r|) = 0,$$

and the solutions for this equation are simply

$$|r| = 0 \quad \text{and} \quad |r| = -\cos(\phi - \phi_r), \tag{4.4.28}$$

where $(\phi_r - \phi) \in [\pi/2, 3\pi/2]$ in order for $|r|$ to be positive. Using the non-trivial solution, one obtains the expression for t

$$t = -ie^{i\phi_r} \sin(\phi_r - \phi). \tag{4.4.29}$$

Replacing the coefficients on the original matrix, this leads to

$$M = \begin{pmatrix} -ie^{i\phi_r}\sin(\phi_r - \phi) & -e^{i\phi_r}\cos(\phi - \phi_r) \\ -e^{i\phi_r}\cos(\phi - \phi_r) & -ie^{i\phi_r}\sin(\phi_r - \phi) \end{pmatrix} \tag{4.4.30}$$

In a general case, where this matrix is not necessarily symmetric, θ defines the transmittance and reflectance of the beam splitter; meanwhile in the symmetric case, the angle that defines these coefficients is given by $(\phi_r - \phi)$, within a restriction given by our solutions that can be rewritten as

$$\phi_r - \phi = \theta + \frac{\pi}{2}, \quad \theta \in [0, \pi/2]. \tag{4.4.31}$$

We rewrite this equation in terms of θ and the *unknown* phase ϕ, giving us the final expression for the symmetric beam splitter matrix

$$M = e^{i(\phi+\theta)} \begin{pmatrix} \cos(\theta) & i\sin(\theta) \\ i\sin(\theta) & \cos(\theta) \end{pmatrix}. \tag{4.4.32}$$

One might also directly use Eq. 4.4.22, from the general description, set $\phi_0 = \phi + \theta$, $\phi_t = 0$ and $\phi_r = \pi/2$, and recover this same expression, confirming that this is indeed a particular case of the general beam splitter matrix.

4.5 Angular Momentum Analog

An additional understanding of the beam splitter operation can be obtained through an analogy with angular momentum manifested through the Schwinger representation Campos et al. (1989). Using the previous definitions, of $\hat{a}_0$ and $\hat{a}_1$ the two input modes of the beam splitter, and $\hat{b}_0$, $\hat{b}_1$ as the two output modes, we can switch the focus from the number of photons to the angular momentum $\hat{L}$. We then define the angular momentum operators (Makarov (2022), Yurke et al. (1986)):

$$\hat{L}_1 = \frac{1}{2}\left(\hat{a}_0^\dagger \hat{a}_1 + \hat{a}_1^\dagger \hat{a}_0\right), \quad \hat{L}_2 = \frac{1}{2i}\left(\hat{a}_0^\dagger \hat{a}_1 - \hat{a}_1^\dagger \hat{a}_0\right), \quad \hat{L}_3 = \frac{1}{2}\left(\hat{a}_0^\dagger \hat{a}_0 - \hat{a}_1^\dagger \hat{a}_1\right). \tag{4.5.1}$$

One can verify these operators satisfy the angular momentum commutation relations. The square of the angular momentum is related to the boson number

operators

$$\hat{L}^2 = \sum_{i=1}^{3} \hat{L}_i^2 = \hat{l}(\hat{l}+1), \quad \hat{L}_3 = \hat{m}, \tag{4.5.2}$$

$$\hat{l} = \frac{1}{2}(\hat{n}_0 + \hat{n}_1), \quad \hat{m} = \frac{1}{2}(\hat{n}_0 - \hat{n}_1), \tag{4.5.3}$$

where $\hat{n}_0$, $\hat{n}_1$ are operators of the number of photons in modes 0 and 1 respectively. Eqs. 4.5.1-4.5.3 apply analogously for the output modes $\hat{b}_0$, $\hat{b}_1$. The transformation between the input and output modes can be expressed through an operator $\hat{B}$

$$\hat{L}'_j = \hat{B}(\Phi, \Theta, \Psi)\hat{L}_j\hat{B}^\dagger(\Theta, \Phi, \Psi), \quad j = 0, 1. \tag{4.5.4}$$

$\hat{L}'_j$ are the output angular momentum operators, while $\hat{L}_j$ are the input angular momentum operators. This is a standard representation of the rotation $SO(3)$; applicable provided that this same rotation can be used on the bosonic operators $\hat{a}_0$, $\hat{a}_1$ and $\hat{b}_0$, $\hat{b}_1$. The general form for this matrix is given by

$$\hat{B}(\Phi, \Theta, \Psi) = e^{-i\Phi\hat{L}_3}e^{-i\Theta\hat{L}_2}e^{-i\Psi\hat{L}_3}. \tag{4.5.5}$$

The parameters (Φ, Θ, Ψ) are comparable to the classical Euler angles. In this representation, we identify the angles Φ and Ψ as the relative phases between the modes, while Θ is related to the transmittance and reflectance of the beam splitter. Through the representation of SU(2), Eq. 4.5.5 can be rewritten as an operation of matrices

$$\hat{B} = \begin{pmatrix} e^{i\Psi/2} & 0 \\ 0 & e^{-i\Psi/2} \end{pmatrix} \begin{pmatrix} \cos(\Theta/2) & \sin(\Theta/2) \\ -\sin(\Theta/2) & \cos(\Theta/2) \end{pmatrix} \begin{pmatrix} e^{i\Phi/2} & 0 \\ 0 & e^{-i\Phi/2} \end{pmatrix}, \tag{4.5.6}$$

equivalently,

$$\hat{B} = \begin{pmatrix} \cos(\Theta/2)e^{i(\Phi+\Psi)/2} & \sin(\Theta/2)e^{i(\Phi-\Psi)/2} \\ -\sin(\Theta/2)e^{-i(\Phi-\Psi)/2} & \cos(\Theta/2)e^{-i(\Phi+\Psi)/2} \end{pmatrix}. \tag{4.5.7}$$

It is possible to identify the similarities of the beam splitter matrix U_{BS} from Eq. 4.4.22 and the rotation matrix $\hat{B}$. One might for example, restrict the solutions for a $\phi_0 = 0$. Ignoring this *global phase* restricts the transformation to the unimodular

subgroup SU(2); and allows us to obtain the relations

$$\Theta = 2\theta \ , \quad \Phi + \Psi = 2\phi_t \ , \quad \Phi - \Psi = 2\phi_r. \tag{4.5.8}$$

We note that in our particular case we will not be able to ignore the global phase, as we have seen in Section 4.4.1. In what follows, we will connect the two former sections and find an expression for both the Schrödinger and Heisenberg pictures.

4.5.1 Symmetric Case

To recover the expression derived in Eq. 4.4.32, we make use of the past section, and easily recognize how the external phases appear as global operators:

$$\hat{B}_{sym} = e^{-i(\theta+\phi)\hat{n}} e^{i\frac{\pi}{2}\hat{L}_3} e^{-i2\theta\hat{L}_2} e^{-i\frac{\pi}{2}\hat{L}_3} = e^{-i\{(\theta+\phi)\hat{n}+2i\theta\hat{L}_1\}} = e^{-i(\theta+\phi)\hat{n}}\hat{U}_M. \tag{4.5.9}$$

$\hat{n} = \hat{a}_0^\dagger\hat{a}_0 + \hat{a}_1^\dagger\hat{a}_1$ is the total photon number operator. Through the BCH formula, the phases are left operating on the outside, confirming the global component. All that is left is to apply the BCH on the $\hat{U}_M$ operator (which is what we have named the symmetric beam splitter operator, a less general version of $\hat{U}_{BS}$), solve the matrix multiplications inside the equation, and we will obtain the final expression for the symmetric beam splitter that we derived before, confirming the consistency of both approaches

$$\begin{pmatrix} \hat{a}_0' \\ \hat{a}_1' \end{pmatrix} = e^{i(\phi+\theta)} \begin{pmatrix} \cos\theta & i\sin\theta \\ i\sin\theta & \cos\theta \end{pmatrix} \begin{pmatrix} \hat{a}_0 \\ \hat{a}_1 \end{pmatrix}. \tag{4.5.10}$$

4.5.1.1 Two particular cases

We notice that for the particular case of $\theta = 0$, the beam splitter will behave as a phase shifter, since all the incoming light will be transmitted. For two incident arbitrary fields (see for example Fig. 4.6.1), we observe that no photon number parity operators will appear after the interaction.

$$\hat{U}_M^{\theta=0} \left|\varphi\right\rangle_0 \left|\psi\right\rangle_1 = e^{-i\phi\hat{n}_0} \left|\varphi\right\rangle_0 e^{-i\phi\hat{n}_1} \left|\psi\right\rangle_1 . \tag{4.5.11}$$

Meanwhile, for the case of a 50/50 beam splitter, where $\theta = \pi/2$, the relations

between the input and output modes will be

$$\hat{U}_M^{\theta=\pi/2} |\varphi\rangle_0 |\psi\rangle_1 = e^{-i\phi\hat{n}_0} \hat{P}_0 |\psi\rangle_0 e^{-i\phi\hat{n}_1} \hat{P}_1 |\varphi\rangle_1 \tag{4.5.12}$$

These two expressions hint at the connection between being able to control the transmittance and reflectance of the beam splitter, and the appearance of parity operators ($\hat{P}_k = e^{i\pi\hat{n}_k}$ for $k = 0, 1$) in the output modes. This is a key feature of the Quantum Mirror, which we will explore in the next section.

4.6 Quantum Mirror

With the relationship between the quantum mirror and the angular momentum understood, we can now introduce the actual mechanism that we will use as the tomography technology. The overall action on an arbitrary electromagnetic input state depends on the internal state of the Quantum Mirror (QM), due to its controllable nature. If the QM is in the ground state $|g\rangle$, the input states will not change and will transmit as if there were no medium. If the QM is in the excited state $|e\rangle$, the input states will be reflected and acquire a phase following Eq. 4.5.12. This is best described through a unitary operator that transforms the input modes into output modes, given by:

$$\hat{U}_{QM} = \hat{\pi}_g \otimes \mathbf{1}_0 \otimes \mathbf{1}_1 + \hat{\pi}_e \otimes \hat{U}_M, \tag{4.6.1}$$

where $\hat{\pi}_g = |g\rangle\langle g|$ and $\hat{\pi}_e = |e\rangle\langle e|$ correspond to the projectors of the state of the atomic system or mirror. $\mathbf{1}_0$ and $\mathbf{1}_1$ are the identity operators acting on the input modes 0 and 1 respectively, while $\hat{U}_M$ is the operator that describes the action of the QM on the input modes when the mirror is in the excited state $|e\rangle$.

4.6.1 Transformations between QM's

Eq. 4.5.12 suggests the possibility of being able to manipulate *where* the parity operators act, something which can be achieved through the control of the external phases. Controlling the relative phases introduced in the system is crucial, since different phase configurations lead to distinct interference outcomes that can be exploited to engineer specific quantum operations, such as controlled-SWAP gates

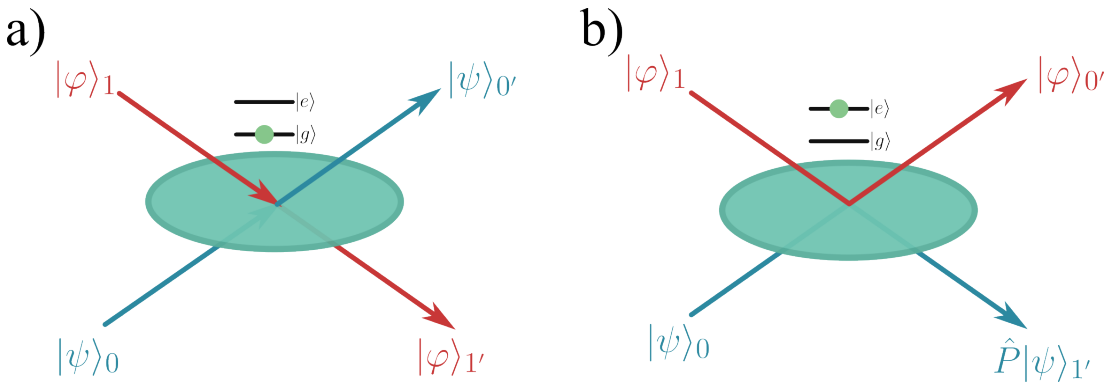

Figure 4.6.1: Schematic representation of a Quantum Mirror (QM). The QM can be in two states: ground state $|g\rangle$ or excited state $|e\rangle$. a) When in the ground state, the input modes $|\psi\rangle_0$ and $|\phi\rangle_1$ pass through unchanged to the output modes $|\psi\rangle_{0'}$ and $|\phi\rangle_{1'}$. b) When in the excited state, the input modes are reflected, swapping their paths and acquiring a phase factor dependent on the photon number in mode 1.

or to reveal symmetry-breaking effects.

We can see from Eq. 4.5.12 and Eq. 4.6.1 that the phase imparted by the beam splitter is no longer global but instead becomes a relative phase between the control subspaces ($\{|e\rangle, |g\rangle\}$). This intrinsically symmetric phase response can be manipulated further to be asymmetric by introducing external path-dependent phase shifts $\{\varphi_0, \varphi_1, \varphi_2, \varphi_3\}$, implemented as $e^{i(\varphi_0\hat{n}_0+\varphi_1\hat{n}_1)}$ before the QM and $e^{-i(\varphi_2\hat{n}_0+\varphi_3\hat{n}_1)}$ after it (Fig. 4.6.2). Reordering the terms, the resulting system operator can be written as

$$\begin{aligned}\hat{U}_S &= e^{-i(\varphi_2\hat{n}_0+\varphi_3\hat{n}_1)}\,\hat{U}_{QM}\,e^{i(\varphi_0\hat{n}_0+\varphi_1\hat{n}_1)},\\ &= \hat{\pi}_g \otimes e^{i(\varphi_{in}-\varphi_{out})\hat{n}/2}e^{i(\Delta-\Delta')\hat{L}_3} + \hat{\pi}_e \otimes e^{i(\varphi_{in}-\varphi_{out})\hat{n}/2}e^{-i\Delta'\hat{L}_3}\hat{U}_M\,e^{i\Delta\hat{L}_3},\end{aligned} \tag{4.6.2}$$

where we have introduced the phase sums and differences $\varphi_{in} = \varphi_0 + \varphi_1$, $\varphi_{out} = \varphi_2 + \varphi_3$, $\Delta = \varphi_0 - \varphi_1$ and $\Delta' = \varphi_2 - \varphi_3$. Factoring out common terms, we can rewrite the expression as

$$\hat{U}_S = \mathbf{1} \otimes e^{i(\varphi_{in}-\varphi_{out})\hat{n}/2}e^{i(\Delta-\Delta')\hat{L}_3}\left(\hat{\pi}_g \otimes \mathbf{1} \otimes \mathbf{1} + \hat{\pi}_e \otimes e^{-i\Delta\hat{L}_3}\,\hat{U}_M\,e^{i\Delta\hat{L}_3}\right). \tag{4.6.3}$$

Without loss of generality, we set $\varphi_0 = \varphi_2$ and $\varphi_1 = \varphi_3$, since the factorized term corresponds to a global operation on the field modes and has no physical consequence when only the atomic subsystem is measured. Then the simplified

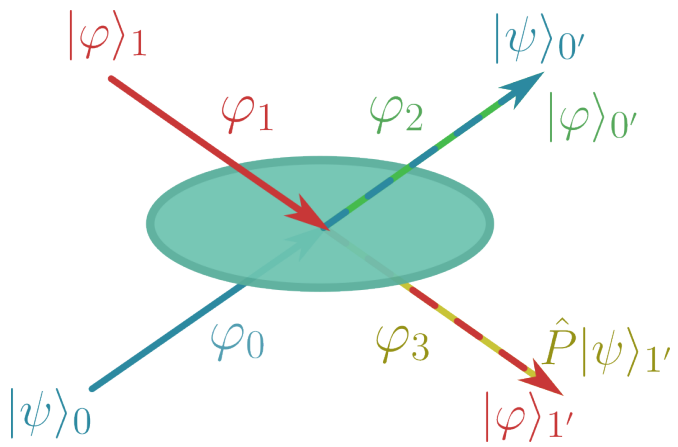

Figure 4.6.2: Schematic representation of a Quantum Mirror (QM). The induced phase shift is controllable and described by φ_i with $i = 0, 1, 2, 3$. The operation of the QM depends on the state of the atomic system, as discussed in the main text. When the atomic system is in the excited state $|e\rangle$, the QM swaps the input modes while simultaneously applying a parity operation to each mode. These parity transformations are governed by the induced phase shifts φ_i.

unitary system operator is given by

$$\hat{U}_S = \hat{\pi}_g \otimes \mathbf{1} \otimes \mathbf{1} + \hat{\pi}_e \otimes e^{-i\Delta\hat{L}_3}\, \hat{U}_M\, e^{i\Delta\hat{L}_3}. \tag{4.6.4}$$

Finally, the action of $\hat{U}_S$ on two incoming field modes prepared in arbitrary states $|\psi\rangle$ and $|\varphi\rangle$ and on the atomic state is given by

$$\begin{aligned} \hat{U}_S\,|g\rangle\,|\psi\rangle\,|\varphi\rangle &= |g\rangle\,|\psi\rangle\,|\varphi\rangle \\ \hat{U}_S\,|e\rangle\,|\psi\rangle\,|\varphi\rangle &= |e\rangle e^{-i(\phi+\Delta)\hat{n}_0}\hat{P}_0\,|\varphi\rangle \otimes e^{-i(\phi-\Delta)\hat{n}_1}\hat{P}_1\,|\psi\rangle\,. \end{aligned} \tag{4.6.5}$$

This effectively breaks the symmetry of the parity operators acting on the input states, allowing us to choose which mode will receive the parity operation based on the phase difference Δ and the relative global phase ϕ. We note, that the before called *global* phase can no longer be factorized, which selects a preferred path dependent on the photon number.

4.6.2 QM for State Tomography

Before proceeding, we fix the phase parameters that will be assumed throughout the remainder of this section and the following analysis. In particular, we consider

the symmetric operating point of the QM, setting the internal phase to $\phi = \pi/2$ and the external phase difference to $\Delta = \pi/2$. As shown in Eq. 4.6.5, this choice leads to a controlled and asymmetric action of the parity operator on the input modes. These parameter values will be implicitly assumed in what follows, as they are precisely the conditions under which the QM implements the measurements required for quantum state tomography.

The action of the mirror operator over input states, given by our previous assumptions and for the following of this work will be described by $\hat{U}_S(\phi, \Delta) \to \hat{U}_S(\pi/2, \pi/2) = \hat{U}'_S$:

$$\hat{U}'_S \left|g\right\rangle_a \left|\psi\right\rangle_0 \left|\phi\right\rangle_1 = \left|g\right\rangle_a \left|\psi\right\rangle_{0'} \left|\phi\right\rangle_{1'}, \tag{4.6.6}$$

$$\hat{U}'_S \left|e\right\rangle_a \left|\psi\right\rangle_0 \left|\phi\right\rangle_1 = \left|e\right\rangle_a \left|\phi\right\rangle_{0'} \hat{P}_1 \left|\psi\right\rangle_{1'}. \tag{4.6.7}$$

Furthermore, this evolution operator for the QM can also be written as $\hat{U}'_S = e^{i\theta\hat{\pi}_e \otimes \hat{L}_2}$ (See Appendix A.2.1 for further discussion and derivation).

4.6.2.1 One Interaction

We now introduce a method to quantify the information of an unknown state ρ. We first displace ρ by an adjustable amount α ($\hat{\rho}' = \hat{D}(\alpha)\hat{\rho}\hat{D}^\dagger(\alpha)$), and inject it into a QM prepared in a superposition ($\left|+\right\rangle = \left|g\right\rangle + \left|e\right\rangle$). On the other input, we inject a pure coherent state $\left|\phi\right\rangle$ (See Fig. 4.6.1). The initial state is represented by the following density matrix:

$$\begin{aligned}\hat{\rho}^{(i)}_{sys} &= \left|+\right\rangle\left\langle+\right| \otimes \rho' \otimes \left|\phi\right\rangle\left\langle\phi\right| \\ &= \left(\frac{\hat{\pi}_g + \hat{\pi}_{ge} + \hat{\pi}_{eg} + \hat{\pi}_e}{2}\right) \otimes \left(\sum_i p_i \left|\psi'_i\right\rangle\left\langle\psi'_i\right|\right) \otimes \left|\phi\right\rangle\left\langle\phi\right|\end{aligned} \tag{4.6.8}$$

The resulting state after the interaction is given by the operation $\hat{U}_S\,\hat{\rho}\,U_S^\dagger = \hat{\rho}^{(f)}_{sys}$ will be then

$$\hat{\rho}^{(f)}_{sys} = \frac{1}{4}\left(\pi_g\rho_{sys} + \pi_{ge}\rho_{sys}\hat{U}_S^\dagger + \hat{U}_S\pi_{eg}\rho_{sys} + \hat{U}_S\pi_{ee}\rho_{sys}\hat{U}_S^\dagger\right). \tag{4.6.9}$$

We measure the system in a convenient basis of the superposition of excited and ground atomic states, $\left|\xi_\pm\right\rangle = \left|g\right\rangle \pm e^{i\delta}\left|e\right\rangle$. This means we will trace out the system

as $Tr(\rho_{sys} |\xi_\pm\rangle \langle\xi_\pm|)$, which leads to a probability that depends on the parameter δ. This equation has the foundational shape of the quasiprobability distributions mentioned early in this chapter. Physically, it would correspond to the projection of the information of the quantum state of light onto the Bloch sphere of the ancilla atom.

$$p_\pm(\delta) = \frac{1}{2}\left(1 \pm \mathrm{Re}[e^{-i\delta} \langle\phi| e^{i\pi\hat{n}} \hat{D}^\dagger(\alpha)\hat{\rho}\hat{D}(\alpha) |\phi\rangle]\right) \tag{4.6.10}$$

Here, $\hat{D}(\alpha)$ is the displacement operator that shifts the unknown state $\hat{\rho}$ in phase space by an amount α. This variable then, can be controlled as to *scan* the phase space. The operator $e^{i\pi\hat{n}}$ is the photon number parity operator $\hat{P}$. δ picks the angle of projection on the Bloch sphere of the atom. This is a phase that can be adjusted independently, allowing us to select different quadratures of the field. By varying δ, we can extract different components of the quasiprobability distribution, something we will derive in the next section.

4.6.2.2 Controlled Phase Interaction

Before further discussion on the utility of the QM for tomography, we will further prove the validity of the previous result by generalizing it to the case where we have external phases in the system.

Quitting the assumption that the system is naturally acting with a photon number parity operator on only one side of the QM (that is, the variables ϕ and Δ that we had fixed are no longer a set value), we can generalize the previous result to any global phase or even external phases induced in the system.

Starting from the definition of the QM operator given by Eq. 4.5.12, we will now add controllable phases before and after the interaction, namely φ_0 , φ_1 for the input modes and φ_2 , φ_3 for the output modes (See Fig. 4.6.2). We assume these phases can be controlled independently, allowing us to manipulate the interference effects in the system. Analogous to the previous section, we can now write the resulting state after the interaction, without making any assumptions about the

phases in the system as

$$\begin{aligned}
&\hat{U}_{QM}\,\hat{\rho}\,U_{QM}^{\dagger} \cong \pi_{gg} \otimes U_{\varphi_0-\varphi_2}\hat{\rho}' U_{\varphi_0-\varphi_2}^{\dagger} \otimes U_{\varphi_1-\varphi_3}\,|\varphi\rangle\langle\varphi|\,U_{\varphi_1-\varphi_3}^{\dagger} + \\
&\pi_{ge} \otimes U_{\varphi_0-\varphi_2} \sum_i p_i'\,|\psi_i'\rangle\langle\varphi|\,U_{\pi+\varphi_1-\varphi_2-\phi}^{\dagger} \otimes U_{\varphi_1-\varphi_3}\,|\varphi\rangle\langle\psi_i'|\,U_{\pi+\varphi_0-\varphi_3-\phi}^{\dagger} + \\
&\pi_{eg} \otimes \sum_i p_i'\,U_{\pi+\varphi_1-\varphi_2-\phi}\,|\varphi\rangle\langle\psi_i'|\,U_{\varphi_0-\varphi_2}^{\dagger} \otimes U_{\pi+\varphi_0-\varphi_3-\phi}\,|\psi_i'\rangle\langle\varphi|\,U_{\varphi_1-\varphi_3}^{\dagger} + \\
&\pi_{ee} \otimes U_{\pi+\varphi_1-\varphi_2-\phi}\,|\varphi\rangle\langle\varphi|\,U_{\pi+\varphi_1-\varphi_2-\phi}^{\dagger} \otimes U_{\pi+\varphi_0-\varphi_3-\phi}\hat{\rho}' U_{\pi+\varphi_0-\varphi_3-\phi}^{\dagger}
\end{aligned} \tag{4.6.11}$$

And calculating the trace analogously to the previous section (See Appendix A.2.2 for the details), we find the probability of measuring the atom in the state $|\xi_{\pm}\rangle$ after the interaction to be

$$p_{\pm}(\delta) = \frac{1}{2}\left(1 \pm \mathrm{Re}\left[e^{i\delta}\,\langle\varphi|\,e^{-i(\pi-\phi-\Delta)n}\hat{D}(\alpha)\hat{\rho}\hat{D}^{\dagger}(\alpha)e^{-i(\pi-\phi+\Delta)n}\,|\varphi\rangle\right]\right) \tag{4.6.12}$$

This then recovers the effect seen in Eq. 4.6.5, where one manages to "choose" in which mode the parity operator will act.

4.7 Quasiprobability Function Measurements

4.7.0.1 P distribution

To be able to measure the P distribution matrix element from a measurement in the atomic state, one can consider introducing a pure coherent state as a LO $|\varphi\rangle = |\gamma\rangle$ and set the displacement coefficient $\alpha = 0$, Using Eq. 4.6.10:

$$p_{\pm}(\delta) = \frac{1}{2}\left(1 \pm \mathrm{Re}[e^{-i\delta}\,\langle\gamma|\,e^{i\pi\hat{n}}\hat{D}^{\dagger}(0)\rho\hat{D}(0)\,|\gamma\rangle]\right)$$

Considering p_+, the parity operator will act on the coherent state as follows,

$$p_{+}(\delta) = \frac{1}{2}\left(1 + \mathrm{Re}[e^{-i\delta}\,\langle-\gamma|\,\rho\,|\gamma\rangle]\right) \tag{4.7.1}$$

For $\delta \in \{0, \pi/2\}$, the value of the matrix element can be obtained

$$2p_{+}(\delta) - 1 = \langle-\gamma|\,\rho\,|\gamma\rangle\,. \tag{4.7.2}$$

4.7.0.2 Husimi distribution

For the Husimi representation, the LO is now a vacuum state $|\varphi\rangle = |0\rangle$, the displacement $\alpha = \gamma$,

$$p_{\pm}(\delta) = \frac{1}{2}\left(1 \pm \mathrm{Re}[e^{-i\delta}\langle 0|\, e^{i\pi\hat{n}}\hat{D}^{\dagger}(\gamma)\hat{\rho}\hat{D}(\gamma)\,|0\rangle]\right)$$

4.7.0.3 Wigner distribution

The LO is now a state $|\varphi\rangle = |-x/2\rangle$, the displacement $\alpha = q$ with $q,\, x \in \mathbb{R}$

$$p_{\pm}(\delta) = \frac{1}{2}\left(1 \pm \mathrm{Re}[e^{-i\delta}\langle -x/2|\, e^{i\pi\hat{n}}\hat{D}^{\dagger}(q)\hat{\rho}\hat{D}(q)\,|-x/2\rangle]\right)$$

$$p_{\pm}(\delta) = \frac{1}{2}\left(1 \pm \mathrm{Re}[e^{-i\delta}\langle q + x/2|\,\hat{\rho}\,|q - x/2\rangle]\right)$$

4.7.0.4 Direct measurement of Wigner function through Two QM

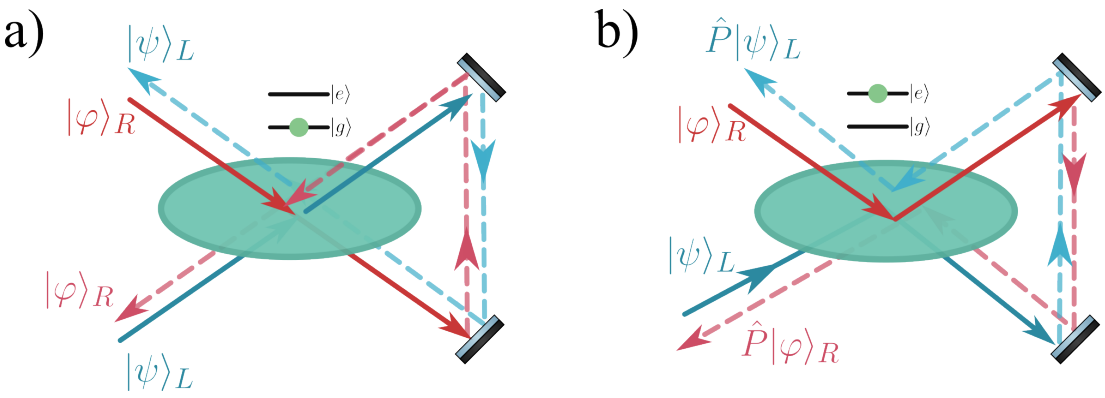

Figure 4.7.1: Schematic representation of a double-interaction with a Quantum Mirror (QM).

In the case where we have two interactions with a QM (can be the same or a second QM in the path), we could engineer the direct measurement of the Wigner function of an unknown displaced state $\hat{\rho}'$ with a vacuum state $|\varphi\rangle = |0\rangle$. The first interaction can be written immediately from Section 4.6.2.1.

$$\begin{aligned}\rho^{i}_{sys} = \frac{1}{4}(\pi_{gg}\otimes\hat{\rho}'\otimes|0\rangle\langle 0| + \pi_{ge}\otimes\sum_i p_i\,|\psi_i'\rangle\langle 0|\otimes|0\rangle\langle\psi_i'|\,\hat{P}^{\dagger} + \\ \pi_{eg}\otimes\sum_i p_i\,|0\rangle\langle\psi_i'|\otimes\hat{P}\,|\psi_i'\rangle\langle 0| + \pi_{ee}\otimes|0\rangle\langle 0|\otimes\hat{P}\hat{\rho}'\hat{P}^{\dagger}),\end{aligned} \tag{4.7.3}$$

and the second interaction with the QM will be as follows:

$$\begin{aligned}\rho_{sys}^{ii} &= \frac{1}{4}(\pi_{gg}\otimes\hat{\rho}'\otimes|0\rangle\langle 0| + \pi_{ge}\otimes\sum_i p_i|\psi_i'\rangle\langle\psi_i'|\hat{P}^\dagger\otimes|0\rangle\langle 0|\hat{P}^\dagger \\ &+ \pi_{eg}\otimes\sum_i p_i\hat{P}|\psi_i'\rangle\langle\psi_i'|\otimes\hat{P}|0\rangle\langle 0| + \pi_{ee}\otimes\hat{P}\hat{\rho}'\hat{P}^\dagger\otimes\hat{P}|0\rangle\langle 0|\hat{P}^\dagger), \\ &= \frac{1}{4}(\pi_{gg}\otimes\hat{\rho}'\otimes|0\rangle\langle 0| + \pi_{ge}\otimes\sum_i p_i|\psi_i'\rangle\langle\psi_i'|\hat{P}^\dagger\otimes|0\rangle\langle 0| \\ &+ \pi_{eg}\otimes\sum_i p_i\hat{P}|\psi_i'\rangle\langle\psi_i'|\otimes|0\rangle\langle 0| + \pi_{ee}\otimes\hat{P}\hat{\rho}'\hat{P}^\dagger\otimes|0\rangle\langle 0|),\end{aligned} \tag{4.7.4}$$

The trace over this system will give us:

$$\mathrm{Tr}\{\rho_{sys}^{ii}|\pm\rangle\langle\pm|\} = \frac{1}{2}\left(1 \pm \frac{1}{2}e^{i\delta}\mathrm{Tr}[\hat{\rho}'\hat{P}^\dagger] \pm \frac{1}{2}e^{-i\delta}\mathrm{Tr}[\hat{P}\hat{\rho}']\right) \tag{4.7.5}$$

In order to recover the Wigner function kernel, we recognize the last two terms can be written as $2Re(e^{-i\delta}\mathrm{Tr}[\hat{P}\hat{\rho}'])$, and once we set $\delta = 0$, we obtain

$$p_\pm = \frac{1}{2}\left(1 \pm \mathrm{Tr}[\hat{P}\hat{\rho}']\right) \tag{4.7.6}$$

Which is directly related to the Wigner function by writing $\hat{\rho}' = \hat{D}(\alpha)\hat{\rho}\hat{D}^\dagger(\alpha)$:

$$W(\alpha) = \frac{2}{\pi}\Big(p_+(\alpha) - p_-(\alpha)\Big) \tag{4.7.7}$$

4.7.0.5 Direct measurement of Wigner function through Two QM, with controlled phases

Following the procedure from Section 4.6.2.2, we now demonstrate that the external phase difference Δ implies no net effect on the measurement of the WF, validating the assumption made in the previous section. We begin by considering the experimental configuration of Fig. 4.7.1 and 4.6.2, and assume a stable retroreflection geometry in which path-induced (external) phase shifts are constant and determined by the fixed spatial configuration of the interferometer.

We use the same unknown displaced state $\hat{\rho}'$ with a vacuum state $|\varphi\rangle = |0\rangle$. The interaction is as follows $\hat{U}_{QM}^{\Delta}(\hat{U}_{QM}^{\Delta}\hat{\rho}'\hat{U}_{QM}^{\Delta\dagger})\hat{U}_{QM}^{\Delta\dagger}$:

$$\begin{aligned}\hat{\rho}_{sys}^{(ii)} = \pi_{gg} \otimes U_{\varphi_1-\varphi_3} U_{\varphi_0-\varphi_2} \hat{\rho}' U_{\varphi_0-\varphi_2}^{\dagger} U_{\varphi_1-\varphi_3}^{\dagger} \\ \otimes U_{\varphi_0-\varphi_2} U_{\varphi_1-\varphi_3} |\varphi\rangle \langle\varphi| U_{\varphi_1-\varphi_3}^{\dagger} U_{\varphi_0-\varphi_2}^{\dagger} + \\ \pi_{ge} \otimes U_{\varphi_1-\varphi_3} U_{\varphi_0-\varphi_2} \hat{\rho}' U_{2(\pi-\phi)}^{\dagger} U_{\varphi_0-\varphi_3}^{\dagger} U_{\varphi_1-\varphi_2}^{\dagger} \\ \otimes U_{\varphi_0-\varphi_2} U_{\varphi_1-\varphi_3} |\varphi\rangle \langle\varphi| U_{2(\pi-\phi)}^{\dagger} U_{\varphi_1-\varphi_2}^{\dagger} U_{\varphi_0-\varphi_3}^{\dagger} + \\ \pi_{eg} \otimes U_{\varphi_1-\varphi_2} U_{\varphi_0-\varphi_3} U_{2(\pi-\phi)} \hat{\rho}' U_{\varphi_0-\varphi_2}^{\dagger} U_{\varphi_1-\varphi_3}^{\dagger} \\ \otimes U_{\varphi_0-\varphi_3} U_{\varphi_1-\varphi_2} U_{2(\pi-\phi)} |\varphi\rangle \langle\varphi| U_{\varphi_1-\varphi_3}^{\dagger} U_{\varphi_0-\varphi_2}^{\dagger} + \\ \pi_{ee} \otimes U_{\varphi_1-\varphi_2} U_{\varphi_0-\varphi_3} U_{2(\pi-\phi)} \hat{\rho}' U_{2(\pi-\phi)}^{\dagger} U_{\varphi_0-\varphi_3}^{\dagger} U_{\varphi_1-\varphi_2}^{\dagger} \\ \otimes U_{\varphi_0-\varphi_3} U_{\varphi_1-\varphi_2} U_{2(\pi-\phi)} |\varphi\rangle \langle\varphi| U_{2(\pi-\phi)}^{\dagger} U_{\varphi_1-\varphi_2}^{\dagger} U_{\varphi_0-\varphi_3}^{\dagger}\end{aligned} \tag{4.7.8}$$

One can quickly recover Eq. 4.7.4 once the external phases are turned to 0. To apply the trace on this system and effectively measure in the $|\xi_+\rangle$ basis, much alike our past derivations; one can easily prove that the diagonal elements after operating $|\xi_+\rangle \langle\xi_+| \hat{\rho}'$, will be but the unity. This is true in the atomic base, the first mode and the second one. The only traces that will be non-unity correspond to the terms that go with $e^{\pm i\delta}$. Setting the phases once again to $\Delta = \varphi_2 - \varphi_1 = \varphi_0 - \varphi_3$ and putting all the terms together we will find the final expression for the measurement,

$$p_{\pm} = \frac{1}{2}(1 \pm e^{i\delta} Tr\left[\beta_{00}\right] Tr\left[\beta_{10}\right] \pm e^{-i\delta} Tr\left[\beta_{01}\right] Tr\left[\beta_{11}\right]), \tag{4.7.9}$$

where we have defined the following operators:

$$\begin{aligned}\beta_{00} &= \hat{\rho}' U_{\pi-\phi+\Delta}^{\dagger} U_{\pi-\phi-\Delta}^{\dagger} \\ \beta_{10} &= |\varphi\rangle \langle\varphi| U_{\pi-\phi+\Delta}^{\dagger} U_{\pi-\phi-\Delta}^{\dagger} \\ \beta_{01} &= U_{\pi-\phi+\Delta} U_{\pi-\phi-\Delta} \hat{\rho}' \\ \beta_{11} &= U_{\pi-\phi+\Delta} U_{\pi-\phi-\Delta} |\varphi\rangle \langle\varphi| .\end{aligned} \tag{4.7.10}$$

Substituting the definitions of defined β_{ij} into Eq. 4.7.9, we observe that the external phase factors Δ cancel out. Furthermore, by enforcing the vacuum state condition expressed in the beginning ($|\varphi\rangle = |0\rangle$), the expression simplifies to $\langle 0| \hat{U}_{2(\pi-\phi)} |0\rangle$, which has unitary trace.

$$p_{\pm} = \frac{1}{2}(1 \pm e^{i\delta} Tr\left[\hat{\rho}' U^{\dagger}_{2(\pi-\phi)}\right] \pm e^{-i\delta} Tr\left[U_{2(\pi-\phi)}\hat{\rho}'\right]), \tag{4.7.11}$$

We can see that if $\phi = \pi/2$, then $\hat{U}_{2(\pi-\phi)} = \hat{P}$, becoming thus, the parity operator we defined before. Ultimately, we recover the result explicitly derived in Eq. 4.7.5. This confirms that the external path phases cancel out, demonstrating that the Wigner function reconstruction is independent of the path induced phase differences, and without the need of a copy of the unknown quantum state $\hat{\rho}'$.

4.8 Experimental Considerations

In order to explore the experimental feasibility of implementing a QM for tomography, we require a physical system capable of dynamically controlling its reflection coefficient while simultaneously sustaining a quantum superposition state. These particular requirements have been recently demonstrated on the work by Srakaew et al. (2023), where they experimentally realized a tunable atomic mirror using an atomic lattice and Rydberg interactions. The coherent reflection from the atomic lattice arises from a collective resonance of the atomic array (Bekenstein et al. (2020), Shahmoon et al. (2017)), which can be switched on and off by manipulating the state of the control/ancilla atom. Different approaches might also be considered to realize a QM, and we refer the reader to the works realized by He and Zhu (2023), Hétet et al. (2011a), and Chang et al. (2007).

4.8.1 About the t and r coefficients

We previously introduced the general ansatz relating the transmission and reflection coefficients as

$$t = r + e^{i\phi}. \tag{4.8.1}$$

This relation is a valid starting point to analyze the behavior of the QM in a general sense. However, for our specific application, the phase ϕ depends on the internal state of the QM, which can be in either the ground state $|g\rangle$ or the excited state $|e\rangle$. Therefore, while we can initially consider the relation quantum mirror (without assuming anything yet about any coefficients),

$$t_k = r_k + e^{i\phi_k}, \tag{4.8.2}$$

with $k = e, g$. Considering the physical constrains of the system, we can interpret these coefficients through the lens of the *dominant process* in each state of the mirror. In the ground state $|g\rangle$, the system is designed to be highly transmissive, which implies $t_g \gg r_g$. The treatment is analogous for the excited state $|e\rangle$, where the system is predominantly reflective, leading to $r_e \gg t_e$. This leads us to consider the following approximations:

$$\begin{aligned} t_g &= e^{i\phi_g} \quad (\text{for } |g\rangle) \\ r_e &= -e^{i\phi_e} \quad (\text{for } |e\rangle). \end{aligned} \tag{4.8.3}$$

The action of these coefficients in each subspace leads to the following transformations of the field operators:

$$(\hat{a}_0, \hat{a}_1) \xrightarrow{\hat{U}_g} (\hat{a}_0 e^{i\phi_g}, \hat{a}_1 e^{i\phi_g}), \tag{4.8.4}$$

$$(\hat{a}_0, \hat{a}_1) \xrightarrow{\hat{U}_e} (-\hat{a}_1 e^{i\phi_e}, -\hat{a}_0 e^{i\phi_e}), \tag{4.8.5}$$

Finally, the action of $\hat{U}'_{QM}$ on two incoming field modes prepared in arbitrary states $|\psi\rangle$ and $|\varphi\rangle$ and on the atomic state is given by

$$\begin{aligned} \hat{U}'_{QM} |g\rangle |\psi\rangle |\varphi\rangle &= |g\rangle \hat{U}_M^{(g)} |\psi\rangle |\varphi\rangle = |g\rangle e^{-i\phi_g \hat{n}_0} |\psi\rangle e^{-i\phi_g \hat{n}_1} |\varphi\rangle \\ &= (\mathbf{1} \otimes e^{-i\phi_g \hat{n}}) |g\rangle |\psi\rangle |\varphi\rangle \end{aligned} \tag{4.8.6}$$

$$\begin{aligned} \hat{U}'_{QM} |e\rangle |\psi\rangle |\varphi\rangle &= |e\rangle \hat{U}_M^{(e)} |\psi\rangle |\varphi\rangle = |e\rangle e^{-i\phi_e \hat{n}_0} \hat{\Pi} |\varphi\rangle e^{-i\phi_e \hat{n}_1} \hat{\Pi} |\psi\rangle \\ &= (\mathbf{1} \otimes e^{-i\phi_g \hat{n}}) |e\rangle e^{-i(\phi_e - \phi_g)\hat{n}_0} \hat{\Pi} |\varphi\rangle e^{-i(\phi_e - \phi_g)\hat{n}_1} \hat{\Pi} |\psi\rangle \end{aligned} \tag{4.8.7}$$

From these two expressions, we observe that the phase ϕ_g appears only as a global phase factor and is therefore physically irrelevant. Consequently, the physically relevant phase shift appearing in Eq. 4.5.12 can be identified as the phase difference between the two internal states of the QM,

$$\phi = \phi_e - \phi_g. \tag{4.8.8}$$

4.8.2 Rydberg mediated Metasurface

To provide concrete values for the phase ϕ we need in order to be able to implement the QM for the tomography protocol, we turn to one of the possible realizations

of the switchable metasurface, the Rydberg mediated metasurface (Srakaew et al. (2023); Bekenstein et al. (2020)). This system consists of a uniform 2D lattice (with a variable lattice constant, $a_{lattice} = 532$nm for the experimental setup), presenting collective effects leading to mirror-like behavior. This optical response is mediated by a Rydberg *control* atom in the middle (See Figure 4.8.1).

As mentioned in (Srakaew et al. (2023); Srakaew (2024)), through the use of a probe laser $\lambda_p = 780$nm and a control wavelength $\lambda_p = 480$nm, the system is induced into an EIT (transparent) state. A UV laser $\lambda_{UV} = 297$nm π-pulse is applied, coupling the central ancilla atom into a rydberg state which 'turns off' the EIT previously induced. The system reverts to a two-level optical response, rendering the lattice highly reflective. In that sense, we map the two states of the QM: we associate the EIT (transparent) system to the *ground* QM state, while the coupled Rydberg control (reflective) would be the *excited* QM state.

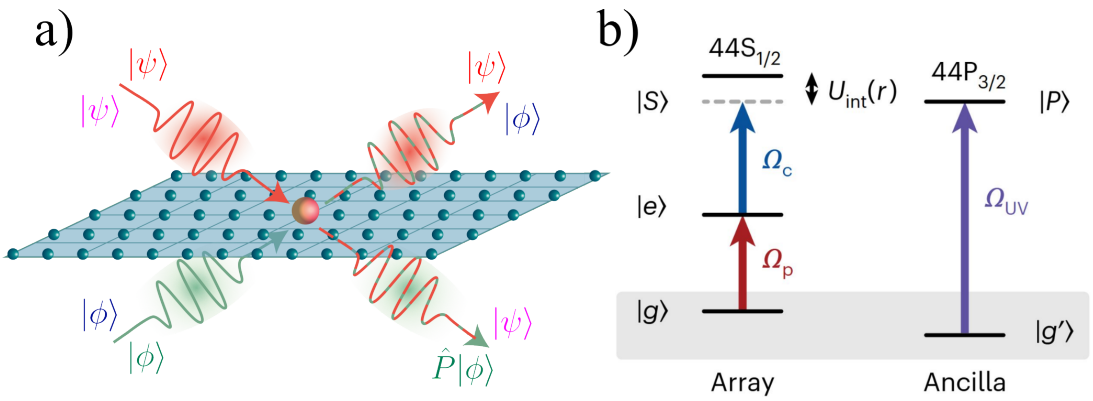

Figure 4.8.1: a) Schematic representation of a Quantum Mirror (QM) in a Rydberg mediated metasurface. b) Energy level diagram of the atomic lattice and ancilla atom used to control the reflectivity of the metasurface. The probe and control lasers create an EIT condition in the lattice atoms, while the UV laser couples the ancilla atom to a Rydberg state, disrupting the EIT and switching the metasurface to a reflective state. Adapted from Srakaew et al. (2023).

In order to calculate the phase difference ϕ between both states of the QM, we need to calculate the reflection coefficient r_e and the transmission coefficient t_g, just as discussed. These coefficients can be derived from the electric susceptibilities of the medium, which will differ depending on wether we are in the EIT regime (ground state) or the two-level regime (excited state). Following the model presented in Srakaew (2024), we can express the susceptibilities for both the EIT and two-level (TA) regimes.

The susceptibility of the EIT system (only probe and control laser on) can be written as follows,

$$\chi^{EIT} = \chi_0 \frac{i\Gamma_e}{\Gamma_e - 2i\delta_p + \Omega_c^2[\Gamma_{ryd} - 2i\Delta_2]^{-1}}, \tag{4.8.9}$$

where $\Gamma_{e,ryd}$ are the natural decay rates, $\chi_0 = 3n_a\lambda_p^2/(2\pi k_p)$ the value that contains the optical cross-section, σ_0 and the number density n_a, bridging then the macroscopic reaction of the single atom susceptibility onto the medium. k_p corresponds to the wave vector of the probe light (where the transparency occurs), $\delta_p = \omega_p - \omega_{eg}$, and $\delta_c = \omega_c - \omega_{se}$ and $\Delta_2 = \delta_p - \delta_c$ the two-photon detuning. When the EIT breaks down (the Rydberg state is induced in the control atom), the system can be seen again as a two-level system:

$$\chi^{TA} = \chi_0 \frac{i\Gamma_e}{\Gamma_e - 2i\delta_p}, \tag{4.8.10}$$

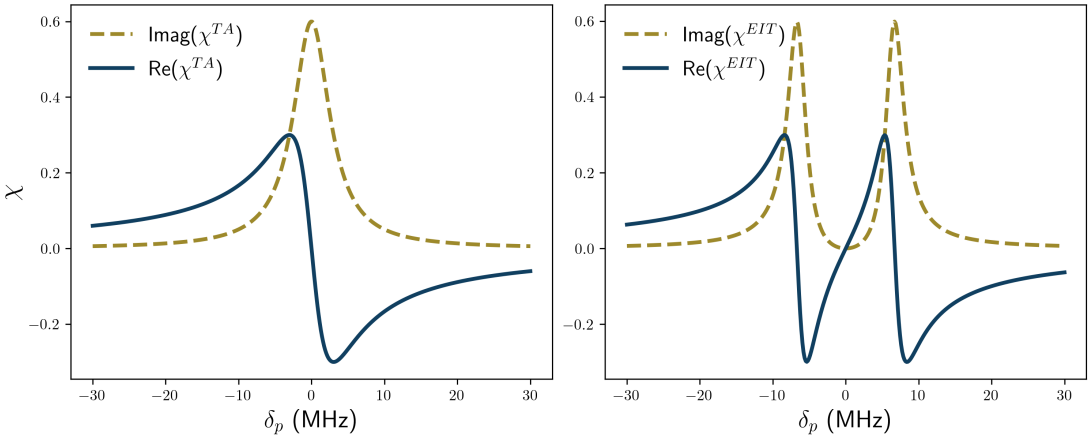

Figure 4.8.2: Real and imaginary parts of the electric susceptibility for the two-level (left) and EIT (right) regimes. The susceptibilities are calculated using the following parameters: $\Gamma_e = 2\pi \times 6$ MHz, $\Gamma_{ryd} = 2\pi \times 10$ kHz, $\Omega_c = 2\pi \times 13.4$ MHz, $a_{lattice} = 532$nm. The detunings δ_p and δ_c are swept from -30 to 30 MHz. Due to normalization, these figures are set to be a reference and do not represent the actual experimental data from Srakaew (2024).

By modeling these susceptibilities explicitly (Figure 4.8.2), we can derive the exact complex transmission and reflection coefficients (t and r) for each state ($\{|e\rangle, |g\rangle\}$), which we perform in the following section.

4.8.2.1 Phase from interaction

In attempting to calculate the ϕ phase difference, we turn to the Fresnel equations for reflection and transmission at an interface. These equations describe the optical response of a *bulk medium*, through its index of refraction $n = \sqrt{1+\chi}$ and polarizability $\mathbf{P} = \varepsilon_0 \chi \mathbf{E}$. With only these two definitions we can calculate the Fresnel reflection coefficient by

$$r = \frac{E_{out}}{E_{in}}, \tag{4.8.11}$$

then $E_{out} = e^{i\phi}|r|E_{in}$. However, this approach is not enough to describe the behaviour of a medium with a particular geometry, such as a metasurface. In order to do that, we must consider boundary conditions that take into account the discontinuities in the fields at the interface. A reasonable approach for these boundary equations was defined in Achouri et al. (2015), where the authors derive a particular case of interest for an infinitesimal sheet discontinuity in free space, employing a method known as Generalized Sheet Transition Conditions (GSTCs). By applying the boundary conditions, we can derive expressions for the transmission and reflection coefficients that account for the specific properties of the metasurface. The equations derived for the transmission and reflection coefficients of this context are as follows

$$\begin{aligned} t_x &= \frac{4 + \chi_{ee}^{xx}\chi_{mm}^{yy}k^2}{(2+ik\chi_{ee}^{xx})(2+ik\chi_{mm}^{yy})} \\ r_x &= \frac{2ik(\chi_{mm}^{yy} - \chi_{ee}^{xx})}{(2+ik\chi_{ee}^{xx})(2+ik\chi_{mm}^{yy})}. \end{aligned} \tag{4.8.12}$$

Here, χ_{ee}^{xx} and χ_{mm}^{yy} are the electric and magnetic tensor susceptibilities of the metasurface, respectively, k is the wave vector of the incident light. For a material like rubidium, we can consider $\chi_{mm} \approx 0$, due to the fact that the interactions in the optical regime are dominated by the electric dipole moment. We further simplify the problem assuming the probe polarization will align with the principal axis of the interaction, such that the rubidium metasurface will react isotropically to the incident light, (thus allowing us to treat the electric susceptibility as a scalar quantity). The electrical susceptibilities will be given by the Eqs. 4.8.9 and 4.8.10. Substituting these relations into the expressions for the transmission and reflection coefficients, and accounting for the sign convention used in electrical engineering notation (where $j = -i$), we obtain the following state-dependent

coefficients:

$$
\begin{aligned}
|g\rangle_{atom} : t &= \frac{2}{2 + ik\chi^{EIT}} \\
|e\rangle_{atom} : r &= \frac{-ik\chi^{TA}}{2 + ik\chi^{TA}}.
\end{aligned}
\tag{4.8.13}
$$

These expressions provide the missing connection between the atomic control parameters and the unknown phase shift that the light acquires upon interaction with the Quantum Mirror. By calculating the argument of Eq. 4.8.13, we can map the phase response across the experimentally feasible parameter space defined by the detunings δ_p and δ_c (Figure 4.8.3).

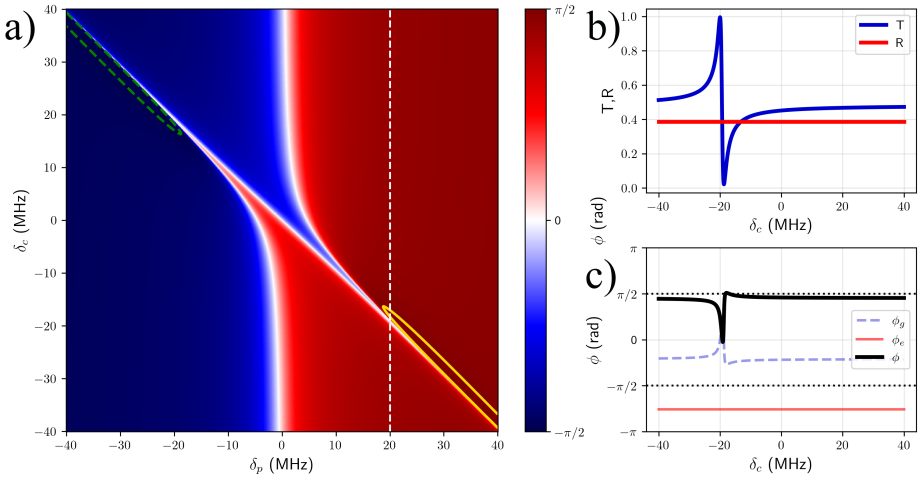

Figure 4.8.3: a) Calculated phase plot sweeping detunings δ_p and δ_c, which change the susceptibility response in both states. The white dotted line shows the cut that we have selected for the two figures on the right. b) Transmissivity and reflectivity coefficients $T = |t|^2$ and $|R|^2$, for the parameters in the while line of (a). c) Calculated phase, by definition $\phi = \arg(t/r)$, while considering the phase shift from the reflection $\phi_{refl} = \pi$.

However, this approach is not enough to describe the full interaction of the light with the metasurface, as we noticed that tuning the lattice constant $a_{lattice}$ can lead to significant and undesired losses of the reflection coefficient (see Figure 4.8.3), which makes the assumptions we previously made for the coefficients t and r no longer valid. This is a consequence of the fact that the interaction of light with a metasurface is not only determined by the bulk properties of the material, but

also by the specific geometry of the system with its boundary conditions and the cooperativity that arises from the collective behavior of the atoms set in that specific geometry (Bekenstein et al. (2020); Ballantine and Ruostekoski (2021)).

4.8.2.2 Cooperative Effects

When considering metamaterials (materials engineered to show responses that are not found naturally in their constituents), the composing elements typically show a separation smaller than the operating or resonant wavelength ($a < \lambda$). Specifically for the context of atomic lattices, Shahmoon et al. (2017) demonstrated that high reflection coefficients originate from the cooperative resonances of the dipolar array and its collective surface-wave excitations.
To accurately capture the resonance shifts induced by cooperative effects, one must consider the collective response of the atomic lattice. Through a collective polarizability description that accounts for inter-atomic interactions, we observe how the collective polarizability leads to shifts in the resonance frequencies and in the linewidths of the optical response, which in turn affect the reflection and transmission coefficients, a key component that was missing from the first approach.

While there are numerous methods to model these cooperative shifts across a metasurface, our primary interest lies in controlling electromagnetically induced transparency (EIT) through Rydberg blockades (Petrosyan et al. (2011)), including further considerations such as noise or disorder in the system (Ruostekoski (2023); Ballantine et al. (2022); Robicheaux (2025)). This theoretical progression leads us to the framework established by Lukin and Yelin, where one can prove that the effective polarizability tensor can be written as follows (considering an arbitrary polarization, which will later be simplified and treated as a scalar, just as we did in the previous section),

$$\bar{\bar{\alpha}}_e = -\frac{3\lambda_a^2}{4\pi^2}\frac{\gamma/2}{\delta - \bar{\bar{\Delta}}(\boldsymbol{k}_\parallel) + i(\gamma + \gamma_{nr} + \bar{\bar{\Gamma}}(\boldsymbol{k}_\parallel))/2}. \tag{4.8.14}$$

Here, γ_{nr} stands for non-radiative loss rate, and $\bar{\bar{\Delta}}(\boldsymbol{k}_\parallel)$, $\bar{\bar{\Gamma}}(\boldsymbol{k}_\parallel)$ are the cooperative resonance and width tensors, respectively given by a dyadic Green's function further discussed in (Shahmoon et al. (2017)). Under the assumption that there

is no phase acquired when light goes through in the transmissive state,

$$\boldsymbol{E} = \left[e^{ikz} + re^{ik|z|}\right] \boldsymbol{E}_0, \tag{4.8.15}$$

one can find the scalar solution for the reflection coefficient r

$$r(\delta) = i\pi \left(\frac{\lambda}{a}\right)^2 \frac{\alpha_e(\delta)}{\varepsilon_0 \lambda^3} = -\frac{i(\gamma + \Gamma)/2}{\delta - \Delta + i(\gamma + \gamma_{nr} + \Gamma)/2}, \tag{4.8.16}$$

where the past detuning and decays have been switched from tensors to scalar values, without losing the cooperative component. The cooperative widths have been experimentally measured (Rui et al. (2020)) and calculated; it has been shown that indeed the cooperative linewidth is smaller than that of an isolated atom.

However, throughout these works, there was no specific treatment of the *relative* phase ϕ, that has been extensively discussed in the present work. With the added assumption that there is no phase acquired when light goes through in the transmissive state; this assumption breaks down once we move away from the perfect EIT condition ($\Delta_2 = 0$).

This is further proved by the fact that even when increasing the lattice constant $a_{lattice}$, which should lead to a decrease in the interaction between the atoms and thus a decrease in the cooperative effects, we still observe significant reflections, which can be attributed to the cooperative resonances at the surface of the lattice (Javanainen and Rajapakse (2019)) making it a strong candidate for quantum mirror applications or other quantum technologies that require of stable scaling (Moreno-Cardoner et al. (2021)).

While the past works have completely ignored the relative phase ϕ that originates from the interaction with the metasurface, it has been shown that it does indeed exist and is easily manipulated, specially in the context of induced or natural magnetic susceptibilities, which can give a full 2π phase range (Ruostekoski (2023); Ballantine et al. (2022); Ballantine and Ruostekoski (2021)).

4.9 Conclusion

Figure 4.8.3 shows that the phase ϕ can be effectively tuned across a wide range of values by adjusting experimental parameters such as the detunings δ_p and δ_c in this case. This tunability is a promising feature for the practical implementation of quantum mirrors for quantum state tomography, a process that, before quantum mirrors, relied heavily on the ability to reconstruct probability distributions through homodyne measurements. We expect that with further understanding of the atom-atom interactions that affect the optical response, it will be possible to achieve even more precise control over the quantum mirror.

Throughout this chapter, we have established a comprehensive theoretical framework for the operation of a quantum mirror, and successfully verified the breaking of parity operator symmetry in the presence of external phases. Although ideal in its symmetry and non-lossy assumptions, we derived the specific tomography measurement protocols for the Q, P and Wigner representations of a quantum state. Furthermore, we explored and clarified a fundamental relationship between the coefficients t and r and the global phase ϕ, a connection often treated as trivial, but which we have shown to be central to the device's operation.

It should be mentioned that although we have focused on a specific implementation using Rydberg-mediated metasurfaces, the principles outlined in this work are broadly applicable to other systems capable of exhibiting similar quantum mirror behavior. Cavity QED systems with Rydberg atoms (Magro et al. (2023)), single ions in cavities acting as mirrors (Hétet et al. (2011b)), interactions with plasmonic nanocavities (He and Zhu (2023)), among others, are potential candidates for quantum mirrors, and yet to be explored.

5

Nonlinear Bragg Lattices in Atomic Vapors

Forever Howlong

Black Country New Road

5.1 Introduction

This chapter discusses the theoretical and experimental details relating to the possibility of making an effective Bragg Grating inside atomic vapors through modulation via Stark shifts. Under this context, interesting effects arise from nonlinearities in the index of refraction of rubidium, potentially offering all-optical switching control over the Bragg lattice. To fully grasp the importance of implementing such a structure in atomic vapours, we first must look at the fundamentals of this phenomenon.

Bragg scattering is a phenomenon often associated to condensed matter physics, commonly used to determine crystal structure of materials (Wolff et al. (2021)), however, its importance is seen by all areas of optics and related fields. For example, the discovery of Bragg scattering (Bragg (1913)) led to groundbreaking discoveries, such as the discovery of DNA double helix structure (Thomas (2012)), precise measurements of atomic distances in crystals, and even precision gravitometry (Altin et al. (2013)). Bragg scattering occurs when waves incident on a crystalline medium undergo constructive interference due to the periodic arrangement of scattering planes. When the incident light's wavelength λ is comparable to the periodicity d of the structure, an interference between the incoming and reflected fields leads to enhanced reflection at specific angles. This is generally described through Bragg's law:

$$n\lambda = 2d\sin\theta, \tag{5.1.1}$$

where n corresponds to the order of the diffraction and θ to the angle which is measured from where the lattice planes are with respect to the incident wave. This relationship describes how the constructive interference inside the periodic layers in the medium results in an output, the one which we distinguish as the Bragg scattered wave. In this work, we consider the first order Bragg scattering ($n = 1$) in a normal incidence configuration ($\theta = 90°$), which simplifies Bragg's law to $\lambda = 2d$.

A natural extension of this concept is to consider media outside the range of condensed matter physics, such as atomic vapours. Indeed, researchers have already demonstrated the ability to optically modulate the index of refraction in a periodic manner; through optical lattices (Deutsch et al. (1995)), or through standing waves in warm vapours (Strekalov et al. (2007)). In cold atomic systems, these periodic structures have shown to produce measurable scattering (Miyake et al. (2011), Weidemüller et al. (1995)), and even collective effects that can be further exploited (Asselie et al. (2025)).

While cold atomic systems offer a clean and easily controllable platform, they are also incredibly complex to build and maintain. Creating cold atomic clouds require an amount of resources often out of reach for many laboratories. As such, one turns to more accessible platforms, such as warm atomic vapors (i.e. rubidium cells), which provide a simpler and straightforward setup, without the need for complex cooling systems. Atomic vapors can be used at room temperature or slightly heated, and are usually contained in simple glass cells.

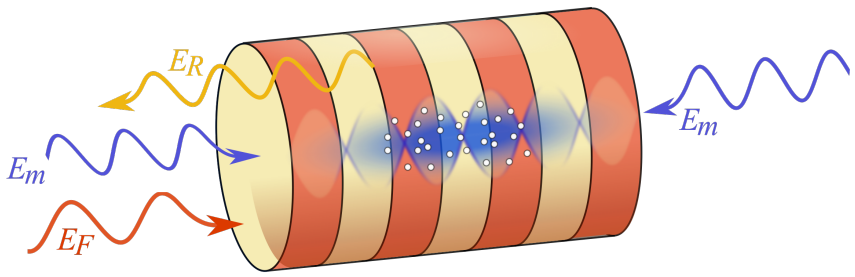

Figure 5.1.1: Illustration of the Bragg scattering process in an atomic vapor. A standing wave (E_m in blue) creates a periodic modulation of the refractive index inside the vapor cell, forming a Bragg grating. A probe beam (E_F, in red) is incident on the cell, and part of it is reflected due to the Bragg scattering effect. The reflected light (E_R, in yellow) is detected by a photodetector.

Although thermal noise results in interaction times that are much lower than

in their colder counterparts, warm vapors can be highly nonlinear compared to traditional fiber optics. This allows us to harness nonlinearities for various optical purposes (Fang et al. (2015), Grynberg et al. (1994)), including applications in high resolution spectroscopy (Wang et al. (2010)) and quantum technologies (Borba et al. (2017)). Within this niche area of research, effects of saturation (Häupl et al. (2025)) and bistabilities (Joshi and Xiao (2010), An et al. (2022), Novikova et al. (2004)) have been observed, which provide mechanisms for all-optical switching (Dawes et al. (2005), Raja et al. (2024)). However, a comprehensive study of both the nonlinearities and bistabilities of the Bragg medium in warm atomic vapors, including both theoretical modeling and experimental realization, remains an open area of research.

In the following sections we discuss the theoretical framework needed to understand how we can create a Bragg grating in a warm atomic vapour, considering all variables in the system; we center ourselves in the Bragg grating modulation through a Stark shift by a counter-propagating standing wave, while the medium can be saturated by the incident probe. We will also review the experimental setup designed to measure this effect, and the results obtained. We conclude with the implications of these results and future prospects for this line of research.

5.2 Index of Refraction Perturbations

A counter-propagating standing wave with spatial period Λ will induce an AC Stark shift with the same periodicity. Consequently, the refractive index may be written as a sum of an unperturbed index of refraction, and a spatially modulated term, as follows:

$$n \approx n_0 + n_{\text{Stark}} \cos(2\pi z/\Lambda). \tag{5.2.1}$$

We also know that for two-level atom in a linear, isotropic, homogeneous system, its optical response is characterized by its susceptibility χ,

$$\chi = -\frac{\alpha_0}{k_p} \frac{2\delta_p/\Gamma_e - i}{(2\delta_p/\Gamma_e)^2 + 1}, \tag{5.2.2}$$

where δ_p is the probe detuning, Γ_e is the excited-state decay rate, $\alpha_0 = N\sigma_0$ characterizes the resonant absorption strength, and k_p is the probe wavevector. At higher intensities, saturation effects become relevant, and the susceptibility is

modified to

$$\chi = -\frac{\alpha_0}{k_p}\frac{2\delta_p/\Gamma_e - i}{(2\delta_p/\Gamma_e)^2 + 1 + |E|^2/|E_s|^2}, \tag{5.2.3}$$

where $|E|^2$ is the probe intensity and $|E_s|^2$ is the saturation intensity of the transition. For our final consideration, we include the effect of the Stark shift $\delta_{\text{Stark}} = \delta_S \cos(2\pi z/\Lambda)$ induced by the standing wave, which modifies the probe detuning as $\delta_p \to \delta_p - \delta_{\text{S}} \cos(2\pi z/\Lambda)$, effectively shifting the resonance frequency of the atoms. Thus, the susceptibility becomes

$$\chi = -\frac{\alpha_0}{k_p}\frac{2(\delta_p - \delta_{\text{Stark}})/\Gamma_e - i}{(2(\delta_p - \delta_{\text{Stark}})/\Gamma_e)^2 + 1 + |E|^2/|E_s|^2}. \tag{5.2.4}$$

We remember that $n = \sqrt{1+\chi}$ and as such we can calculate the index of refraction as the taylor expansion for Eq. 5.2.4, for the Stark shift perturbation, while considering saturation $S = |E|^2/|E_s|^2$,

$$n \approx 1 - \frac{1}{2}\frac{\alpha_0}{k_p}\frac{2\delta_p/\Gamma_e - i}{(2\delta_p/\Gamma_e)^2 + 1 + S} + \frac{1}{2}\frac{\alpha_0}{k_p\Gamma_e}\frac{1 + S - (2\delta_p/\Gamma_e)^2 + 2(2\delta_p/\Gamma_e)i}{((2\delta_p/\Gamma_e)^2 + 1 + S)^2}\delta_S \cos(2\pi z/\Lambda). \tag{5.2.5}$$

We summarize the index of refraction modulation as the following equations, noting the fact that these are complex quantities, with both real and imaginary parts. As such, absorption effects are inherently included in this model.

$$n \approx n_0 + n_{\text{Stark}} \cos(2\pi z/\Lambda) \tag{5.2.6}$$

$$n_0 = 1 - \frac{1}{2}\frac{\alpha_0}{k_p}\frac{2\delta_p/\Gamma_e - i}{(2\delta_p/\Gamma_e)^2 + 1 + S} \tag{5.2.7}$$

$$n_{\text{Stark}} = \frac{1}{2}\frac{\alpha_0}{k_p\Gamma_e}\frac{1 + S - (2\delta_p/\Gamma_e)^2 + 2i(2\delta_p/\Gamma_e)}{\left((2\delta_p/\Gamma_e)^2 + 1 + S\right)^2}\delta_S. \tag{5.2.8}$$

In the search for valid ranges of this approximation, we find that if the perturbations order is less than 6 MHz, the approximated model approaches the full description as seen in Fig. 5.2.1.

As we can see in Fig. 5.2.1, the refractive index modulation n_{Stark} depends strongly on both the probe detuning δ_p and the Stark shift detuning δ_{Stark}. Notably, the Stark modulation shifts the whole resonance, as expected. Further increasing

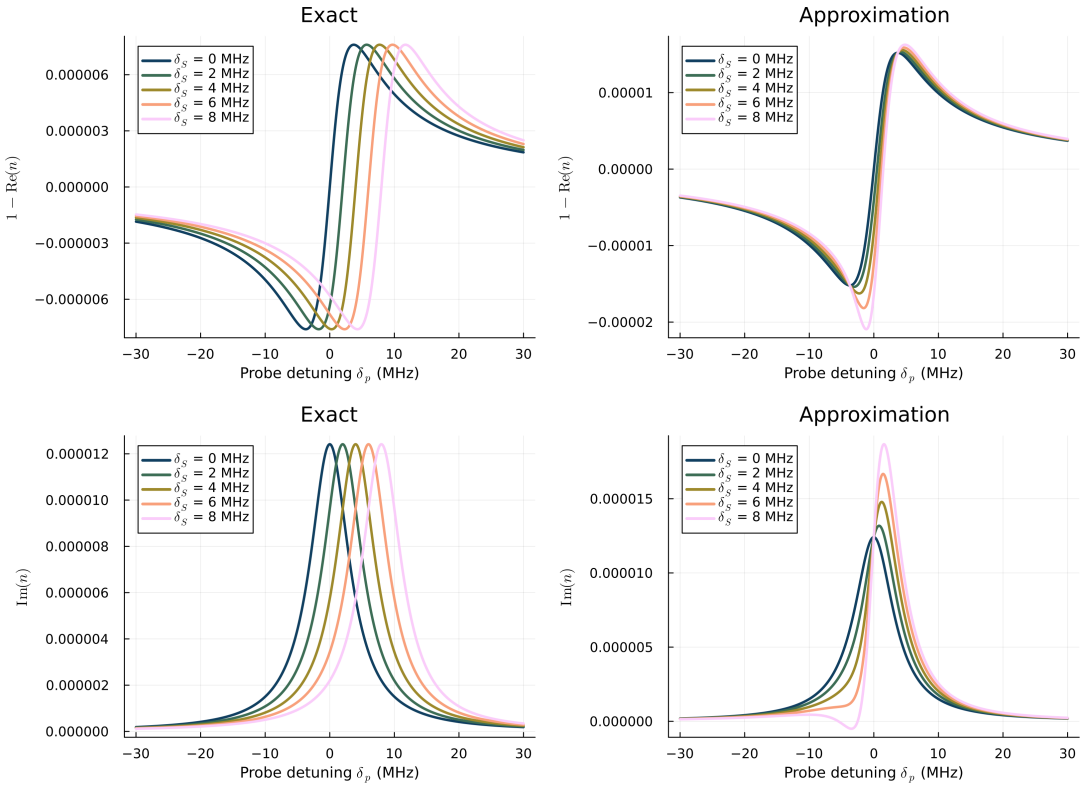

Figure 5.2.1: Variations of the real and imaginary components of the refractive index modulation induced by the Stark shift acting on the two-level atom, compared to the true expression under no approximation. Plotted as a function of the probe detuning δ_p for different values of the Stark shift detuning, being fixed at different values of detuning. The saturation parameter is fixed at $S = 0.5$.

the Stark shift detuning δ_{Stark} enhances the magnitude of the index modulation, thereby strengthening the Bragg grating effect.

5.3 Coupled Mode Theory

In order to effectively describe the interaction of the incident and reflected light present in the Bragg grating, considering the nonlinearities of the atomic cloud, we turn to the coupled mode theory (CMT). In the CMT, one assumes that there are two translationally variant channels, presenting transference of power. The rate of this power exchange depends on a coupling parameter given by the medium characteristics. We assume the power should be conserved, so any difference will be transfered to other modes. In the case of fiber Bragg gratings for example, the coupling takes place only in the forward and backward propagating fundamental modes (Erdogan (1997)), that is, assuming that no loss occurs.

Starting from the Helmholtz equation, for a monochromatic linearly polarized field, travelling only in the z direction:

$$\frac{\partial^2 E(\mathbf{r})}{\partial z^2} + k_0^2 n^2 E(\mathbf{r}) = 0, \tag{5.3.1}$$

and from Eq. 5.2.5, we can write $n^2 \approx n_0^2 + 4n_0 n_S^2 \cos(2\pi z/\Lambda)$, and use the following ansatz

$$E_{total} = E_+(z)e^{i\beta z} + E_-(z)e^{-i\beta z}, \tag{5.3.2}$$

where E_+ and E_- correspond to the forward and backward solutions respectively. β is the propagation constant of the mode in the unperturbed medium. Substituting the ansatz into the Helmholtz equation, we obtain:

$$\begin{gathered}(2i\beta\frac{\partial E_+}{\partial z} - \beta^2 E_+)e^{i\beta z} - (2i\beta\frac{\partial E_-}{\partial z} + \beta^2 E_-)e^{-i\beta z} + \\ k_0^2(n_0^2 + 4n_0 n_S\cos(2\pi z/\Lambda))(E_+e^{i\beta z} + E_-e^{-i\beta z}) = 0.\end{gathered} \tag{5.3.3}$$

Writing the cosine modulation in exponential form and retaining only the near phase-matched terms (terms with a slowly varying phase), we have:

$$\frac{1}{2}(e^{-i(2\pi z)/\Lambda} + e^{i(2\pi z)/\Lambda})e^{\pm i\beta z}E_\pm = \frac{1}{2}e^{\mp i(\beta - 2\bar{\delta})z}E_\pm, \tag{5.3.4}$$

where $\bar{\delta} = \beta - \pi/\Lambda$ is the detuning from the Bragg condition. This periodic

modulation couples the forward and backward modes through the spatial Fourier components of the refractive index (Erdogan (1997), Yariv and Yeh (2002)),

$$\begin{aligned} 2i\beta\partial_z E_+ e^{i\beta z} - \beta^2 E_+ e^{i\beta z} + k_0^2 n_0^2 E_+ e^{i\beta z} + 2k_0^2 n_0 n_S e^{i(\beta-2\bar{\delta})z} E_- &= 0 \\ -2i\beta\partial_z E_- e^{-i\beta z} - \beta^2 E_- e^{-i\beta z} + k_0^2 n_0^2 E_- e^{-i\beta z} + 2k_0^2 n_0 n_S e^{-i(\beta-2\bar{\delta})z} E_+ &= 0, \end{aligned} \tag{5.3.5}$$

Finally, we switch to studying only the envelopes of this system, as we are no longer interested in the oscillations of the electric fields but the power transfer. There is an extra dephase between the coupling of both equations given by the term $e^{-i2\bar{\delta}z}E_-$, so we write the field solutions as $E_+(z) = A_f(z)e^{-i\bar{\delta}z}$ and $E_-(z) = A_b(z)e^{i\bar{\delta}z}$. Substituting these and remembering $\beta \approx k_0 n_0$, we arrive at the known expression for the CMT:

$$\partial_z A_f(z) = ik_0 n_S A_b(z) + i\bar{\delta} A_f(z) \tag{5.3.6}$$

$$\partial_z A_b(z) = -ik_0 n_S A_f(z) - i\bar{\delta} A_b(z). \tag{5.3.7}$$

These are the coupled mode equations that we will solve in the following sections.

5.4 Preliminary Results

5.4.0.1 Parameter Calculations

The dimensionless parameter α_0, which sets the overall scale of the medium's susceptibility, was computed using

$$\alpha_0 = k_p \frac{N\mu^2}{\epsilon_0 \hbar \Gamma_e}.$$

Here, N is the atomic number density, μ is the dipole matrix element for the Rb^{87} D_2 line, Γ_e the natural linewidth.

Using parameters appropriate for a cold atomic cloud, that is, $N \sim 10^{16}\,\mathrm{m}^{-3}$, $\mu = 3.584 \times 10^{-29}\,\mathrm{C}\cdot\mathrm{m}$, $\lambda_p = 780\,\mathrm{nm}$, and $\Gamma = 2\pi \times 6.06\,\mathrm{MHz}$, we evaluate and substitute into the expression above, yielding $\alpha_0 \approx 3.0 \times 10^3$.

Physically, α_0 acts as a normalization factor for the electric susceptibility, allowing it to be written as a dimensionless lineshape function scaled by α_0. It is also proportional to the resonant optical depth, with $\mathrm{OD} \sim \alpha_0 L$ for a medium of

length L, due to Beers Law.

For the Stark shift calculations, we calculated

$$\begin{aligned} \Delta E &= -\alpha_e^{(0)}(\lambda_c) I_{sat} \frac{\eta_0}{2} \\ \Delta E &= -\alpha_g^{(0)}(\lambda_c) I_{sat} \frac{\eta_0}{2} \end{aligned} \tag{5.4.1}$$

where $\alpha_e^{(0)} = 2.37 \times 10^{-27}$ and $\alpha_g^{(0)} \approx 0$. We then transform the energy into a frequency shift through the equivalence $\Delta E/(2\pi\hbar) = \Delta\omega$.

5.4.0.2 Numerical Solutions

The reflectivity of a uniform grating of length L can be found by assuming a forward-going wave incident from $z = 0$, and requiring that no backward-going wave exists for $z = L$. This corresponds to the following boundary conditions:

$$\begin{aligned} A_f(0) &= A_{in} \\ A_b(L) &= 0. \end{aligned} \tag{5.4.2}$$

In order to solve the coupled mode equations, we consider a backward propagation integration of the system. What follows is the implementation of this integration scheme alongside some preliminary and exploratory results.

For the backward propagation, the integration is done through a high-order Adaptive Stepsize Runge-Kutta solver in the Julia programming language. The expected output mode $A_f(L)$, is used as initial condition for the backward propagation alongside with the known boundary condition $A_b(L) = 0$. The system is integrated, and we obtain the values for the input mode as well as the reflected mode at the origin $A_f(0)$ and $A_b(0)$ respectively. Finally, we can calculate the reflectivity of the system as $R = |A_b(0)|^2/|A_f(0)|^2$. By sweeping through a range of expected output values, we map the corresponding input intensities. This method effectively traces the curves in Fig. 5.4.2, which have been plotted to show the different response of the medium when considering the two different models (with losses and without them). An adiabatic step in the boundary counditions of the input intensity is considered to the integration in order to avoid numerical instabilities.

In Fig. 5.4.1, we observe two important characteristics. Firstly, the perturbed

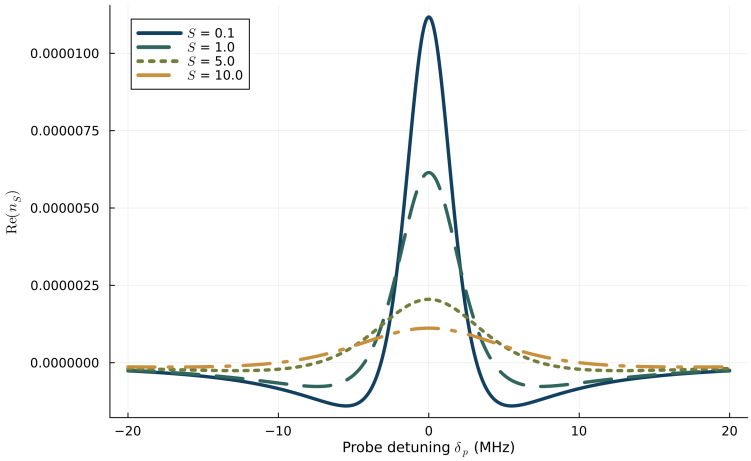

Figure 5.4.1: Response of n_S under different incident intensities. $\mathrm{Re}(n_S)$ corresponds to the component of the index of refraction that controls how the Bragg grating will reflect, as it controls the dispersion response which directly affects the phase gained by the light as is goes through the medium.

index of refraction n_s shows a decrease in amplitude as the intensity grows. This behavior is a direct consequence of the power broadening effect, and can be directly correlated to the inherent saturation response of the atoms. As more power is injected into the system, this response flattens out, which completely saturates and destroys the lattice. Secondly, we note there is a change in sign as we vary the detuning. As we sweep the input intensity, the difference in signs of the index of refraction could cancel out ($n_S = 0$), momentarily erasing the grating, which can be seen in the "revivals" of reflectivity from Fig. 5.4.2.

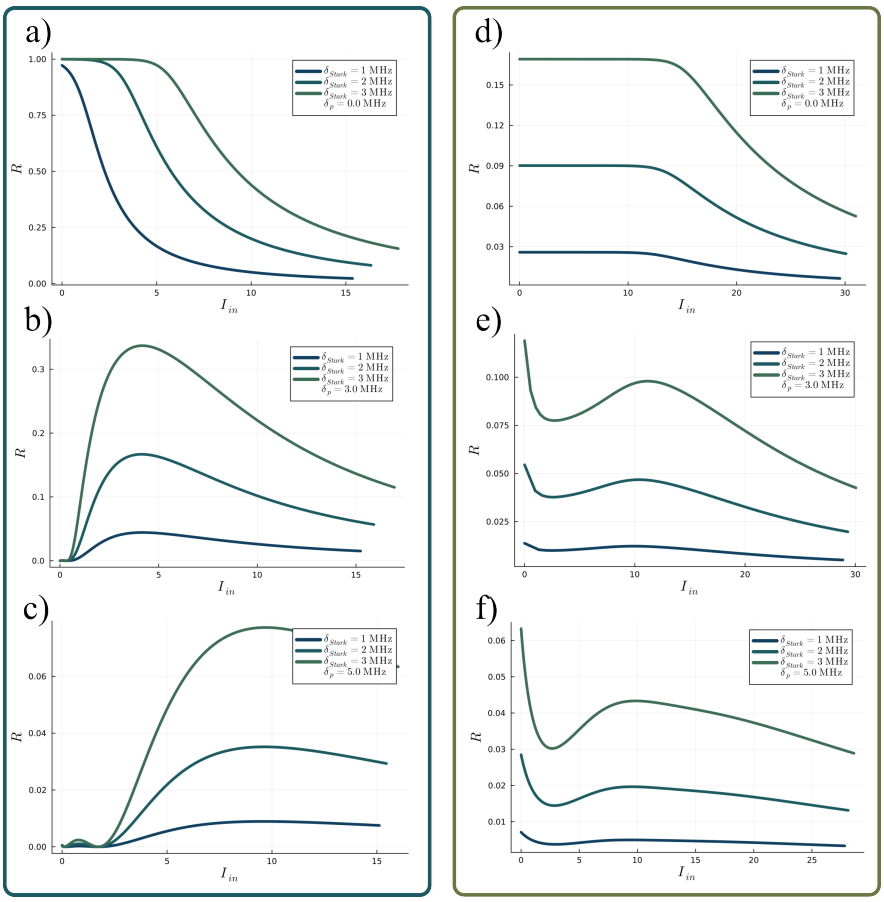

Figure 5.4.2: Preliminary results for the backward propagation integration method. a) Input intensity obtained from a fixed output boundary condition, illustrating the dependence on the Stark detunings δ_{Stark}, leading to the different dynamical regimes present in the medium. (a), (b) and (c) correspond to the Reflectivity of the medium under an intensity sweep, with $\delta_p = 0, 3, 5$ MHz respectively. (d), (e) and (f) are analogous to the left-side, but considering losses in the system.

5.4.1 Warm Vapours Considerations

In warm atomic vapors, the number density of atoms N is a crucial parameter that influences the strength of the refractive index modulation (as the optical response of the medium as we are modelling it depends on the bulk of the vapor). The number density can be estimated using the vapor pressure of rubidium, which is temperature-dependent (Steck (2001)).

The number density can be controlled by adjusting the temperature of the vapor cell. As the temperature increases, the vapor pressure of rubidium increases, leading to a higher number density of atoms in the vapor phase. This model

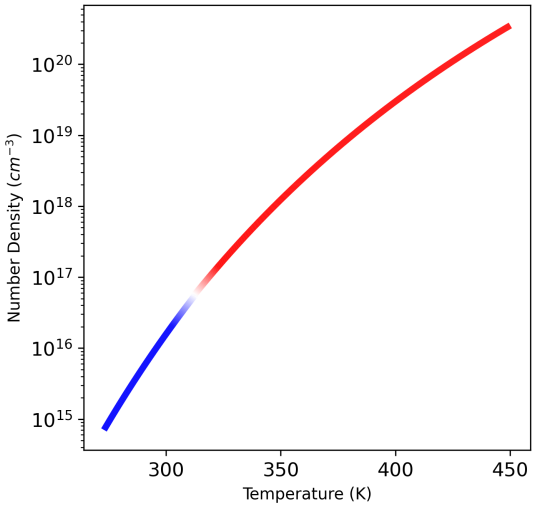

Figure 5.4.3: Number density of Rb^{87} plotted as a function of the temperature of the vapor cell. The white spot between the blue and red line correspond to the transition from solid to liquid phase. Code was referenced from Di Domenico and Weis (2011) but performed in Python.

(5.4.3) allows us to set a value for the number density of atoms N in the vapor cell, which is a crucial parameter for determining the strength of the refractive index modulation. This parameter is considered in the value of α_0 in Eq. 5.2.4, along with every approximation after it, as part of the optical density $\alpha_0 = N\sigma_0$, with $\sigma_0 \approx 3\lambda^2/2\pi$ being the atomic cross-section.

One further consideration in warm vapors is the Doppler broadening (see Section 2.4.3) of the atomic resonance due to the thermal motion of the atoms. As we have seen, this effect considers the distribution of atomic velocities due to the thermal motion, which in turn causes a broadening of the resonance line shape. We will incorporate this effect into our model by averaging the susceptibility over the Doppler-broadened velocity distribution of the atoms. This is done by integrating the susceptibility over the Maxwell-Boltzmann distribution of atomic velocities, leading to an effective susceptibility that accounts for the Doppler broadening. This effective susceptibility will then be used to calculate the refractive index modulation in the presence of thermal motion.

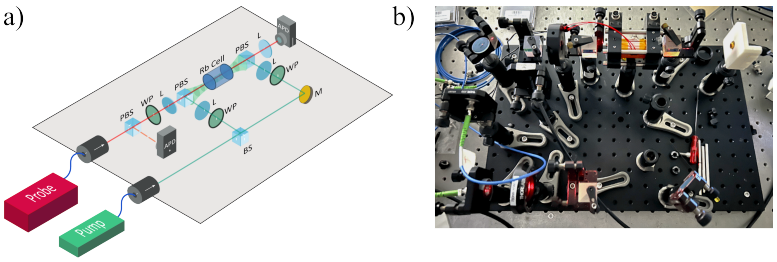

Figure 5.5.1: Experimental set up. a) illustration of the designed experiment. b) photograph of the actual setup. PBS stand for Polarizing Beam Splitter, WP for Wave Plate, APD for Photodetector, BS for Beam Splitter, L for lens, M for mirror.

5.5 Experiment

Due to time contraints inherent to the duration of a master's degree, it was not possible to realize measurements on the present project. This section therefore describes the experimental design and our contributions in preparations for future explorations and measurements.

The experimental setup designed to measure the expected Bragg scattering is illustrated in Fig. 5.5.1. The core of the setup consists of a rubidium vapor cell, which can be heated to a temperature of around 100° C in order to increase the atomic density. A standing wave is created inside the cell using two counter-propagating laser beams, which should be detuned from the atomic resonance to minimize absorption while maximizing the refractive index modulation. The standing wave creates a periodic modulation of the refractive index in the vapor, forming the Bragg-Stark grating.

A probe laser beam is then directed into the cell, and the reflected light is detected using a photodetector (APD). For balancing purposes, a portion of the probe beam is split off before entering the cell to serve as a reference for normalization of the detected signal; as well as at the output of the cell. Various optical components such as lenses, mirrors, beam splitters, polarizing beam splitters, and wave plates are used to control the beam paths, polarizations, and intensities. Special care was taken to ensure the precise alignment of the counter-propagating beams to create a stable and well-defined standing wave inside the vapor cell. The polarizations of the beams were also carefully controlled to maximize the interference contrast. The probe beam may be aligned at a slight angle with respect to the standing

wave in order to satisfy the Bragg condition for scattering.

The pump beam is split by a beam splitter, and the two resulting beams are directed to enter the Rb cell from opposite directions. When these two counter-propagating beams overlap, they interfere to form a standing wave. The probe beam is directed into the Rb cell. Because of the periodic modulation created by the pump, a portion of the probe is reflected (Bragg scattered) back toward the first polarizing beam splitter.

5.6 Discussion

Although exploratory in its beginnings, we have established an exploratory theoretical and experimental framework for future investigations into Bragg scattering in atomic vapors. The theoretical model developed provides a clear understanding of how the refractive index modulation arises from the AC Stark effect induced by a standing wave, and how this modulation can be harnessed to create an effective Bragg grating.

We anticipate that future experiments (even in cold atomic systems) will be able to validate the predictions of our coupled mode theory approximation, and reveal the nonlinear dynamics that may arise in this system. We also note the huge parameter space, as an opportunity for further exploration, including variations in the Stark effect modulation (via intensity or detuning control), probe detuning, atomic density (via temperature control), and further configuration variations (such as exploiting EIT responses). Each of these parameters can significantly influence the strength and characteristics of the Bragg scattering observed; but the strongest effects arise from the interplay between Stark modulation and probe saturation.

Current ongoing research focuses on the addition of optical losses in the system given by the imaginary part of the refractive index. This will allow us to explore the interplay between gain and loss in the Bragg grating, potentially leading to exciting phenomena such as non-reciprocal behavior (Zhang et al. (2024)).

Finally, further studies on the temporal dynamics of the scattering process under pulsed excitation conditions could reveal transient phenomena and provide insights into the response times of the system, which are crucial for applications in optical

switching. For instance, research into optical solitons, which can form under saturable lattices (Malomed et al. (2005)), in the proposed atomic mirrors could open new avenues for robust information transmission (Shou and Huang (2021)).

6

Conclusions and Future Work

6.1 Summary

In this thesis, we have investigated several key aspects of quantum light generation and manipulation using atomic ensembles. We have managed to exploit the unique properties of these ensembles to achieve significant advancements not only in the theoretical understanding but also in practical implementations for the future development of quantum technologies; hopefully paving the way for the long dreamed *quantum internet*. Between our contributions, we remark the study of nonlinear optical effects in rubidium vapor, the experimental generation of single photons on demand, and the theoretical framework of a quantum mirror for quantum state tomography. A summary of each chapter and its most significant contributions is presented below, along with potential directions for future research.

6.1.1 Chapter 3

Chapter 3 focused on the generation of single photons using a rubidium atomic ensemble. Through the implementation of the DLCZ and Superradiance protocols, we successfully generated correlated Stokes and anti-Stokes photon pairs. This controlled generation allowed us to characterize different parameters in order to optimize and compare each protocol. Through data analysis, we canaged to study the second order correlation function $g^{(2)}_{S,AS}$, the conditional retrieval efficiency, and the generation probability of the spinwave and the coincidences. Our experimental results demonstrated that while both protocols are capable of producing high-quality single photons, the superradiance protocol showed enhanced performance due to collective effects in the atomic ensemble, specifically in lower write power contexts.

We expect future work in this area could improve detection efficiency, further characterize the temporal profile of the emitted anti-Stokes photons; as well as confirm the validity of the single photon regime through autocorrelation

measurements, thereby strengthening the experimental results and providing a new platform for single-photon generation for quantum technologies.

6.1.2 Chapter 4

We presented a comprehensive theoretical framework that defines the operation of a quantum mirror, a novel tool that we expect could ease the experimental and numerical difficulties that appear in quantum state tomography. Through various examples and generalizations, we derived the specific tomography measurement protocols for the Q, P and Wigner representations of a quantum state. We also identified and successfully verified the breaking of parity operator symmetry in the presence of external phases, which corresponds to the key element in the tomographic process. Finally, we extended this work to study the experimetal feasibility of the controllable parity operator quantum mirror, by shedding light into a fundamental relationship between the coefficients t and r and the global phase ϕ, a connection often treated as trivial, but which we have shown to be central to the device's operation.

The tunability of the quantum mirror is a promising feature for the practical implementations of quantum state tomography, a process that, before quantum mirrors, relied heavily on the ability to reconstruct probability distributions through homodyne measurements. We expect that with further optimization of the experimental parameters, it will be possible to achieve even more precise control over the quantum mirror.

Furthermore, we expect that several, useful applications for the quantum mirror will be found. The versatility of this technology opens doors to developing algoritms capable of directly studying and quantifying the 'quantumness' or Wigner negativity without the need of reconstruction methods, which could prove to ve valuable in particular for the study of non-Gaussian quantum states. Outside of tomography, quantum mirrors have shown effective for quantum teleportation protocols.

6.1.3 Chapter 5

In Chapter 5, we explored the nonlinear optical properties of a rubidium atomic vapor subjected to a periodic modulation of its refractive index, induced by an off-

resonant standing wave that generates a spatially dependent Stark shift, effectively acting as a Bragg Mirror with switchable capabilities.

Our findings demonstrated that by tuning the optical depth, the saturation of the probe and the Stark shift induced detunings, one is able to create a switchable nonlinear mirror for incoming light. The inclusion of losses in the model further confirms the emergence of multistable behavior in the system.

An experimental scheme was designed and implemented to validate these theoretical predictions. Extensions of this work are currently underway, specifically focused on a more complete treatment of warm-vapor effects, including Doppler broadening and temporal response. Future work could extend this study to the regime of short optical pulses and low intensities, where the strong nonlinearity of rubidium may enable slow-light or low-power optical switching.

Bibliography

Achouri, K., Salem, M. A., and Caloz, C. (2015). General metasurface synthesis based on susceptibility tensors. *IEEE Transactions on Antennas and Propagation*, 63(7):2977–2991.

Aladjidi, T., Abuzarli, M., Brochier, G., Bienaimé, T., Picot, T., Bramati, A., and Glorieux, Q. (2022). Transit effects for non-linear index measurement in hot atomic vapors.

Altin, P. A., Johnsson, M. T., Negnevitsky, V., Dennis, G. R., Anderson, R. P., Debs, J. E., Szigeti, S. S., Hardman, K. S., Bennetts, S., McDonald, G. D., Turner, L. D., Close, J. D., and Robins, N. P. (2013). Precision atomic gravimeter based on bragg diffraction. *New Journal of Physics*, 15(2):023009.

An, H., Owens, H., Ather, H., Shakouri, A., and Hosseini, M. (2022). Intensity instability and correlation in amplified multimode wave mixing. *Scientific Reports*, 12.

Anderson, M. H., Ensher, J. R., Matthews, M. R., Wieman, C. E., and Cornell, E. A. (1995). Observation of bose-einstein condensation in a dilute atomic vapor. *Science*, 269(5221):198–201.

Anshu, A. and Arunachalam, S. (2024). A survey on the complexity of learning quantum states. *Nature Reviews Physics*, 6(1):59–69.

Aspect, A. (2019). *Hanbury Brown and Twiss, Hong Ou and Mandel effects and other landmarks in quantum optics: from photons to atoms*, pages 428–449. Oxford University Press.

Asselie, S., Nazon, J.-M., Caldani, R., Roux-Spitz, C., and Guerin, W. (2025). Temporal dynamics in the bragg reflection of light by cold atoms: Flash effect and superradiant decay. *Physical Review A*, 112(5).

Ballantine, K. E. and Ruostekoski, J. (2021). Cooperative optical wavefront engineering with atomic arrays. *Nanophotonics*, 10(7):1901–1909.

Ballantine, K. E., Wilkowski, D., and Ruostekoski, J. (2022). Optical magnetism and wavefront control by arrays of strontium atoms. *Physical Review Research*, 4(3).

Banaszek, K., Radzewicz, C., Wódkiewicz, K., and Krasiński, J. S. (1999). Direct measurement of the wigner function by photon counting. *Physical Review A*, 60(1):674–677.

Banaszek, K. and Wódkiewicz, K. (1996). Direct probing of quantum phase space by photon counting. *Physical Review Letters*, 76(23):4344–4347.

Bechhoefer, J. (2005). Feedback for physicists: A tutorial essay on control. *Reviews of Modern Physics*, 77(3):783–836.

Bekenstein, R., Pikovski, I., Pichler, H., Shahmoon, E., Yelin, S. F., and Lukin, M. D. (2020). Quantum metasurfaces. In *OSA Quantum 2.0 Conference*, page QW5B.3, Washington, D.C. Optica Publishing Group.

Berezhiani, L. and Zantedeschi, M. (2021). Evolution of coherent states as quantum counterpart of classical dynamics. *Physical Review D*, 104(8).

Bertet, P., Auffeves, A., Maioli, P., Osnaghi, S., Meunier, T., Brune, M., Raimond, J. M., and Haroche, S. (2002). Direct measurement of the wigner function of a one-photon fock state in a cavity. *Physical Review Letters*, 89(20).

Blumenthal, D. J., Isichenko, A., and Chauhan, N. (2024). Enabling photonic integrated 3d magneto-optical traps for quantum sciences and applications. *Optica Quantum*, 2(6):444–457.

Borba, G. C., Felinto, D., and Tabosa, J. W. R. (2017). Nonlinear optical memory: theory and experiment. *Journal of the Optical Society of America B*, 34(12):2528.

Bornet, G., Emperauger, G., Chen, C., Ye, B., Block, M., Bintz, M., Boyd, J. A., Barredo, D., Comparin, T., Mezzacapo, F., Roscilde, T., Lahaye, T., Yao, N. Y., and Browaeys, A. (2023). Scalable spin squeezing in a dipolar rydberg atom array. *Nature*, 621(7980):728–733.

Boyd, R. (2020). *Nonlinear Optics*. Academic Press, Elsevier.

Bragg, W. L. (1913). The diffraction of short electromagnetic waves by a crystal. *Proceedings of the Cambridge Philosophical Society*, 17:43–57.

Cahill, K. E. and Glauber, R. J. (1969). Density operators and quasiprobability distributions. *Physical Review*, 177(5):1882–1902.

Campos, R. A., Saleh, B. E. A., and Teich, M. C. (1989). Quantum-mechanical lossless beam splitter: Su(2) symmetry and photon statistics. *Physical Review A*, 40(3):1371–1384.

Chang, D. E., Sørensen, A. S., Demler, E. A., and Lukin, M. D. (2007). A single-photon transistor using nanoscale surface plasmons. *Nature Physics*, 3(11):807–812.

Chen, W., Beck, K. M., Bücker, R., Gullans, M., Lukin, M. D., Tanji-Suzuki, H., and Vuletić, V. (2013). All-optical switch and transistor gated by one stored photon. *Science*, 341(6147):768–770.

Corwin, K. L., Lu, Z.-T., Hand, C. F., Epstein, R. J., and Wieman, C. E. (1998). Frequency-stabilized diode laser with the zeeman shift in an atomic vapor. *Applied Optics*, 37(15):3295.

Couteau, C., Barz, S., Durt, T., Gerrits, T., Huwer, J., Prevedel, R., Rarity, J., Shields, A., and Weihs, G. (2023). Applications of single photons to quantum communication and computing. *Nature Reviews Physics*, 5(6):326–338.

Dahmani, B., Hollberg, L., and Drullinger, R. (1987). Frequency stabilization of semiconductor lasers by resonant optical feedback. *Opt. Lett.*, 12(11):876–878.

Dalibard, J. and Cohen-Tannoudji, C. (1989). Laser cooling below the doppler limit by polarization gradients: simple theoretical models. *Journal of the Optical Society of America B*, 6(11):2023.

Dawes, A. M. C., Illing, L., Clark, S. M., and Gauthier, D. J. (2005). All-optical switching in rubidium vapor. *Science*, 308(5722):672–674.

Delone, N. B. and Krainov, V. P. (1999). Ac stark shift of atomic energy levels. *Physics-Uspekhi*, 42(7):669–687.

Deutsch, I. H., Spreeuw, R. J. C., Rolston, S. L., and Phillips, W. D. (1995). Photonic band gaps in optical lattices. *Physical Review A*, 52(2).

Di Domenico, G. and Weis, A. (2011). Vapor pressure and density of alkali metals. https://demonstrations.wolfram.com/VaporPressureAndDensityOfAlkaliMetals/. Wolfram Demonstrations Project, interactive computational model.

Dicke, R. H. (1954). Coherence in spontaneous radiation processes. *Physical Review*, 93(1):99–110.

Duan, L.-M., Lukin, M., Cirac, I., and Zoller, P. (2001). Long-distance quantum communication with atomic ensembles and linear optics. *Nature*, 414(6862):413–418. arXiv:quant-ph/0105105.

Erdogan, T. (1997). Fiber grating spectra. *Journal of Lightwave Technology*, 15(8):1277–1294.

Fang, Y., Qin, Z., Wang, H., Cao, L., Xin, J., Feng, J., Zhang, W., and Jing, J. (2015). Quantum optical devices based on four-wave mixing in hot rubidium vapor. *Science China Physics, Mechanics and Astronomy*, 58(6).

Farrera, P., Heinze, G., Albrecht, B., Ho, M., Chávez, M., Teo, C., Sangouard, N., and de Riedmatten, H. (2016). Generation of single photons with highly tunable wave shape from a cold atomic ensemble. *Nature Communications*, 7(1).

Foot, C. J. (2005). *Atomic Physics*. Oxford University Press.

Fox, M. (2006). *Quantum Optics: An Introduction*. OUP Oxford.

Glorieux, Q., Aladjidi, T., Lett, P. D., and Kaiser, R. (2023). Hot atomic vapors for nonlinear and quantum optics. *New Journal of Physics*, 25(5):051201.

Gorshkov, A. V., André, A., Fleischhauer, M., Sørensen, A. S., and Lukin, M. D. (2007). Universal approach to optimal photon storage in atomic media. *Physical Review Letters*, 98(12):123601.

Grynberg, G., Maître, A., and Petrossian, A. (1994). Flowerlike patterns generated by a laser beam transmitted through a rubidium cell with single feedback mirror. *Physical Review Letters*, 72(15).

Gyongyosi, L. and Imre, S. (2022). Advances in the quantum internet. *Commun. ACM*, 65(8):52–63.

Hadfield, R. H. (2009). Single-photon detectors for optical quantum information applications. *Nature Photonics*, 3(12):696–705.

Hammerer, K., Sorensen, A. S., and Polzik, E. S. (2010). Quantum interface between light and atomic ensembles. *Reviews of Modern Physics*, 82(2):1041–1093. arXiv:0807.3358 [quant-ph].

Hawthorn, C. J., Weber, K. P., and Scholten, R. E. (2001). Littrow configuration tunable external cavity diode laser with fixed direction output beam. *Review of Scientific Instruments*, 72(12):4477–4479.

He, F. and Zhu, K.-D. (2023). Single molecule photonic transistor and router through plasmonic nanocavity. *Applied Physics B*, 129(5).

Ho, M., Teo, C., Riedmatten, H. d., and Sangouard, N. (2018). Optimal photon generation from spontaneous raman processes in cold atoms. *New Journal of Physics*, 20(12):123018.

Häupl, D. R., Higgins, C. R., Pizzey, D., Briscoe, J. D., Wrathmall, S. A., Hughes, I. G., Löw, R., and Joly, N. Y. (2025). Modelling spectra of hot alkali vapour in the saturation regime. *New Journal of Physics*, 27(3):033003.

Hétet, G., Slodička, L., Hennrich, M., and Blatt, R. (2011a). Single atom as a mirror of an optical cavity. *Physical Review Letters*, 107(13):133002.

Hétet, G., Slodička, L., Hennrich, M., and Blatt, R. (2011b). Single atom as a mirror of an optical cavity. *Physical Review Letters*, 107(13).

Iturra, F. (2023). Crean en chile dispositivo capaz de generar números aleatorios y autocertificarse ante ciberataques. *Bio Bio Chile*. Available at: https://www.biobiochile.cl/noticias/ciencia-y-tecnologia/pc-e-internet/2023/12/11/crean-en-chile-dispositivo-capaz-de-generar-numeros-aleatorios-y-autocertificarse-ante-ciberataques.shtml (Accessed: September 26th, 2025).

Javanainen, J. and Rajapakse, R. (2019). Light propagation in systems involving two-dimensional atomic lattices. *Physical Review A*, 100(1).

Jaynes, E. and Cummings, F. (1963). Comparison of quantum and semiclassical radiation theories with application to the beam maser. *Proceedings of the IEEE*, 51(1):89–109.

Joshi, A. and Xiao, M. (2010). Atomic optical bistability in two- and three-level systems: perspectives and prospects. *Journal of Modern Optics*, 57(14-15).

Kenfack, A. and yczkowski, K. (2004). Negativity of the wigner function as an indicator of non-classicality. *Journal of Optics B: Quantum and Semiclassical Optics*, 6(10):396–404.

Kimble, H. J. (2008). The quantum internet. *Nature*, 453(7198):1023–1030.

Knight, P. L. (1986). Quantum fluctuations and squeezing in the interaction of an atom with a single field mode. *Physica Scripta*, 33(T12):51–55.

Laiho, K., Avenhaus, M., Cassemiro, K. N., and Silberhorn, C. (2009). Direct probing of the wigner function by time-multiplexed detection of photon statistics. *New Journal of Physics*, 11(4):043012.

Laurat, J., de Riedmatten, H., Felinto, D., Chou, C.-W., Schomburg, E. W., and Kimble, H. J. (2006). Efficient retrieval of a single excitation stored in an atomic ensemble. *Optics Express*, 14(15):6912.

Lee, C., Iwata, G. Z., Corsini, E., Higbie, J. M., Knappe, S., Ledbetter, M. P., and Budker, D. (2011). Small-sized dichroic atomic vapor laser lock. *Review of Scientific Instruments*, 82(4).

Leonhardt, U. (1997). *Measuring the Quantum State of Light*. Cambridge Studies in Modern Optics. Cambridge University Press.

Leonhardt, U. and Paul, H. (1995). Measuring the quantum state of light. *Progress in Quantum Electronics*, 19(2):89–130.

Liu, G., Zhou, W., Gromyko, D., Huang, D., Dong, Z., Liu, R., Zhu, J., Liu, J., Qiu, C.-W., and Wu, L. (2025). Single-photon generation and manipulation in quantum nanophotonics. *Applied Physics Reviews*, 12(1).

Lounis, B. and Orrit, M. (2005). Single-photon sources. *Reports on Progress in Physics*, 68(5):1129–1179.

Ludlow, A. D., Boyd, M. M., Ye, J., Peik, E., and Schmidt, P. O. (2015). Optical atomic clocks. *Reviews of Modern Physics*, 87(2):637–701.

Lutterbach, L. G. and Davidovich, L. (1997). Method for direct measurement of the wigner function in cavity qed and ion traps. *Physical Review Letters*, 78(13):2547–2550.

Lvovsky, A. I. and Raymer, M. G. (2009a). Continuous-variable optical quantum state tomography. *Reviews of Modern Physics*, 81(1):299–332. arXiv:quant-ph/0511044.

Lvovsky, A. I. and Raymer, M. G. (2009b). Continuous-variable optical quantum-state tomography. *Rev. Mod. Phys.*, 81:299–332.

Magro, V., Vaneecloo, J., Garcia, S., and Ourjoumtsev, A. (2023). Deterministic freely propagating photonic qubits with negative wigner functions. *Nature Photonics*, 17(8):688–693.

Makarov, D. (2022). Theory for the beam splitter in quantum optics: Quantum entanglement of photons and their statistics, hom effect. *Mathematics*, 10(24):4794.

Malomed, B. A., Mayteevarunyoo, T., Ostrovskaya, E. A., and Kivshar, Y. S. (2005). Coupled-mode theory for spatial gap solitons in optically induced lattices. *Physical Review E*, 71(5).

Marte, P., Zoller, P., and Hall, J. L. (1991). Coherent atomic mirrors and beam splitters by adiabatic passage in multilevel systems. *Physical Review A*, 44(7):R4118–R4121.

Mele, F. A., Lami, L., and Giovannetti, V. (2025). Maximum tolerable excess noise in continuous-variable quantum key distribution and improved lower bound on two-way capacities. *Nature Photonics*, 19(3):329–334.

Micheli, A., Daley, A. J., Jaksch, D., and Zoller, P. (2004). Single atom transistor in a 1d optical lattice. *Physical Review Letters*, 93(14).

Michelson, A. A. and Morley, E. W. (1887). Lviii. on the relative motion of the earth and the luminiferous aether. *The London, Edinburgh, and Dublin Philosophical Magazine and Journal of Science*, 24(151).

Miyake, H., Siviloglou, G. A., Puentes, G., Pritchard, D. E., Ketterle, W., and Weld, D. M. (2011). Bragg scattering as a probe of atomic wave functions and quantum phase transitions in optical lattices. *Physical Review Letters*, 107(17).

Moreno-Cardoner, M., Goncalves, D., and Chang, D. E. (2021). Quantum nonlinear optics based on two-dimensional rydberg atom arrays. *Physical Review Letters*, 127(26).

Moya-Cessa, H. and Knight, P. L. (1993). Series representation of quantum-field quasiprobabilities. *Physical Review A*, 48(3):2479–2481.

Mäusezahl, M., Munkes, F., and Löw, R. (2024). Tutorial on laser locking techniques and the manufacturing of vapor cells for spectroscopy. *New Journal of Physics*, 26(10):105002.

Nehra, R., Win, A., Eaton, M., Shahrokhshahi, R., Sridhar, N., Gerrits, T., Lita, A., Nam, S. W., and Pfister, O. (2019). State-independent quantum state tomography by photon-number-resolving measurements. *Optica*, 6(10):1356.

Nogues, G., Rauschenbeutel, A., Osnaghi, S., Bertet, P., Brune, M., Raimond, J. M., Haroche, S., Lutterbach, L. G., and Davidovich, L. (2000). Measurement of a negative value for the wigner function of radiation. *Physical Review A*, 62(5):054101.

Novikova, I., Zibrov, A. S., Phillips, D. F., Andre, A., and Walsworth, R. L. (2004). Dynamic optical bistability in resonantly enhanced raman generation. *Physical Review A*, 69(6):061802. arXiv:quant-ph/0404065.

Petrosyan, D., Otterbach, J., and Fleischhauer, M. (2011). Electromagnetically induced transparency with rydberg atoms. *Physical Review Letters*, 107(21).

Pezzagna, S., Rogalla, D., Wildanger, D., Meijer, J., and Zaitsev, A. (2011). Creation and nature of optical centres in diamond for single-photon emission—overview and critical remarks. *New Journal of Physics*, 13(3):035024.

Raja, S. V., Govindarajan, A., and Lakshmanan, M. (2024). Unique multistable states in periodic structures with saturable nonlinearity. *Optical Fiber Technology*, 87:103901. arXiv:2408.10249 [physics].

Rastogi, A. (2018). Light-matter interactions for quantum simulation and quantum memory experiments. M.sc. thesis, University of Alberta.

Rastogi, A. (2024). *Broadband, on-demand optical memories based on alkali-atom-ensemble for photonic quantum technologies*. Ph.d. thesis, University of Alberta.

Rastogi, A., Saglamyurek, E., Hrushevskyi, T., and LeBlanc, L. J. (2022). Superradiance-mediated photon storage for broadband quantum memory. *Physical Review Letters*, 129(12).

Robicheaux, F. (2025). Spatial averaging for light reflection and transmission through cold-atom arrays. *Physical Review A*, 111(1).

Rui, J., Wei, D., Rubio-Abadal, A., Hollerith, S., Zeiher, J., Stamper-Kurn, D. M., Gross, C., and Bloch, I. (2020). A subradiant optical mirror formed by a single structured atomic layer. *Nature*, 583(7816):369–374.

Ruostekoski, J. (2023). Cooperative quantum-optical planar arrays of atoms. *Physical Review A*, 108(3).

Saglamyurek, E., Hrushevskyi, T., Rastogi, A., Cooke, L. W., Smith, B. D., and LeBlanc, L. J. (2021). Storing short single-photon-level optical pulses in bose-einstein condensates for high-performance quantum memory. *New Journal of Physics*, 23(4):043028.

Saglamyurek, E., Hrushevskyi, T., Rastogi, A., Heshami, K., and LeBlanc, L. J. (2018). Coherent storage and manipulation of broadband photons via dynamically controlled autler-townes splitting. *Nature Photonics*, 12(12):774–782.

Sangouard, N., Simon, C., de Riedmatten, H., and Gisin, N. (2011). Quantum repeaters based on atomic ensembles and linear optics. *Reviews of Modern Physics*, 83(1):33–80.

Sangouard, N., Simon, C., Minář, J., Zbinden, H., de Riedmatten, H., and Gisin, N. (2007). Long-distance entanglement distribution with single-photon sources. *Physical Review A*, 76(5).

Shahmoon, E., Wild, D. S., Lukin, M. D., and Yelin, S. F. (2017). Cooperative

resonances in light scattering from two-dimensional atomic arrays. *Physical Review Letters*, 118(11).

Shinbrough, K. and Lorenz, V. O. (2023). Variance-based sensitivity analysis of lambda-type quantum memory. *Physical Review A*, 107(3):033703.

Shou, C. and Huang, G. (2021). Storage, splitting, and routing of optical peregrine solitons in a coherent atomic system. *Frontiers in Physics*, 9.

Sommerfeld, A. (1940). Zur feinstruktur der wasserstofflinien. geschichte und gegenwrtiger stand der theorie. *Die Naturwissenschaften*, 28(27).

Srakaew, K. (2024). *Rydberg interactions in subwavelength atomic arrays and Hubbard systems*. PhD thesis, Ludwig Maximilians Universität.

Srakaew, K., Weckesser, P., Hollerith, S., Wei, D., Adler, D., Bloch, I., and Zeiher, J. (2023). A subwavelength atomic array switched by a single rydberg atom. *Nature Physics*, 19(5):714–719.

Sridhar, N., Shahrokhshahi, R., Miller, A., Gerrits, T., Lita, A., Nam, S. W., and Pfister, O. (2015). Direct measurement of the wigner function by photon-number-resolving detection.

Steck, D. A. (2001). Rubidium 87 & 85 d line data. online at http://steck.us/alkalidata.

Stern, L., Zektzer, R., Mazurski, N., and Levy, U. (2016). Enhanced light-vapor interactions and all optical switching in a chip scale micro-ring resonator coupled with atomic vapor. *Laser Lamp; Photonics Reviews*, 10(6):1016–1022.

Strekalov, D. V., Matsko, A. B., and Yu, N. (2007). Electromagnetically induced transparency with a partially standing drive field. *Phys. Rev. A*, 76:053828.

Sudarshan, E. C. G. (1963). Equivalence of semiclassical and quantum mechanical descriptions of statistical light beams. *Physical Review Letters*, 10(7):277–279.

Suess, D., Rudnicki, L., maciel, T. O., and Gross, D. (2017). Error regions in quantum state tomography: computational complexity caused by geometry of quantum states. *New Journal of Physics*, 19(9):093013.

Thomas, J. M. (2012). The birth of x-ray crystallography. *Nature*, 491(7423):186–187.

Tretiakov, A. (2016). Versatile apparatus for ultracold atomic hybrid systems. M.sc. thesis, University of Alberta.

Uria, M., Hermann-Avigliano, C., Solano, P., and Delgado, A. (2026). Alice and bob through a quantum mirror.

Vivoli, V. C., Sangouard, N., Afzelius, M., and Gisin, N. (2013). High-bandwidth quantum memory protocol for storing single photons in rare-earth doped crystals. *New Journal of Physics*, 15(9):095012.

Wallentowitz, S. and Vogel, W. (1996). Unbalanced homodyning for quantum state measurements. *Physical Review A*, 53(6):4528–4533.

Wang, H., Yang, X., Zhang, L., Li, S., Zhang, C., Xie, C., and Peng, K. (2010). High-resolution resonance bragg-scattering spectroscopy of an atomic transition from a population difference grating in a vapour cell. *Journal of Physics B: Atomic, Molecular and Optical Physics*, 43(13):135403.

Weidemüller, M., Hemmerich, A., Görlitz, A., Esslinger, T., and Hänsch, T. W. (1995). Bragg diffraction in an atomic lattice bound by light. *Physical Review Letters*, 75:4583–4586.

Wieman, C. and Hänsch, T. W. (1976). Doppler-free laser polarization spectroscopy. *Physical Review Letters*, 36(20):1170–1173.

Wolff, C., Smith, M. J. A., Stiller, B., and Poulton, C. G. (2021). Brillouin scattering—theory and experiment: tutorial. *Journal of the Optical Society of America B*, 38(4):1243.

Yariv, A. and Yeh, P. (2002). *Optical Waves in Crystals: Propagation and Control of Laser Radiation*. Wiley-Interscience.

Yurke, B., McCall, S. L., and Klauder, J. R. (1986). Su(2) and su(1,1) interferometers. *Physical Review A*, 33(6):4033–4054.

Zhang, L., Stiesdal, N., Busche, H., Hansen, M. G., Pohl, T., and Hofferberth, S. (2024). Nonreciprocal recovery of electromagnetically induced transparency by wavenumber mismatch in hot atoms.

Zhang, Y. and Ding, E. a. (2025). Experimental single-photon quantum key distribution surpassing the fundamental weak coherent-state rate limit. *Physical Review Letters*, 134(21).

Zugenmaier, M. (2018). *Towards an on-demand single photon source based on room temperature vapour cells*. PhD thesis, Niels Bohr Institute.

Zuo, Y., Cao, C., Cao, N., Lai, X., Zeng, B., and Du, S. (2022). Optical neural network quantum state tomography. *Advanced Photonics*, 4(02).

A

Appendix

A.1 DLCZ vs Superradiance protocol additional results

This section shows the rest of the comparisons of the measurments described in Section 3.4.1 for both the DLCZ and SR protocols. The results shown here were obtained using a read power of 1.0 mW and 2.0 mW, with a varying write power. These measurements were completed by MSc. student Travis Hosack.

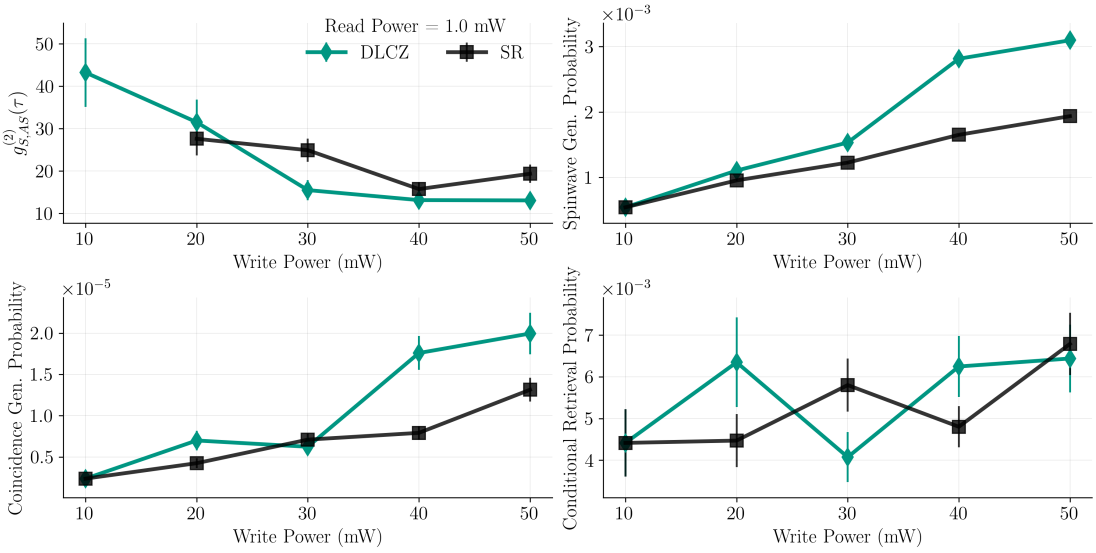

Figure A.1.1: DLCZ vs Superradiance protocol with a read power of 1.0 mW.

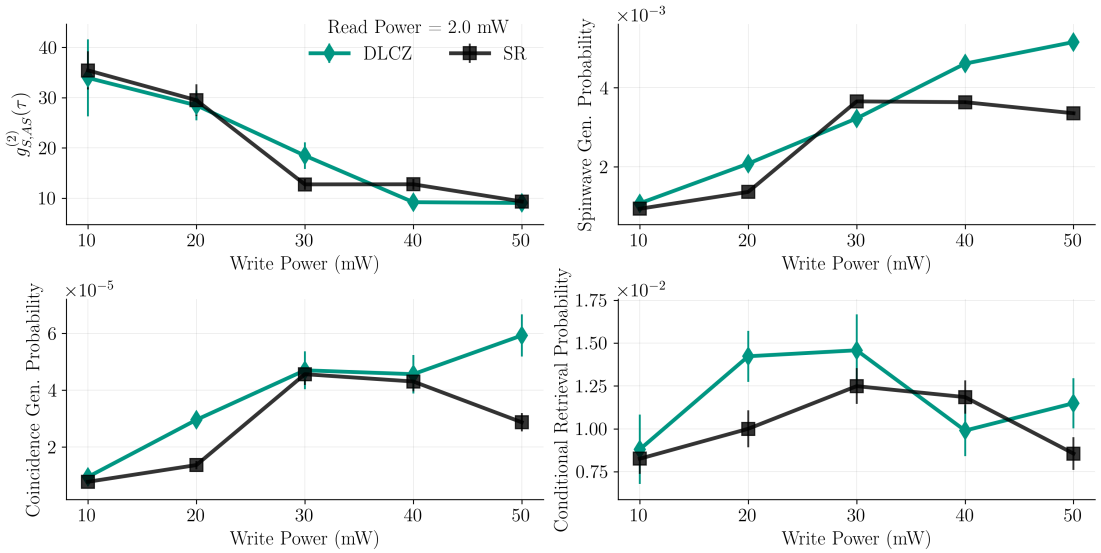

Figure A.1.2: DLCZ vs Superradiance protocol with a read power of 2.0 mW.

A.2 Quantum Mirror

A.2.1 Hamiltonian of The QM Operator

One can see this by expanding the exponential as a sum:

$$\hat{U}_{QM} = e^{i\theta\hat{\pi}_e \otimes \hat{L}_2} = \sum_n \frac{(i\theta)^n}{n!}(\hat{\pi}_e \otimes \hat{L}_2)^n. \tag{A.2.1}$$

We can use the exponent independently because of tensor properties,

$$\begin{aligned}
\hat{U}_{QM} = \sum_n \frac{(i\theta)^n}{n!}\hat{\pi}_e^n \otimes \hat{L}_2^n &= \frac{(i\theta)^0}{0!}\hat{\pi}_e^0 \otimes \hat{L}_2^0 + \sum_n \frac{(i\theta)^n}{n!}\hat{\pi}_e^n \otimes \hat{L}_2^n \\
&= \hat{1}_a \otimes \hat{1}_0 \otimes \hat{1}_1 + \sum_n \frac{(i\theta)^n}{n!}\hat{\pi}_e^n \otimes \hat{L}_2^n \\
&= (\hat{\pi}_g + \hat{\pi}_e) \otimes \hat{1}_0 \otimes \hat{1}_1 + \sum_{n=1} \frac{(i\theta)^n}{n!}\hat{\pi}_e^n \otimes \hat{L}_2^n \\
&= \hat{\pi}_g \otimes \hat{1}_0 \otimes \hat{1}_1 + \sum_{n=0} \frac{(i\theta)^n}{n!}\hat{\pi}_e^n \otimes \hat{L}_2^n,
\end{aligned}$$

one might easily confirm $\pi_e^n = \pi_e$.

$$\hat{U}_{QM} = \hat{\pi}_g \otimes \hat{1}_0 \otimes \hat{1}_1 + \sum_n \frac{(i\theta)^n}{n!} \hat{\pi}_e \otimes \hat{L}_2^n \tag{A.2.2}$$

$$= \hat{\pi}_g \otimes \hat{1}_0 \otimes \hat{1}_1 + \hat{\pi}_e \otimes \sum_n \frac{(i\theta)^n}{n!} \hat{L}_2^n \tag{A.2.3}$$

$$= \hat{\pi}_g \otimes \hat{1}_0 \otimes \hat{1}_1 + \hat{\pi}_e \otimes e^{i\theta \hat{L}_2}. \tag{A.2.4}$$

Which then confirms the original expression for the QM operator

$$\hat{U}_{QM} = \hat{\pi}_g \otimes \mathbf{1} \otimes \mathbf{1} + \hat{\pi}_e \otimes \hat{U}_{BS}. \tag{A.2.5}$$

For a time independent Hamiltonian

$$U(t, t_0) = e^{-\frac{i}{\hbar} H(t - t_0)}, \tag{A.2.6}$$

equivalent to the following expression

$$U(\theta, \theta_0) = e^{-\frac{i}{\hbar} H(\theta - \theta_0)} \tag{A.2.7}$$

only if the parameter θ is rescaled in units of time $\theta = g(t - t_0)$, associated to an interaction time between the modes and the QM. Now we can take $\theta_0 = 0$ and write

$$U(\theta) = e^{-\frac{i}{\hbar} H(\theta)} = e^{i\theta \hat{\pi}_e \otimes \hat{L}_2} \rightarrow \hat{H} = \hbar \hat{\pi}_e \otimes \hat{L}_2 \tag{A.2.8}$$

A.2.2 Controlled Phase Interaction

To work on this expression, we must consider the basis on which we are tracing, in this case $\mathrm{Tr}\{\rho_{total} |\xi_\pm\rangle \langle\xi_\pm|\}$ is equivalent to expanding the terms as

$$|\xi_\pm\rangle \langle\xi_\pm| = \pi_{gg} \pm e^{-i\delta} \pi_{ge} \pm e^{i\delta} \pi_{eg} + \pi_{ee}. \tag{A.2.9}$$

This sum will multiply over each of the terms in expression 4.6.2, which we can immediately evaluate (first) on the atomic subspace trace as:

$$\begin{aligned}
\mathrm{Tr}_{atom}\left[\pi_{gg}\left|\xi_{\pm}\right\rangle\left\langle\xi_{\pm}\right|\right] &= 1 \otimes (\text{mode } 0 \otimes \text{mode } 1) \\
\mathrm{Tr}_{atom}\left[\pi_{ge}\left|\xi_{\pm}\right\rangle\left\langle\xi_{\pm}\right|\right] &= \pm e^{i\delta} \otimes (\text{mode } 0 \otimes \text{mode } 1) \\
\mathrm{Tr}_{atom}\left[\pi_{eg}\left|\xi_{\pm}\right\rangle\left\langle\xi_{\pm}\right|\right] &= \pm e^{-i\delta} \otimes (\text{mode } 0 \otimes \text{mode } 1) \\
\mathrm{Tr}_{atom}\left[\pi_{ee}\left|\xi_{\pm}\right\rangle\left\langle\xi_{\pm}\right|\right] &= 1 \otimes (\text{mode } 0 \otimes \text{mode } 1)
\end{aligned}$$

For the trace over the modes, we have to consider the fact that the off-diagonal terms do not possess a straightforwardly unitary operation, so we will write in general the trace operation, that will take the number operator out of all phase operators $\hat{U}$.

$$\mathrm{Tr}\{U_v\left|a\right\rangle\left\langle b\right|U_u\} = \sum_n \left\langle n\right|U_v\left|a\right\rangle\left\langle b\right|U_u\left|n\right\rangle = \sum_n \left\langle b\right|U_u\left|n\right\rangle\left\langle n\right|U_v\left|a\right\rangle$$

for example:

$$\begin{aligned}
&\mathrm{Tr}_0\left[\sum_i p_i' U_{\pi+\varphi_1-\varphi_2-\phi}\left|\varphi\right\rangle\left\langle\psi_i'\right|U^{\dagger}_{\varphi_0-\varphi_2}\right] \\
&= \sum_i p_i' \sum_n \left\langle\psi_i'\right|U^{\dagger}_{\varphi_0-\varphi_2}\left|n\right\rangle\left\langle n\right|U_{\pi+\varphi_1-\varphi_2-\phi}\left|\varphi\right\rangle \\
&= \sum_i p_i' \left\langle\psi_i'\right| e^{-i(\varphi_0-\varphi_2)n} e^{i(\pi+\varphi_1-\varphi_2-\phi)n}\left|\varphi\right\rangle \\
&= \sum_i p_i' \left\langle\psi_i'\right| e^{-i(\varphi_0-\varphi_1+\phi)n}\hat{P}\left|\varphi\right\rangle
\end{aligned}$$

Then, the results of tracing over mode 0 leave us with the following

$$\begin{aligned}
&\mathrm{Tr}_0\left[U_{\varphi_0-\varphi_2}\hat{\rho}' U^{\dagger}_{\varphi_0-\varphi_2}\right] = 1 \otimes (\text{mode } 1) \\
&\mathrm{Tr}_0\left[U_{\varphi_0-\varphi_2}\sum_i p_i'\left|\psi_i'\right\rangle\left\langle\varphi\right|U^{\dagger}_{\pi+\varphi_1-\varphi_2-\phi}\right] = \sum_i p_i'\left\langle\varphi\right|\hat{P}^{\dagger}e^{i(\varphi_0-\varphi_1+\phi)n}\left|\psi_i'\right\rangle \otimes (\text{mode } 1) \\
&\mathrm{Tr}_0\left[\sum_i p_i' U_{\pi+\varphi_1-\varphi_2-\phi}\left|\varphi\right\rangle\left\langle\psi_i'\right|U^{\dagger}_{\varphi_0-\varphi_2}\right] = \sum_i p_i'\left\langle\psi_i'\right| e^{-i(\varphi_0-\varphi_1+\phi)n}\hat{P}\left|\varphi\right\rangle \otimes (\text{mode } 1) \\
&\mathrm{Tr}_0\left[U_{\pi+\varphi_1-\varphi_2-\phi}\left|\varphi\right\rangle\left\langle\varphi\right|U^{\dagger}_{\pi+\varphi_1-\varphi_2-\phi}\right] = 1 \otimes (\text{mode } 1)
\end{aligned}$$

then,

$$\begin{aligned}
&\mathrm{Tr}_1\left[U_{\varphi_1-\varphi_3}\left|\varphi\right\rangle\left\langle\varphi\right|U^{\dagger}_{\varphi_1-\varphi_3}\right] = 1\\
&\mathrm{Tr}_1\left[U_{\varphi_1-\varphi_3}\left|\varphi\right\rangle\left\langle\psi_i'\right|U^{\dagger}_{\pi+\varphi_0-\varphi_3-\phi}\right] = \left\langle\psi_i'\right|\hat{P}^{\dagger}e^{-i(\varphi_0-\varphi_1-\phi)n}\left|\varphi\right\rangle\\
&\mathrm{Tr}_1\left[U_{\pi+\varphi_0-\varphi_3-\phi}\left|\psi_i'\right\rangle\left\langle\varphi\right|U^{\dagger}_{\varphi_1-\varphi_3}\right] = \left\langle\varphi\right|e^{i(\varphi_0-\varphi_1-\phi)n}\hat{P}\left|\psi_i'\right\rangle\\
&\mathrm{Tr}_1\left[U_{\pi+\varphi_0-\varphi_3-\phi}\hat{\rho}'U^{\dagger}_{\pi+\varphi_0-\varphi_3-\phi}\right] = 1
\end{aligned}$$

Which will then allow us to write the full expression for the trace

$$\begin{aligned}
p_{\pm}(\delta) = \frac{1}{4} + \frac{1}{4} \pm \frac{e^{i\delta}}{4}&\left(\sum_i p_i'\left\langle\varphi\right|\hat{P}^{\dagger}e^{i(\varphi_0-\varphi_1+\phi)n}\left|\psi_i'\right\rangle\left\langle\psi_i'\right|\hat{P}^{\dagger}e^{-i(\varphi_0-\varphi_1-\phi)n}\left|\varphi\right\rangle\right)\\
\pm\frac{e^{-i\delta}}{4}&\left(\sum_i p_i'\left\langle\psi_i'\right|e^{-i(\varphi_0-\varphi_1+\phi)n}\hat{P}\left|\varphi\right\rangle\left\langle\varphi\right|e^{i(\varphi_0-\varphi_1-\phi)n}\hat{P}\left|\psi_i'\right\rangle\right)
\end{aligned}$$

rewriting

$$p_{\pm}(\delta) = \frac{1}{4}\left(2 \pm e^{i\delta}\sum_i p_i'\left\langle\varphi\right|e^{-i(\pi-\phi-\Delta)n}\left|\psi_i'\right\rangle\left\langle\psi_i'\right|e^{-i(\pi-\phi+\Delta)n}\left|\varphi\right\rangle \pm c.c\right) \tag{A.2.10}$$